

NASA Contractor Report 3473

NASA
CR
3473
c.-

0062900

Improved Simulation of Aerosol, Cloud, and Density Measurements by Shuttle Lidar

Philip B. Russell, Bruce M. Morley,
John M. Livingston, Gerald W. Grams,
and Edward M. Patterson

NON-COPY: RETURN TO
AFWL TECHNICAL LIBRARY
KIRTLAND AFB, N.M.

CONTRACT NAS1-16052
NOVEMBER 1981

NASA



NASA Contractor Report 3473

Improved Simulation of Aerosol, Cloud, and Density Measurements by Shuttle Lidar

Philip B. Russell, Bruce M. Morley,
and John M. Livingston
SRI International
Menlo Park, California

Gerald W. Grams and Edward M. Patterson
Georgia Institute of Technology
Atlanta, Georgia

Prepared for
Langley Research Center
under Contract NAS1-16052



National Aeronautics
and Space Administration

**Scientific and Technical
Information Branch**

1981

CONTENTS

LIST OF ILLUSTRATIONS.....	vi
LIST OF TABLES.....	vii

Part 1: EXECUTIVE SUMMARY

I INTRODUCTION.....	3
II RESULTS.....	7
A. Atmospheric Models.....	7
B. Lidar Parameters.....	7
C. Other Inputs.....	8
D. Aerosol and Cloud Measurements at 0.53 and 1.06 μm	9
E. Density, Temperature, Aerosol, and Cloud Measurements at 0.355, 0.532, and 1.064 μm	11
III RECOMMENDATIONS.....	15
A. Hardware Development.....	15
B. Further Studies.....	16
C. Correlative Sensors.....	17
REFERENCES.....	19

Part 2: ORBITING LIDAR SIMULATIONS: AEROSOL AND CLOUD MEASUREMENTS BY AN INDEPENDENT-WAVELENGTH TECHNIQUE

I INTRODUCTION.....	23
II SUMMARY OF INDEPENDENT-WAVELENGTH AEROSOL LIDAR ERROR ANALYSIS METHOD.....	25
III SIMULATION PROCEDURE.....	31

IV	SIMULATION INPUTS.....	33
A.	Atmospheric Models.....	33
B.	Lidar Parameters.....	34
C.	Background Lighting.....	39
D.	Error Sources.....	40
	1. Signal.....	40
	2. Molecular Density.....	43
	3. Transmission.....	44
	4. R_{\min}	46
V	SIMULATION RESULTS.....	49
A.	Signal and Background Profiles.....	49
B.	Retrievals.....	50
	1. Tropical, Nonvolcanic, Cloud-Free, Saharan.....	50
	a. Nighttime (Zenith Moonlit Cloud).....	50
	b. Daytime (Zenith Sunlit Ocean).....	53
	2. Midlatitude, Volcanic, Cirrus, Marine.....	56
	a. Nighttime (Zenith Moonlit Cloud).....	56
	b. Daytime (Zenith Sunlit Cloud).....	58
	3. High-Latitude, Nonvolcanic, Noctilucent Cloud, Marine.....	60
	a. Nighttime (Moonlit Cloud, $\cos \theta_0 = 0.5$).....	60
	b. Daytime (Sunlit Cloud or Ice, $\cos \theta_0 = 0.5$).....	62
VI	SUMMARY AND CONCLUSIONS.....	65
APPENDICES		
A	ATMOSPHERIC MODELS.....	69
B	BACKSCATTER-TO-EXTINCTION RATIOS.....	99
	REFERENCES.....	105

Part 3: ORBITING LIDAR SIMULATIONS:
DENSITY, TEMPERATURE, AEROSOL AND CLOUD MEASUREMENTS
BY A WAVELENGTH-COMBINING TECHNIQUE

I	INTRODUCTION.....	117
II	SOLUTION TECHNIQUE.....	121
A.	Gas Density and Particle Backscatter Profiles.....	121
B.	Pressure and Temperature Profiles.....	125

III	ERROR ANALYSIS.....	129
	A. Gas Density and Particle Backscatter Profiles.....	129
	B. Temperature Profiles.....	130
IV	SIMULATION PROCEDURE.....	133
V	SIMULATION INPUTS.....	135
VI	SIMULATED PERFORMANCE.....	137
	A. Tropical, Nonvolcanic, Cloud-Free, Saharan; Nighttime.....	137
	B. Midlatitude, Volcanic, Cloudy, Marine; Nighttime.....	142
	C. High-Latitude, Nonvolcanic, Cloud-Free, Marine, Nighttime.....	144
VII	SUMMARY AND CONCLUSIONS.....	149
	REFERENCES.....	157

ILLUSTRATIONS

Part 2

1	Simulation Procedure for Evaluating Lidar Measurement and Retrieval Errors.....	32
2	Model Backscatter Mixing Ratio Profiles, Single-Shot Signal and Background Profiles for Low Latitude.....	35
3	Model Backscatter Mixing Ratio Profiles, Single-Shot Signal and Background Profiles for Middle Latitude.....	36
4	Model Backscatter Mixing Ratio Profiles, Single-Shot Signal and Background Profiles for High Latitude.....	37
5	Low-Latitude Nighttime Simulation Results, 1.064 and 0.532 μm , Using Conventional Density Data.....	51
6	Low-Latitude Daytime Simulation Results, 1.064 and 0.532 μm , Using Conventional Density Data.....	54
7	Midlatitude Nighttime Simulation Results, 1.064 and 0.532 μm , Using Conventional Density Data.....	57
8	Midlatitude Daytime Simulation Results, 1.064 and 0.532 μm , Using Conventional Density Data.....	59
9	High-Latitude Nighttime Simulation Results, 1.064 and 0.532 μm , Using Conventional Density Data.....	61
10	High-Latitude Daytime Simulation Results, 1.064 and 0.532 μm , Using Conventional Density Data.....	63

Part 3

1	Multiwavelength Analysis Procedure to Retrieve Profiles of Scattering Ratio and Molecular Density.....	122
2	Low-Latitude Nighttime Simulation Results, 0.355 μm	138
3	Low-Latitude Nighttime Simulation Results, 1.064 and 0.532 μm , Using Lidar Density Data Above 7 km, Conventional Density Below.....	141
4	Midlatitude Nighttime Simulation Results, 0.355 μm	143

5	High-Latitude Nighttime Simulation Results, 0.355 μm	145
6	High-Latitude Nighttime Simulation Results, 1.064 and 0.532 μm , Using Lidar Density Data Above 5 km, Conventional Density Below.....	147

TABLES

Part 2

1	Assumed Lidar Parameters.....	38
2	Background Lighting (Zenith Upward Spectral Radiance) for a Downward-Viewing Lidar and Several Scenarios.....	40
3	Representative 1σ Uncertainties in Density Profiles Derived from Conventional Sources.....	44

Part 1
EXECUTIVE SUMMARY

I INTRODUCTION

A 1979 report¹ by the National Aeronautics and Space Administration's Atmospheric Lidar Working Group defined seven scientific objectives that could be usefully addressed by an orbiting lidar. The objectives are:

- (1) Defining the global flow of water vapor and pollutants.
- (2) Improving stratospheric and mesospheric chemistry and transport models.
- (3) Improving atmospheric radiation-balance models.
- (4) Augmenting the meteorological data base.
- (5) Understanding upper atmospheric waves.
- (6) Investigating thermospheric atomic species.
- (7) Investigating magnetospheric aspects of sun/weather relationships.

Aerosol and cloud measurements play vital roles in Objectives (1)-(3) and (5), and an important, though secondary, role in Objective (4). In addition, stratospheric/tropospheric temperature profile measurements are important to each of Objectives (1)-(5).

The Working Group report¹ defines the accuracy and resolution that measurements must have for each objective. In addition, the report briefly indicates the accuracy and resolution thought to be achievable in various orbiting lidar experiments. However, the Working Group's activities did not include detailed and complete calculations of aerosol and cloud retrievals for the wide variety of atmospheric and measurement conditions that are likely to be encountered in practice. Thus, the question was not fully explored as to how well shuttle lidar aerosol and cloud measurements could contribute to each objective. Also not explored was the possible use of lidar backscatter profiles at the tripled Nd:YAG laser wavelength (0.355 μm) to aid aerosol measurements and possibly to provide temperature profile measurements.

During the Working Group meetings, General Electric Space Division, under contract to NASA, began a facility definition study² to better define the lidar system hardware that would be compatible with both the space shuttle accommodations and the Working Group's scientific objectives. That study established hardware parameters that could be used in scientific simulation studies with the confidence that they could actually be implemented in a future shuttle-borne system.

The Atmospheric Lidar Working Group report and G.E. Facility Definition report thus laid the groundwork for the present study. The objective of this study is to assess quantitatively, for a variety of realistic scenarios, the accuracy and resolution with which aerosol, cloud, density, and temperature profiles could be retrieved from measurements made by an orbiting Nd:YAG lidar having parameters consistent with the G.E. study. This process indirectly identifies the lidar parameters required to obtain scientifically useful data. The aerosol and cloud assessments were to be made using an error-analysis-and-simulation code available at SRI; the code was to be improved as part of the study. The density and temperature assessments were to be made using a new analysis technique based on elastic backscatter at wavelength $0.355\text{ }\mu\text{m}$ (with aerosol and cloud corrections from longer wavelengths). This technique yields density profiles that are then integrated vertically to yield pressure and temperature profiles. Subsidiary goals were to:

- Define a realistic set of aerosol, cloud, density, and ozone models for input to the assessment.
- Define the correlative sensors that could best aid the lidar in achieving the objectives of the Working Group report.
- Point out specific hardware implications of the necessary lidar parameters.
- Expose the study methods and results to the scrutiny of the scientific community, for example by publishing them in a refereed journal.

A specific question addressed by the study was whether the scientific benefit expected from the measurements at $0.355\text{ }\mu\text{m}$ would warrant the additional complexity of transmitting, detecting, and processing signals at that wavelength.

Part 2 of this report gives detailed results of the aerosol and cloud analyses, while Part 3 gives the results of the density and temperature (plus improved aerosol and cloud) analyses. Those parts are formatted for rapid conversion to journal manuscripts, in support of the last objective mentioned above. The remainder of Part 1 summarizes the results and makes the recommendations mentioned above.

This report has benefitted considerably from discussions with E.V. Browell and S.T. Shipley, who also performed a critical review of a previous draft version.

II RESULTS

A. Atmospheric Models

Atmospheric models were developed for low, middle, and high latitude bands. The models include profiles of total gas density, ozone, cirrus and noctilucent clouds, as well as mesospheric, stratospheric, and tropospheric (Saharan and marine) aerosols. Profiles of back-scattering and extinction coefficient at wavelengths 0.266, 0.355, 0.532, 0.694, and 1.064 μm were computed for each model. The models are based on previous optical and physical measurements, and have been compared to previous ruby lidar measurements, so as realistically to represent the conditions encountered in practice. The models and their derivation are described in Appendix A of Part 2.

B. Lidar Parameters

A set of lidar parameters was developed after careful review of the G.E. Facility Definition report,² the scientific measurement goals, and our own review of hardware capabilities. The detailed parameters are listed in Table 1 of Part 2. Important points to note here are the following:

- Three wavelengths (1.064, 0.532, and 0.355 μm) are transmitted simultaneously, but they are obtained from a single Nd:YAG laser by harmonic generation, with no special line-narrowing, tuning, or wavelength-stability requirements.
- Three detectors and two dichroic beamsplitters are used to measure all three wavelengths simultaneously, but detector linewidth and stability can be provided by interference filters, with no need for interferometers or other more sophisticated spectral discriminators.

- Transmitted energies and beam divergences satisfy the preliminary eye safety guidelines* developed by G.E.²
- The weight, power, space, and other requirements implied by the lidar parameters are consistent with the limits for shuttle science payloads.

In sum, the lidar system assumed here may be considered as a baseline system, suitable for an early shuttle mission. The transmitter is less sophisticated than the Nd:YAG-pumped dye laser system considered in the Working Group and Facility Definition reports^{1,2} as the first module in an evolutionary system. Nevertheless, the engineering aspects of transmitting the fundamental, doubled, and tripled wavelengths simultaneously from shuttle have not been worked out.² Also, the three-wavelength detection system is more complex than the two-wavelength systems emphasized by the Facility Definition report.² Finally, we have followed the Facility Definition report in assuming different receiver fields of view and filter bandwidths for viewing daylite and dark portions of the earth. (See Table 1, Section IV-B of Part 2). This procedure is necessary to maximize scientific gain consistent with eye safety;² however, it implies the use of a system that automatically changes telescope beam stops and interference filters upon crossing from dark to daylite areas.

C. Other Inputs

Background radiances at the three lidar wavelengths were developed to represent sunlit clouds, sunlit ocean, and moonlit clouds, each as a function of source (sun or moon) zenith angle. (See Table 2, Section IV-C of Part 2.) Probable errors in atmospheric transmission and in calibrating the received lidar signal in terms of atmospheric backscatter were adapted from a previous study,³ taking into account the larger range of heights and aerosol and cloud types considered in the current study. In particular, we adopted a 1 σ uncertainty for one-way transmission in an aerosol or cloud layer of one-half the particulate

*See also Section IV-B of Part 2.

optical thickness τ_p , because effective backscatter-to-extinction ratios in most appreciably turbid media (i.e., those with $\tau_p \geq 0.3$) cannot be estimated to an accuracy of better than ± 50 percent, even with the aid of multiwavelength lidar measurements. (See Appendix B of Part 2.) We also assumed that the root-mean-square (rms) errors in conventional molecular density profiles (used to analyze the lidar data) were appropriate to data-sparse regions of the globe where most shuttle lidar data will be acquired and where shuttle lidar is most likely to fill data gaps. Specifically, we assumed conventional density rms errors ranging from 2 to 3 percent below 30 km and 5 to 10 percent above 40 km.

D. Aerosol and Cloud Measurements at 0.53 and 1.06 μm

We first considered a lidar with only the fundamental and doubled wavelengths (1.06 and 0.53 μm) available, each being analyzed independently, using conventional density data, to retrieve aerosol and cloud backscatter profiles. Simulations were conducted for low, middle, and high latitude model atmospheres, assuming a variety of daytime and nighttime backgrounds. For each scenario, expected errors in retrieved particle backscatter were calculated from algebraic expressions and also checked by numerical simulations using random number generators. Both the algebraic expressions and the simulations include the four sources of error that we have encountered in actual lidar measurements and analyses--namely, errors in (1) measuring the backscattered signal, (2) accounting for transmission losses, (3) determining the total gas density profile at the lidar location, and (4) calibrating signals in terms of atmospheric backscatter by using an atmospheric layer where gas backscatter dominates particle backscatter.

The results show that useful retrievals can be made for the following constituents and conditions:

- By day: Vertical structure of tenuous clouds (subvisible and visible), Saharan aerosols, and boundary-layer aerosols (at both 0.53 and 1.06 μm wavelengths), and strong volcanic stratospheric aerosols (at 0.53 μm). Quantitative backscatter can be

determined for all of the preceding, provided particulate optical depth does not exceed ~ 0.3 .

- By night: Vertical structure and quantitative backscatter for all of the above, plus upper tropospheric and stratospheric aerosols (at $1.06 \mu\text{m}$) and mesospheric aerosols (at $0.53 \mu\text{m}$) and noctilucent clouds (at 0.53 and $1.06 \mu\text{m}$). (Again, quantitative backscatter retrievals suffer when particulate optical depth exceeds ~ 0.3).

These results were obtained with vertical resolutions of 0.1 to 0.5 km in the troposphere and 0.5 to 2.0 km in the stratosphere and above, except within the mesospheric aerosol and noctilucent cloud layers, where resolutions of 1.0 and 0.25 km , respectively, were used. Horizontal resolution was 100 km in the troposphere, 200 km in the stratosphere and lower mesosphere (below $\sim 60 \text{ km}$), and 2000 km in the upper mesosphere (to $\sim 85 \text{ km}$). Vertical structure of the stronger layers (noctilucent and cirrus clouds, lower tropospheric aerosols) could be observed on much finer horizontal scales (sometimes on single shots--about 700 m apart); moreover, these fine-scale results could be converted to quantitative backscatter if a transmit energy monitor or stable transmit energy were provided.

In general, the principal virtue of the $1.06\text{-}\mu\text{m}$ wavelength is its reduced sensitivity to gas density errors, which are the dominant error source for upper tropospheric and nonvolcanic stratospheric aerosol retrievals. Also, $1.06\text{-}\mu\text{m}$ retrievals are somewhat less susceptible to transmission errors in the stronger layers. The principal virtue of the $0.53\text{-}\mu\text{m}$ wavelength is the stronger signals available (because of atmospheric backscatter and quantum efficiency). These stronger signals are essential for observing the mesospheric aerosol layers at useful horizontal and vertical resolutions.

At 0.53 and $1.06 \mu\text{m}$, errors in the gas density profile are the dominant source of uncertainty in measuring nonvolcanic stratospheric and upper tropospheric aerosols. Although useful retrievals of these aerosols can be made at $1.06 \mu\text{m}$ using conventional density information, retrievals at both wavelengths would be improved by better density information.

E. Density, Temperature, Aerosol, and Cloud Measurements
at 0.355, 0.532, and 1.064 μm

We next considered a lidar having three wavelengths--0.355, 0.53, and 1.06 μm . An analysis technique (Figure 1 of Part 3) was developed that combines information from 0.355 and 1.06 μm to yield a relative density profile and an uncertainty profile that takes into account aerosol and cloud contamination. The relative density profile is converted to an absolute density profile by normalization at an assumed isopycnic level or a level where conventional density data are available to good accuracy. The lidar-derived density profile is used to improve aerosol and cloud retrievals at 0.53 and 1.06 μm , and is also integrated vertically (from a reference height where temperature or pressure are guessed) to yield pressure and temperature profiles. The two keys to the success of this analysis procedure are:

- Returns at 0.355 μm are much more sensitive to gas backscattering than are those at 1.06 μm . (Hence, on a relative basis, 0.355 μm returns are much less sensitive to aerosol contamination, whereas 1.06 μm returns readily indicate regions where particulate contamination might be significant.)
- Aerosol retrievals and the lidar-inferred temperature profiles are relatively insensitive to bias errors in the density profile, so that errors in absolute density normalization have very little effect on these data products. Also, this reduces the effect of some transmission errors.

Error analysis equations were developed to quantify the above arguments and to provide error bars on all retrieved quantities. Also, to check the algebraic error expressions, the numerical simulation code was extended to inject appropriate errors into the multiwavelength retrieval procedure. In addition to the four error sources listed in Section II-B (signal, transmission, conventional density, and calibration), we also included errors in absolute density normalization, in the reference temperature or pressure, and in estimating short-wavelength particle backscatter from a long-wavelength measurement (with errors).

Simulations were run for the low, middle, and high-latitude model atmospheres. In general, cirrus clouds (subvisible as well as visible)

and lower tropospheric aerosols introduced density and temperature errors that were larger than those in conventional data; daytime signal measurement errors were similarly large in the stratosphere and above. Hence, useful lidar density and temperature measurements were restricted to nighttime conditions in the stratosphere and (cloud-free) upper troposphere. (Signal errors also prevented useful measurements in the mesosphere if horizontal resolution was 2000 km or less.)

Simulations were run with vertical resolutions of 0.5 to 1.0 km in the upper troposphere and lower stratosphere, and 2.0 km in the upper stratosphere. A horizontal resolution of 200 km provided useful signal accuracies (0.5 to 2.0 percent) below 40 km; however, this was increased to 2000 km to extend useful signals to 55 km. Retrieved relative density profiles had rms errors of 0.5 to 2 percent in the upper troposphere and stratosphere. The limiting error at most heights was signal measurement error. However, nonvolcanic stratospheric aerosols introduced errors of 1 to 2 percent at the mixing ratio peak (typically ~27 km at low latitudes to ~16 km at high latitudes). For a given amount of particle backscatter, the density error tends to be larger at low latitudes, because the low-latitude peak occurs at greater heights, where the smaller absolute density yields larger relative errors. A midlatitude moderate volcanic stratospheric aerosol model introduced relative density errors of about 3 percent at the peak (~18 km).

Use of the lidar-derived relative density profiles in place of conventional profiles significantly improved the accuracy of aerosol retrievals in the nonvolcanic stratosphere and upper troposphere. This was especially so at 0.53 μm , where conventional density errors had led to very poor retrievals at these heights. The impact of lidar-derived density errors on volcanic stratospheric aerosol retrievals was minimal, both because of the insensitivity of such retrievals to density errors and because of the poorer accuracy of the volcanic lidar density profile.

For cloud-free, nonvolcanic conditions, lidar-derived temperature profiles had rms errors of 1.2 to 2.5 K in a layer bounded on the bottom by strongly scattering tropospheric aerosol layers and on the top by a height ~ 8 km below the reference height where temperature or pressure was guessed. For the model atmospheres used here, this lower bound was ~ 5 km; the upper bound was ~ 32 km for a horizontal resolution of 200 km and ~ 47 km for a horizontal resolution of 2000 km (i.e., the reference heights were at ~ 40 and ~ 55 km, respectively). The midlatitude moderate volcanic stratospheric aerosol introduced temperature errors of ~ 3 K between 17 and 20 km. These simulations assumed an 8 K rms error in the temperature guessed at the reference height (40 to 55 km).

The major advantage of these lidar-derived temperature profiles over those obtained by passive nadir-viewing spaceborne sensors is their fine vertical resolution (~ 0.5 km in the upper troposphere and tropopause region, increasing to ~ 2 km in the upper stratosphere). This resolution would permit defining the tropopause and temperature-wave structures to a degree of detail never before possible.

In general, the simulations validated the algebraic expressions used to put error bars on lidar-derived density and temperature profiles. This is important, because the errors reported above apply to specific atmospheric situations and will, for example, increase considerably whenever strong particulate (cloud or aerosol) layers are encountered. In this respect the outstanding feature of the multiwavelength analysis technique is that it simultaneously retrieves density and particle profiles, and includes particle contamination effects in the density and temperature error bars. Thus, the user is immediately aware of significant cloud or aerosol contamination.

III RECOMMENDATIONS

A. Hardware Development

A major conclusion of this study is that considerable scientific benefits can be obtained by adding measurements at $0.355\ \mu\text{m}$. Therefore, we recommend that:

- A ground-based or airborne three-wavelength Nd:YAG lidar system be built to make aerosol, cloud, density, and temperature measurements, both to test the conclusions reached in this study and to aid in refining the analysis techniques by using actual data.
- The three-wavelength Nd:YAG transmitter/detector configuration be included in any future engineering studies of the shuttle lidar facility.

This study has also shown that, in the lowest few kilometers of the atmosphere, aerosol structure can be usefully retrieved with a vertical resolution of 0.1 km or less, sometimes from single-shot returns. Elsewhere in the troposphere, even subvisible cloud heights can be retrieved to 0.25 km or less. Vertical resolution of 0.5 to 1 km is useful in the lower stratosphere, and 2 km above, with 1 and 0.25 km vertical resolution in the mesospheric aerosol and noctilucent cloud layers, respectively. This implies that:

- The shuttle lidar data recording and/or telemetry system be designed to preserve three simultaneous profiles for each shot, with vertical resolution similar to the following:

Altitude (km)	Vertical Resolution (km)
0-5	0.1
5-18	0.25
18-30	1
30-40	2
40-75	1
75-85	0.25
85-90	2

Most signal profiles will be partly in the pulse-counting regime, partly in the current regime, and partly in the intermediate regime (~ 1 to $100 \text{ pulses } \mu\text{s}^{-1}$) where both of these conventional recording techniques encounter practical difficulties (e.g., pulse overlap and nonuniform charge per pulse). The data analysis techniques require that each part of any profile be relatable to other parts with an accuracy of $\sim 0.5\%$ or better. Therefore we recommend that:

- A reliable, repeatable, and precise method⁴ of logging and splicing together all parts of the signal profile from 0 to 90 km be developed and tested. The method should permit determination of the ratio of signal return from any height to that from any other height to an accuracy of 0.5% or better, as well as accurate logging of the strong surface return. (The above accuracy excludes the \sqrt{N} statistical error inherently determined by the pulse-generation rate in the pulse-counting mode; this error can be reduced by summing many shots or expanding the size of pulse-counting range bins.)

B. Further Studies

This study has raised several important questions that could be answered by further study. Therefore we recommend that:

- The simulation program be used to evaluate the expected performance of:
 - A ground-based or airborne three-wavelength lidar design, as recommended in Section A.
 - A two-wavelength lidar based on the alexandrite solid-state laser ($\lambda = 0.7$ to $0.8 \mu\text{m}$) and second harmonic generation. Such a system would benefit from increased quantum efficiency and atmospheric backscatter at $\sim 0.75 \mu\text{m}$ as compared to $1.06 \mu\text{m}$, while retaining many of the benefits of the more complex three-wavelength system simulated in this study. The tunability of the alexandrite laser also favors other measurements, such as water vapor by differential absorption.
 - A three-wavelength spaceborne lidar with increased output at the (relatively eye-safe) $0.355 \mu\text{m}$ wavelength, to extend the upper height limit and improve the horizontal resolution of density and temperature measurements.
- A statistical study of existing radiosonde data be conducted to determine the rms error with which density can be estimated at the 8-km "isopycnic" layer, as a function of latitude and

season. Also, that existing and new data (from dustsondes, lidar, and satellites) be surveyed to estimate how often significant aerosol and cloud contamination occurs at this level.

- A study be conducted to explore the use of three-wavelength lidar data (with conventional density data) in the lower troposphere to estimate aerosol size distributions and backscatter-to-mass conversion factors.
- A study be conducted to determine whether the wavelength-dependence ratio $\Psi [\equiv B_p(0.355 \mu\text{m})/B_p(1.064 \mu\text{m})]$ can be estimated to better than the $\pm 100\%$ accuracy assumed in this study by using
 - Height information together with previous data on the expected height-dependence of Ψ .
 - Information on $B_p(0.532 \mu\text{m})$.
- The existing simulation code be improved to
 - Make input parameters easier for the user to locate and understand.
 - Handle random errors that produce a negative inferred signal.
 - Include effects of NO_2 absorption.

C. Correlative Sensors

We recommend that the following correlative sensors be operated in conjunction with the shuttle lidar, both to augment the scientific data set and to validate the lidar data:

- On the Shuttle:
 - A radiometer of the Earth Radiation Budget type, to measure radiative effects of aerosol and cloud layers detected by the lidar.
 - A cloud physics radiometer,⁵ to compare passively inferred cloud properties (height, phase, temperature, optical thickness) with those inferred by lidar.
 - A temperature profiling radiometer, to permit comparisons of lidar and passively inferred temperature profiles, and studies of aerosol and cloud effects on each.
 - One or more surface property sensors, such as a Coastal Zone Color Scanner or a Landsat Mapper, to study effects of aerosols and thin clouds on measured radiances and inferences.
- Elsewhere:
 - Radiosondes, to measure temperature and density profiles for comparison to model, interpolated, and lidar-derived profiles.

- Dustsondes, to measure stratospheric and upper tropospheric aerosol profiles.
- Ground-based and airborne lidars, to measure clouds, density, and temperature.
- In situ aerosol samplers (impactors, filters), to determine aerosol optical microproperties (size distribution, composition, shape).
- Satellite limb-scanning aerosol radiometers (such as SAGE II), to measure aerosol extinction profiles.

REFERENCES

1. Shuttle Atmospheric Lidar Research Program--Final Report of Atmospheric Lidar Working Group. NASA SP-433, 1979.
2. Greco, R.V.: Atmospheric Lidar Multi-User Instrument System Definition Study. NASA CR-3303, 1980.
3. Russell, P.B.; Swissler, T.J.; and McCormick, M.P.: Methodology for Error Analysis and Simulation of Lidar Aerosol Measurements. Appl. Opt., vol. 18, no. 22, Nov. 15, 1979, pp. 3783-3797.
4. Evans, W.E.: Design of an Airborne Lidar for Stratospheric Aerosol Measurements. NASA CR-145179, 1977.
5. Kyle, H.L.; Curran, R.J.; Barnes, W.L.; and Escoe, D.: A Cloud Physics Radiometer. Preprints, Third Conference on Atmospheric Radiation, Amer. Meteor. Soc., June 1978, pp. 107-109.

Part 2

ORBITING LIDAR SIMULATIONS:
AEROSOL AND CLOUD MEASUREMENTS
BY AN INDEPENDENT-WAVELENGTH TECHNIQUE

I INTRODUCTION

Previous studies have considered the use of an orbiting lidar to make aerosol and cloud measurements. Several of these studies¹⁻⁶ have estimated the measurement accuracy of lidar return signals for various orbital altitudes, lidar parameters, and atmospheric conditions and illuminations. However, to date, no quantitative studies have shown the accuracy with which cloud and aerosol backscattering profiles, and other parameters such as extinction and mass, could be retrieved from the lidar signal profiles for a variety of realistic scenarios.

The difference between signal-measurement accuracy and particle-retrieval accuracy is often crucial. For example, typical lidar parameters and atmospheric conditions often yield lidar signal profiles that are more accurate at midvisible wavelengths than in the near-infrared; nevertheless, errors in gas backscattering and atmospheric transmission often yield particle backscatter information that is far less accurate in the midvisible than the near-IR, in spite of the more accurate mid-visible signals. Other degradations are also possible. Because studies of aerosol and cloud formation, transport, and radiative and climatic effects will use the retrieved particle profiles, rather than lidar signal profiles, it is important to estimate the quality of these retrieved profiles in judging the utility of shuttle lidar measurements.

This paper presents the results of simulated lidar measurements and retrievals for several realistic combinations of lidar parameters, aerosol and cloud profiles, background lighting conditions, and retrieval error sources. These results not only quantify the expected errors in retrieved data, but also highlight areas that require early hardware development or further study.

We refer to the simulations presented here as "independent-wavelength" simulations. This terminology describes retrievals in which the lidar data are analyzed independently at each wavelength, even though other lidar wavelengths might be producing data simultaneously. An analysis technique that combines signal profiles from two or more wavelengths to retrieve gas density, temperature, aerosol, and cloud information is described and simulated in a companion paper.⁶ In both this and the companion paper we have taken care to make the simulated analysis techniques as similar as possible to techniques used with actual lidar data in the past, and to include error sources that realistically mimic those encountered in actual measurements and retrievals.

II SUMMARY OF SINGLE-WAVELENGTH AEROSOL LIDAR ERROR ANALYSIS METHOD

The error analysis method used here and described in a previous paper⁷ is based on the scattering-ratio/normalization method of lidar calibration and data analysis. This method has been used, in varying forms, in many lidar studies.⁸⁻²⁰ Here, we summarize the analysis method and the resulting algebraic error expressions.

A fundamental quantity that occurs in this analysis method is the scattering ratio, defined by

$$R(\lambda, z) \equiv \frac{B_p(\lambda, z) + B_g(\lambda, z)}{B_g(\lambda, z)} = 1 + \frac{B_p(\lambda, z)}{B_g(\lambda, z)}, \quad (1)$$

where B_p and B_g are the particulate and gaseous backscattering coefficients, respectively, at wavelength λ and height z . As shown in detail elsewhere,⁷ the scattering ratio is related to backscattered lidar signal $S(\lambda, z)$ as

$$R(\lambda, z) = \frac{(z - z_L)^2 S(\lambda, z)}{K(\lambda) Q^2(\lambda, z, z_L) D(z)}, \quad (2)$$

where z_L is the lidar altitude, $K(\lambda)$ is a calibration constant, $Q^2(\lambda, z, z_L)$ is the two-way transmission between the lidar and height z , and $D(z)$ can be any constant multiple of the atmospheric density profile.

In solving Eq. (2), the backscattered signal $S(\lambda, z)$ must first be obtained from the total detector output $V(\lambda, z)$ by subtracting the (internal plus external) background $G(\lambda)$, i.e.,

$$S(\lambda, z) = V(\lambda, z) - G(\lambda) \quad . \quad (3)$$

Thereafter, the calibration constant $K(\lambda)$ is usually fixed by assuming that at the height z^* where Eq. (2) attains its minimum value $R_{\min}(\lambda)$, gas backscattering dominates particulate backscattering, implying that R_{\min} is close to unity (and hence can be estimated with relatively small error--see Section IV-D-4).

This calibration procedure yields the expression from which $R(\lambda, z)$ is obtained in practice:

$$R(\lambda, z) = \frac{(z - z_L)^2 S(\lambda, z) Q^2(\lambda, z_L, z^*) D(z^*)}{(z^* - z_L)^2 S(\lambda, z^*) Q^2(\lambda, z_L, z) D(z)} R_{\min}(\lambda) \quad , \quad (4)$$

or

$$R(\lambda, z) = \frac{h(z - z_L, z^* - z_L) s(\lambda, z, z^*)}{q(\lambda, z, z^*) d(z, z^*)} R_{\min}(\lambda) \quad , \quad (5)$$

where

$$h(z - z_L, z^* - z_L) \equiv \frac{(z - z_L)^2}{(z^* - z_L)^2} \quad , \quad (6)$$

$$s(\lambda, z, z^*) \equiv \frac{S(\lambda, z)}{S(\lambda, z^*)} \quad , \quad (7)$$

$$q(\lambda, z, z^*) \equiv \frac{Q^2(\lambda, z_L, z)}{Q^2(\lambda, z_L, z^*)} = \exp \left\{ \pm 2 \left[\int_z^{z^*} E(\lambda, z') dz' \right] \right\}, \quad (8)$$

$$d(\lambda, z, z^*) = \frac{D(z)}{D(z^*)}, \quad (9)$$

and $E(\lambda, z)$ is the atmospheric extinction coefficient. In Eq. (8), the + (-) sign applies to an upward- (downward-) viewing lidar.

Once $R(\lambda, z)$ has been obtained from Eq. (5), and $B_g(\lambda, z)$ has been obtained as described below, we can derive particulate backscattering by rearranging Eq. (1) to yield

$$B_p(\lambda, z) = B_g(\lambda, z) [R(\lambda, z) - 1]. \quad (10)$$

In turn, the aerosol and cloud quantities required in climatic and environmental studies (e.g., particulate optical thickness, albedo, heating rate, mass) can be derived from $B_p(\lambda, z)$ by using optical model conversion factors. As is well known, these conversion factors can vary widely when the model size, composition, and shape distributions are undefined; however, in some cases knowledge of $B_p(\lambda, z)$ at two or more wavelengths might usefully constrain the possible range of optical models.

In solving Eqs. (3) through (10), $D(z)$ --and hence $B_g(z)$ --is usually obtained from nearby meteorological data; $E(\lambda, z)$ --hence $Q^2(\lambda, z, z_L)$ --is usually provided by a model (often improved by using lidar data); $R_{\min}(\lambda)$ is usually assumed to be unity or is estimated from previous aerosol data and other factors. Errors in these quantities and assumptions, plus errors in the detector outputs $V(\lambda, z)$ and $G(\lambda)$ --hence in $S(\lambda, z)$ --produce corresponding errors in $R(\lambda, z)$, $B_p(\lambda)$, and the other aerosol and cloud parameters derived from these results. Conventional

error-propagation analysis⁷ has shown that the resulting 1 σ relative uncertainties in R and B_p are given by

$$\left(\frac{\delta R}{R}\right)^2 = \left(\frac{\delta s}{s}\right)^2 + \left(\frac{\delta q}{q}\right)^2 + \left(\frac{\delta D}{D}\right)^2 + \left(\frac{\delta D^*}{D^*}\right)^2 - 2 \frac{C_{DD}^2}{DD^*} + \left(\frac{\delta R_{\min}}{R_{\min}}\right)^2 \quad (11)$$

and

$$\left(\frac{\delta B_p}{B_p}\right)^2 = \left(\frac{B_g}{B_p}\right)^2 \left\{ \left[\left(\frac{\delta s}{s}\right)^2 + \left(\frac{\delta q}{q}\right)^2 + \left(\frac{\delta R_{\min}}{R_{\min}}\right)^2 + \left(\frac{\delta \rho^*}{\rho^*}\right)^2 - 2 \frac{C_{\rho\rho}^2}{R\rho\rho^*} \right] R^2 + \left(\frac{\delta \rho}{\rho}\right)^2 \right\}, \quad (12)$$

where ρ and ρ^* are the absolute gas densities at heights z and z^* , respectively, δx is the 1 σ uncertainty in each variable x ,

$$\rho^* \equiv \rho(z^*) \quad , \quad (13)$$

C_{DD}^2 is the covariance between D and D^* , and similarly for $C_{\rho\rho}^2$. [These covariances can usually be assumed to vanish except for $|z - z^*| < \Delta z$, where Δz is the vertical resolution of the input density profile. If $z = z^*$, then $C_{DD}^2 = (\delta D^*)^2$. However, if the density profile $\rho(z)$ contains a systematic bias error, then $C_{\rho\rho}^2$ is nonzero at all heights. See Ref. 7 for details.]

These results show that errors in determining the backscattered lidar signal [symbolized by δs in Eqs. (11) and (12)] are but one of four sources of error in determining the retrieved cloud and aerosol quantities, R and B_p . Errors in transmission (δq), gas density (δD), and lidar calibration (δR_{\min}) also occur and often dominate signal errors. Also, when $B_p/B_g \ll R$, uncertainties in retrieved B_p , from any

of the four sources, are proportional to B_g/B_p . Thus, if other factors are equal, any increase of B_p/B_g (and hence of R) up to the point where $B_p/B_g \approx R$ tends to reduce errors in retrieved B_p .

III SIMULATION PROCEDURE

To test the uncertainty expressions of Eqs. (11) and (12), and also to develop insights and data analysis software, we developed a procedure (and computer code) to simulate the lidar measurement and retrieval process. The simulation procedure, described in detail elsewhere,⁷ is illustrated in Figure 1. Given a set of inputs specifying lidar parameters, atmospheric backscattering and extinction profiles (gaseous and particulate), and background lighting, the code computes profiles of expected return signals and backgrounds. Then, random number generators inject random errors of appropriate size at each step of the measurement and retrieval sequence. The resulting profiles are compared to the input model profiles to see whether differences between the two are consistent with the algebraic uncertainty expressions, Eqs. (11) and (12). If desired, each simulation can be repeated an arbitrary number of times, using different random errors (drawn from the same distributions); thereafter, root-mean-square (rms) differences between the set of retrieved profiles and the model profile are computed. The rms difference profile provides a more stable result for comparison with the algebraic 1 σ uncertainties, Eqs. (11) and (12).

The simulation code also separates the algebraic uncertainties by source, as an aid in identifying the dominant sources for each measurement height and associated set of conditions.

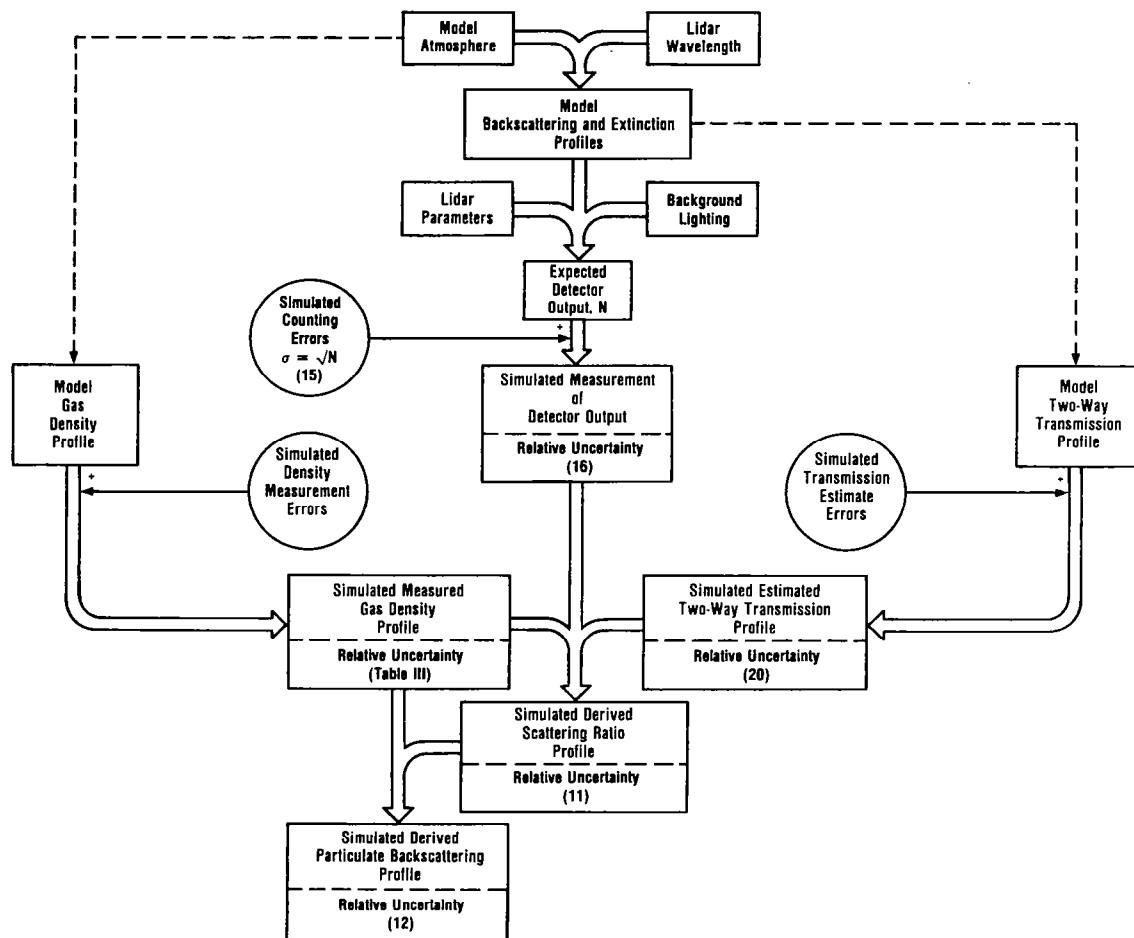


FIGURE 1 SIMULATION PROCEDURE FOR EVALUATING LIDAR MEASUREMENT AND RETRIEVAL ERRORS

Circles symbolize random number generators that inject simulated errors into derived quantities at appropriate steps. Numbers in parentheses indicate equations and tables in the text.

IV SIMULATION INPUTS

A. Atmospheric Models

The dependence of measurement and retrieval error on lidar wavelength, background lighting, density errors, and other factors is strongly determined by the particle and gas models used for input. For example, the wavelength dependence of particulate backscattering (along with other factors) determines whether it is advantageous to use alternate lidar wavelengths. Also, a strongly absorbing variable gas can produce significant transmission errors at its absorbing wavelengths. Moreover, model particle concentrations that give unrealistically large or small values for B_p/B_g can yield unrealistically small or large relative errors in retrieved B_p [cf. Eq. (12)].

For these reasons we developed a set of input atmospheric models, each based on optical and physical measurements, as well as formation, transport, and removal processes that have been previously documented in the literature. In addition, we compared the resulting model backscatter profiles at a wavelength of $0.694 \mu\text{m}$ with previous ruby lidar measurements, and ascertained that the model results were within the typical measurement range for the atmospheric regions and conditions they were intended to represent. For flexibility in simulating special situations, each model component can be multiplied by an arbitrary factor over an arbitrary height range.

The resulting atmospheric models have cloud and aerosol backscatter-to-extinction ratios, as well as wavelength dependences, that vary with height, latitude, and particle source (e.g., volcanic, Saharan, marine) in accordance with the assumed particle size distribution, composition, and shape. The models, which include molecular density, ozone, cirrus and noctilucent clouds, and mesospheric, stratospheric, upper tropospheric, Saharan, and marine aerosols, are described

in Appendix A. Figures 2(a) through 4(a) show the composite model profiles of backscatter mixing ratio (B_p/B_g) that we will use for the simulations in this paper. The associated signal profiles are discussed in Section V-A.

As explained more fully in Appendix A, the inclusion of mesospheric aerosol layers in our models is not intended to suggest that such layers are always, or even typically, present. Rather, the intent is to construct model layers that are consistent with several previous measurements (and transport processes), and then to see how well the orbiting lidar could detect such layers if indeed they were present. Also, we have emphasized marine aerosol models over continental ones because a major strength of any orbiting lidar will be its ability to fill data gaps over the world's vast ocean areas. Note that the marine aerosol models do include particles of continental origin (see Appendix A).

B. Lidar Parameters

The intent of this study is to simulate measurements made by a first-generation spaceborne lidar, flying on the space shuttle and using straightforward measurement techniques with a history of analogous measurements on earth. Therefore, we adopted the parameters of the baseline shuttle lidar determined in a recent facility definition study⁴ by General Electric. These parameters, listed in Table 1, satisfy the following criteria:

- They are compatible with the weight, power, safety, and other restrictions for shuttle science payloads.
- They satisfy a set of preliminary eye safety guidelines developed by General Electric.*

*These guidelines⁴ assume the ANSI criteria for maximum permissible ocular exposure, viewing with the naked eye by day and with a 10-inch telescope by night, a safety factor of 10 for laser beam scintillation effects, and an additional factor of 2 or 3 to account for the difference between average and peak laser energies in Gaussian or multimode laser beams, respectively.

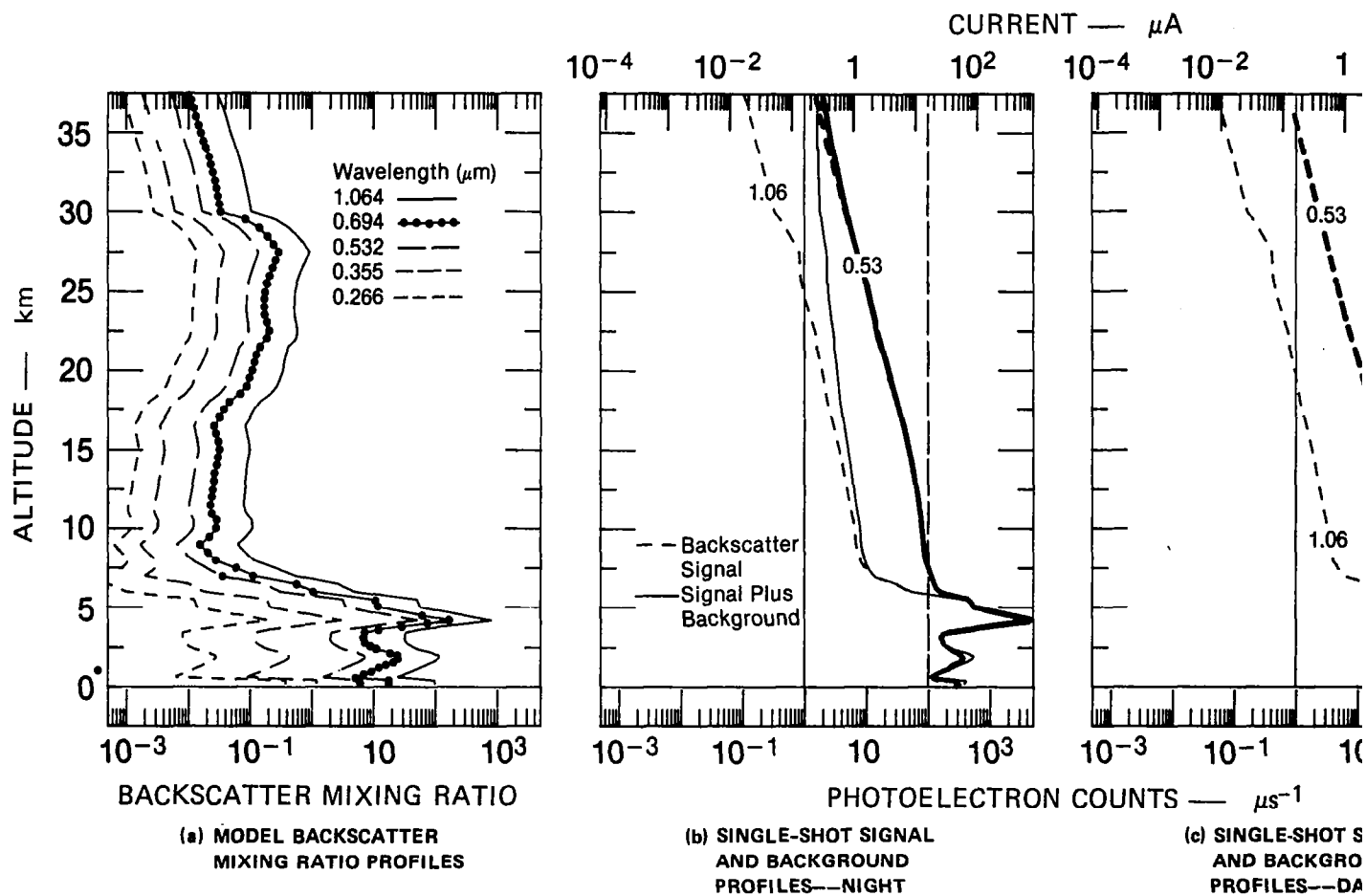


FIGURE 2 MODEL BACKSCATTER MIXING RATIO PROFILES, SINGLE-SHOT SIGNAL AND BACKGROUND PROFILES FOR LOW LATITUDE

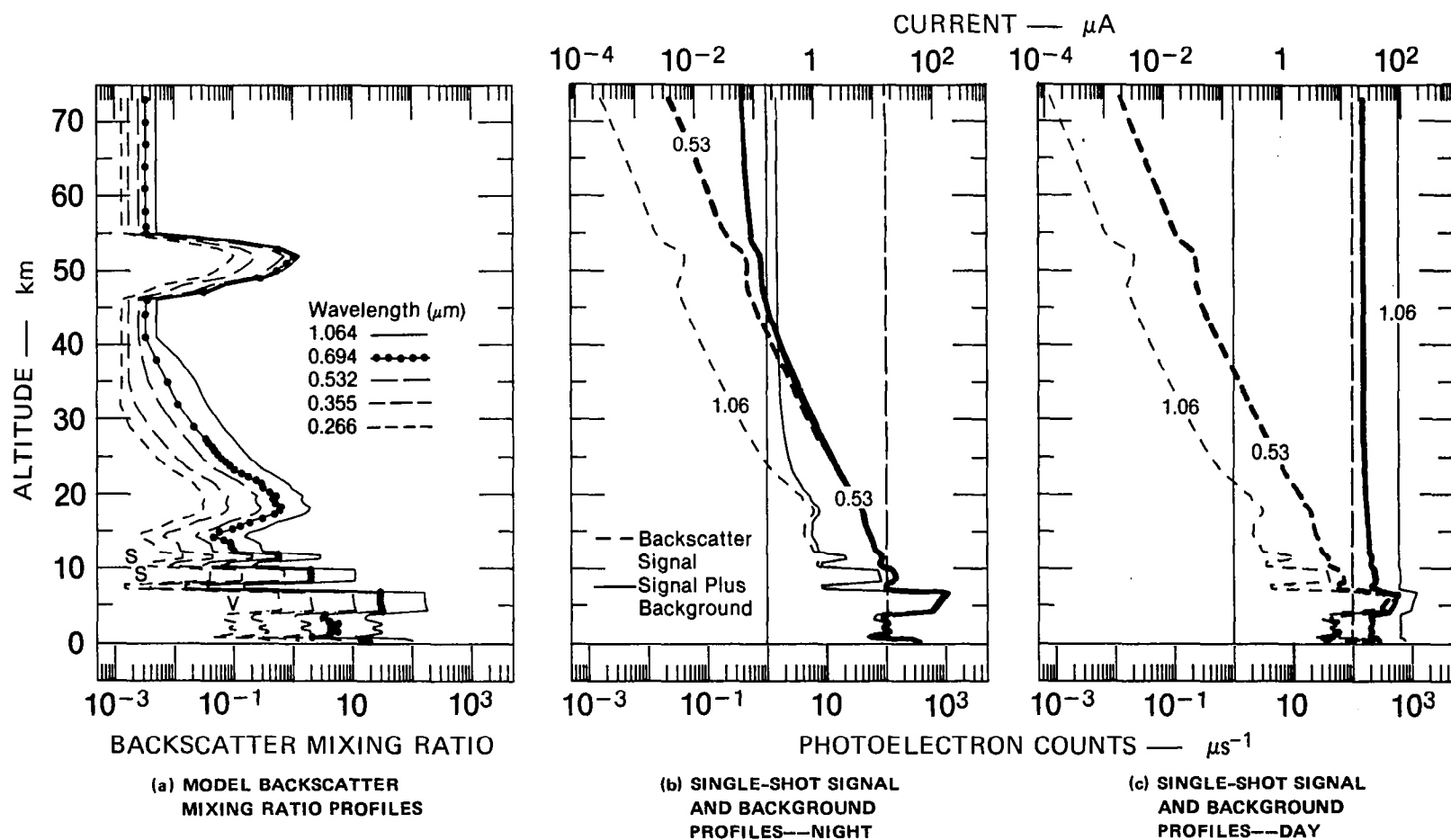


FIGURE 3 MODEL BACKSCATTER MIXING RATIO PROFILES, SINGLE-SHOT SIGNAL AND BACKGROUND PROFILES FOR MIDDLE LATITUDE

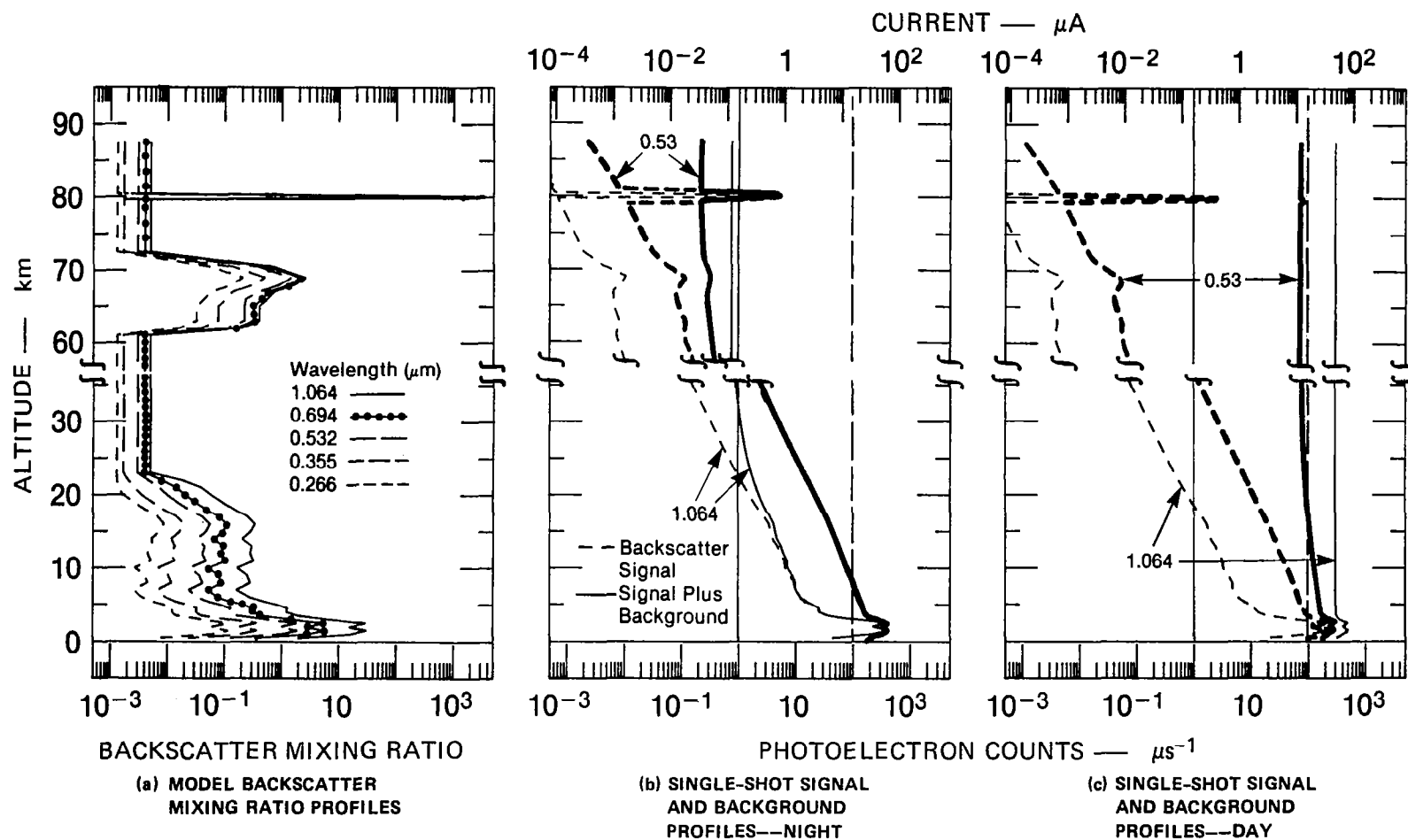


FIGURE 4 MODEL BACKSCATTER MIXING RATIO PROFILES, SINGLE-SHOT SIGNAL AND BACKGROUND PROFILES FOR HIGH LATITUDE

Table 1

ASSUMED LIDAR PARAMETERS

Parameter	Wavelength, λ (μm)		
	1.064	0.532	0.355
Transmitter			
Pulse energy (J, simultaneous)	1.1	0.55	0.20
Repetition rate (s^{-1})	10	10	10
Full beamwidth (mr)	5^* , 0.4^\dagger	5^* , 0.4^\dagger	5^* , 0.4^\dagger
Receiver			
Diameter (m)	1.25	1.25	1.25
Full beamwidth (mr)	5.5^* , 0.5^\dagger	5.5^* , 0.5^\dagger	5.5^* , 0.5^\dagger
Filter bandwidth (nm)	4.0^* , 0.4^\dagger	0.2^* , 0.02^\dagger	4.0^* , 0.4^\dagger
Filter transmission	0.50^* , 0.25^\dagger	0.50^* , 0.25^\dagger	0.20^* , 0.10^\dagger
Overall transmission	0.34^* , 0.17^\dagger	0.25^* , 0.12^\dagger	0.10^* , 0.05^\dagger
Quantum efficiency	0.04	0.20	0.30
Detector dark counts (μs^{-1})	0.03	0.03	0.03
Detector gain	10^6	10^6	10^6
Altitude, 300 km			

* Nighttime configuration.

† Daytime configuration.

- All three wavelengths, though transmitted simultaneously, are obtained from a single Nd:YAG laser. This type of laser has been highly engineered recently for flight applications, ruggedness, and efficiency.
- No special tuning, line narrowing, or wavelength stability is required for either the transmitter or the receiver.

In sum, the lidar parameters define a baseline spaceflight system. Nevertheless, certain engineering issues remain to be resolved regarding frequency tripling and automatic changing of receiver field of view and filter bandwidth when crossing from dark to daylight areas and back.

C. Background Lighting

To give an idea of the wide range of possible background lighting conditions, we have chosen three sets of scenarios: sunlit cloud, sunlit ocean, and full moonlit cloud, each with the illuminating source (sun or moon) at zenith angle θ_0 . For our purposes both clouds and the ocean can be modeled as Lambertian reflectors--i.e., reflected radiance $I_B(\lambda)$ can be modeled as independent of the angle of emergence. This yields, for the spectral radiance $I_B(\lambda)$ emerging toward the zenith,

$$I_B(\lambda) = A F(\lambda) \cos \theta_0 / \left(\int_0^{2\pi} d\phi \int_0^{\pi/2} \cos \theta \sin \theta d\theta \right)$$

$$= A F(\lambda) \cos \theta_0 / (\pi \text{ sr}) \quad (14)$$

where A is the cloud or ocean albedo and $F(\lambda)$ is the solar (or lunar) spectral irradiance.²¹ Note that we do not decrease $I_B(\lambda)$ by a clear-atmosphere, two-way transmission or increase $I_B(\lambda)$ by the clear-atmosphere reflectivity. These two factors tend to cancel; moreover, their inclusion is not warranted, given the approximations already made in the value and spectral and angular dependence of cloud and ocean reflectivity. (Also, our simulation results below 20 km are not

sensitive to changes in background by factors of 3 or less.) Table 2 shows results of Eq. (14) for the three chosen scenarios.

Table 2

BACKGROUND LIGHTING (ZENITH UPWARD SPECTRAL RADIANCE)
FOR A DOWNWARD-VIEWING LIDAR AND SEVERAL SCENARIOS*

λ (μm)	I_B ($\text{mW m}^{-2} \text{ sr}^{-1} \text{ nm}^{-1}$)		
	Sunlit Cloud ($A = 0.8$)	Sunlit Ocean ($A = 0.1$)	Moonlit Cloud ($A = 0.8$)
1.064	168	22	168×10^{-6}
0.532	460	58	460×10^{-6}
0.355	280	34	280×10^{-6}

* Calculated from Eq. (14) assuming the solar spectral irradiances $F(\lambda)$ of Thekaker²¹ and $\cos \theta_0 = 1$.

D. Error Sources

1. Signal

In most cases the wide dynamic range of backscattered signal profiles received by a spaceborne lidar will produce a detector output that must be measured partly in the pulse-counting mode and partly in the current mode; the resulting two profile parts must be accurately spliced together (see Section V-A-1, V-B-1). In the pulse-counting mode the lo

uncertainty in the number of signal counts, N_S (per range element), is given by

$$\left(\frac{\delta S}{S}\right)_{pc} = \frac{\delta N_S}{N_S} = \frac{\sqrt{N_S + N_B + N_D}}{N_S}, \quad (15)$$

where N_B and N_D are the number of output counts arising from background lighting and internal detector noise, respectively. [This assumes that $N_B + N_D$ is determined accurately enough that its uncertainty is negligible compared to Eq. (15). See Ref. 7 for details.] In the current mode, errors are caused by factors such as detector shot noise and saturation, amplifier noise and nonlinearity, and digitizer truncation and saturation. If gain switching or logarithmic amplifiers are used to compress the dynamic range of detector output, additional error sources are introduced. Finally, matching the counting and current parts of the output profile becomes another error source. These errors must be reduced to acceptable levels if detector outputs from the spaceborne lidar are to be useful over all height regions of interest. This problem has been solved for certain height ranges by using a variety of techniques in many ground-based and airborne lidar systems. However, each technique has its own error characteristics, and it is not clear which technique, or possibly a new technique,²² would be used for a shuttle lidar system.

In our simulation program we have confronted this simulation problem in the following manner. At each measurement height, N_S is calculated from the lidar equation as shown in Ref. 7, and N_B and N_D are calculated from the background-lighting, receiver, and detector characteristics. The pulse-counting value for $\delta S/S$, Eq. (15), is then calculated. As N_S increases, this result decreases toward zero. However, it is clear that increasing N_S also leads to pulse overlap, making pulse-counting impossible, and forcing signal measurement into the current mode. At that point, the current-measurement and transition errors mentioned above take over, and Eq. (15) is no longer a valid expression of

total signal uncertainty. Since no universally valid expression describes the current-mode errors mentioned above, our program uses

$$\frac{\delta S}{S} = \text{MAX} \left[\left(\frac{\delta S}{S} \right)_{\text{pc}}, \left(\frac{\delta S}{S} \right)_{\text{min}} \right] . \quad (16)$$

That is, whenever the photon-counting expression becomes less than a prespecified minimum, $(\delta S/S)_{\text{min}}$, that minimum is used for $(\delta S/S)$. This assumes that the shuttle lidar hardware can measure the current-mode part of the output profile and splice it to the pulse-counting part with the accuracy $(\delta S/S)_{\text{min}}$. To highlight the importance of this assumption, the program plots profiles of expected detector output (backscattered signal and background) as a function of height, in terms of both pulse rate and anode current, relative to certain detector benchmarks, such as the point where pulse overlap becomes highly likely and the point where current measurements become sufficiently accurate. (The benchmarks are the 1- and 100-count μs^{-1} lines in Figures 2 through 4.)

These plots can then be used in designing signal-processing and recording hardware that satisfy the $(\delta S/S)_{\text{min}}$ requirement.

For the simulations reported here, we used

$$\left(\frac{\delta S}{S} \right)_{\text{min}} = 0.005 . \quad (17)$$

Although this requirement is stringent, we feel it is attainable using the technique described by Evans.²² Relaxing this requirement to 0.01 would have little effect on the aerosol and cloud simulations shown in this part; however, it would significantly increase the minimum density and temperature errors shown in Part 3. (See also Section V-A of this part.)

Finally, we require an expression for $\delta s/s$ to use in Eqs. (11) and (12). From Eq. (7) it follows that

$$\left(\frac{\delta s}{s}\right)^2 = \left(\frac{\delta S}{S}\right)^2 + \left(\frac{\delta S^*}{S^*}\right)^2, \quad (18)$$

where

$$S^* \equiv S(\lambda, z^*) \quad (19)$$

2. Molecular Density

The problem of obtaining molecular density information from conventional meteorological sources (radiosondes, satellites, and rocketsondes) is discussed in Ref. 7. From a radiosonde ascent, density profiles can be determined with an accuracy of about 1 percent. However, since most shuttle lidar data will come from remote regions of the globe (e.g., the large ocean areas not covered by radiosondes), one must assume that current radiosonde density data will not be available for most shuttle lidar data. The alternative sources of conventional information are:

- Carefully selected seasonal and regional model density profiles.
- Density profiles obtained from current satellite and radiosonde network analyses and historical rocketsonde data using hydrodynamically consistent interpolation methods.

The quality of such density profiles has recently been evaluated by National Weather Service personnel in connection with the SAM II and SAGE satellite programs (which require density profiles in remote areas for input to routine data analysis). These evaluations (Ref. 23, Appendix D, by J. Laver) show that expected density errors depend in a fairly complicated way on height, the time difference between the lidar measurement and the conventional analyses, the hemisphere of the lidar measurement, and even the latitude within the southern hemisphere. However, for purposes of this study, representative values can be

summarized as in Table 3. The indicated $\delta D/D$ values were used for the simulations reported here. The expression given by Ref. 7 was used for C_{DD}^* .

Table 3

REPRESENTATIVE 1 σ UNCERTAINTIES IN DENSITY PROFILES
DERIVED FROM CONVENTIONAL SOURCES
Values apply to densities defined at
geometric (not pressure or geopotential) height

Data Source/z	0-30 km (%)	30-50 km (%)	50-90 km (%)
Radiosonde measurement within 100 km and 6 h (no intervening frontal activity)	1	--	--
Hydrodynamically consistent interpolation of current radiosonde and satellite data, plus historical rocketsonde data, in data- sparse area	2	3 to 5	10
Regional and seasonal models	3	5	10

* The uncertainties used for the simulations in this paper are:

Low-latitude: 2% below 30 km, 3% above.

Mid-latitude: 3% below 40 km, 10% above.

High-latitude: 3% below 40 km, 10% above.

3. Transmission

As shown in Ref. 7, transmission uncertainties for the wavelengths of interest are given by

$$\left(\frac{\delta q}{q}\right)^2 = 4 \left\{ \left[\delta \tau_p(\lambda, z, z^*) \right]^2 + \left[\delta \tau_{sg}(\lambda, z, z^*) \right]^2 + \left[\delta \tau_3(\lambda, z, z^*) \right]^2 \right\}, \quad (20)$$

where $\tau_x(\lambda, z, z^*)$ is the optical thickness of constituent/mechanism x between heights z and z^* ; and p , sg , and 3 denote (cloud and aerosol) particles, total gaseous scattering, and ozone absorption, respectively. (As recently pointed out by Young,²⁴ τ_{sg} includes Raman and Brillouin scattering as well as Rayleigh scattering.) For the reasons cited in Ref. 7, we use

$$\delta\tau_3(\lambda, z, z^*) = 0.2\tau_3(\lambda, z, z^*) \quad . \quad (21)$$

Ref. 7 uses the conservative overestimate

$$\delta\tau_{sg}(\lambda, z, z^*) = 0.1\tau_{sg}(\lambda, z, z^*) \quad . \quad (22)$$

for gaseous scattering optical thickness uncertainties. However, this overestimate becomes important at the short wavelength, $0.355 \mu\text{m}$.

Therefore, we now use the more exact expression

$$\delta\tau_{sg}(\lambda, z, z^*) = \left[\delta\Delta P(z, z^*) / \Delta P(z, z^*) \right] \tau_{sg}(\lambda, z, z^*) \quad , \quad (23)$$

where $\Delta P(z, z^*)$ is the pressure difference between z and z^* . In lidar data analysis the pressure difference is obtained from the molecular density profile, and thus the pressure difference uncertainty, $\delta\Delta P(z, z^*)$, is a function of the molecular density uncertainty profile, $\delta\rho(z)$. Our simulation program obtains $\delta\Delta P(z, z^*)$ from the $\rho(z)$ and $\delta\rho(z)$ profiles using error-propagation techniques described in the companion paper.⁶

For the reasons described in Appendix B, we retain the expression

$$\delta\tau_p(\lambda, z, z^*) = 0.5 \left\{ \left[\tau_{ap}(\lambda, z, z^*) \right]^2 + \left[\tau_{cp}(\lambda, z, z^*) \right]^2 \right\}^{1/2} \quad (24)$$

used in Ref. 7.

Note that Eq. (20) includes no term to describe NO₂ absorption effects. We intend to add such a term in the future and to include typical NO₂ profiles in our atmospheric models as better data become available. However, for the present we have calculated the error incurred by neglect of NO₂ in Eq. (20). As inputs, we used the NO₂ profiles summarized by Noxon²⁵ and the absorption coefficients reviewed by Hudson.²⁶ Taking a worst case of nighttime midlatitude conditions, with an uncertainty in NO₂ concentrations of ± 100 percent between 5 and 20 km and ± 50 percent between 20 and 35 km, led to the following results for $(\delta q/q)_{\text{NO}_2}$ at wavelength 0.355 μm :

z (km)	z^* (km)	$(\delta q/q)$ NO ₂
5	8	0.0002
20	8	0.0008
28	8	0.0016
35	8	0.0026

These values are small compared to the other terms in Eqs. (20), (11), and (12). Moreover, for daytime, lower latitudes, and the longer wavelengths used in this study, $(\delta q/q)_{\text{NO}_2}$ values are even less.²⁵

4. R_{min}

Reference 7 discusses the problem of determining expectation values $\langle R_{\text{min}} \rangle$ and uncertainties δR_{min} as a function of latitude, lidar analysis height range, volcanic effects, and other factors. That study shows that $\langle R_{\text{min}} \rangle$ and δR_{min} can be estimated from the large set of particle number profiles measured by balloonborne particle counters at sites distributed from 90°S to 84°N in the past 12 years, provided the particle number data are combined with realistic models of relative size distribution and composition. As an example, Ref. 7 presents values of $\langle R_{\text{min}} \rangle$ and δR_{min} using model size distributions and compositions that are appropriate for particles in and near the peak of the stratospheric aerosol layer.

Since that work was done, it has become clear that significantly different types of size distribution, and different compositions, should be used to describe aerosols in the upper troposphere, where R_{\min} is frequently found. Using such a height-dependent optical model with the particle number profiles tends to increase the results for $\langle R_{\min} \rangle$ and δR_{\min} found in Ref. 7. While the scope of this study does not permit us to derive a complete new set of $\langle R_{\min} \rangle$, δR_{\min} values to replace those in Ref. 7, we have nonetheless performed sample calculations suggesting that the revised optical model increases the $\langle R_{\min} - 1 \rangle$ and δR_{\min} values of Ref. 7 by about a factor of 2. (However, in northern high latitudes, the values in Ref. 7 practically unaffected, because R_{\min} rarely occurs in the troposphere for such latitudes.) For the current simulation study, we feel that it is sufficiently accurate to use $\langle R_{\min} - 1 \rangle$ and δR_{\min} values that are double those of Ref. 7, with the high-latitude exception just noted. However, because of the importance of R_{\min} to all lidar results derived by the scattering ratio/normalization method [cf. Eq. (5)], we emphasize that analyses of actual lidar data should take care to estimate the best possible values for $\langle R_{\min} \rangle$ and δR_{\min} for the conditions under which the data were taken.

The results in this section reinforce a conclusion of Ref. 7, namely that a carefully estimated value for $\langle R_{\min} \rangle$ is in many cases significantly more accurate than the common assumption of $R_{\min} = 1$, and can significantly improve the accuracy of retrieved lidar data products over large height ranges. In fact the results of this section suggest that the error in using $R_{\min} = 1$ is about double that previously thought.

V SIMULATION RESULTS

A. Signal and Background Profiles

Figures 2 through 4 show single-shot profiles of signal and signal plus background for the lidar parameters of Table 1 and the three associated model atmospheres each for a nighttime and a daytime condition. The detector outputs have been expressed both as photoelectron counts per microsecond and as microamperes, assuming a detector internal gain of 10^6 , which is typical for a commercially available photomultiplier recently tested for lidar applications by Evans.²⁷ The solid vertical line in each plot indicates the counting rate at which output pulses (each ~ 20 ns long²⁷) become likely to overlap, thus causing pulse-counting errors. The dashed vertical line indicates the minimum output for which conventional current measurements can be made with the accuracy specified by Eq. (17).

In all cases the dynamic range of the total detector output (signal plus background) in the current-measurement range is less than three orders of magnitude (although the return from the surface or opaque clouds would be considerably larger than the atmospheric returns shown). This behavior contrasts with many ground-based or airborne lidars, which can encounter many decades of signal decrease from the range-squared effect alone. In contrast, for a shuttle lidar altitude of 300 km, range-squared effects vary by less than a factor of 3 between 100 km and the surface, and actually counteract the increase of atmospheric density.

The major problem in accurate measurement of the output profiles is that, at night, all profiles span the transition region between pulse-counting and current measurement. Because of the normalization method assumed here to calibrate received signals in terms of backscattering coefficient, the data acquisition method must accurately splice together

the pulse and current portions of the profile in this transition region. A method for doing this was recently described by Evans,²² but to our knowledge it has not been implemented. As noted in Section IV-D-1, we have assumed that current measurements and a pulse-to-current splice can be made with an accuracy of 0.5 percent. Although we feel that this goal can be met, it is worth emphasizing that this assumption implies a certain amount of hardware development.

B. Retrievals

1. Tropical, Nonvolcanic, Cloud-Free, Saharan

a. Nighttime (Zenith Moonlit Cloud), $\Delta x \approx 200$ km

The model atmosphere used in this scenario [Figure 2(a)] includes no clouds; however, we have used a background radiance appropriate for clouds illuminated by a full, zenith moon (Table 2) to make our results conservative. As can be seen from Figure 3(a), 1.06- μm signal-to-noise ratio [Eq. (15)] above 20 km would improve by assuming less background (e.g., a moonlit ocean); however, the 0.53- μm signal-to-noise ratio is signal-dominated for all heights below 35 km, and hence is insensitive to this assumption.

Figure 5(a,b) shows simulated retrievals for backscatter mixing ratio, assuming the error sources given by Eqs. (15)-(18), (20)-(24), Table 3, and Section IV-D-4, with shots integrated for 28 s (total 280 shots), yielding a horizontal resolution of ~ 200 km for a spacecraft velocity of ~ 7 km s⁻¹. Vertical resolution, shown by the spacing of the dots, is 0.5 km below 20 km and 1 km above, except above ~ 29 km where range bins have been combined to improve the signal-to-noise ratio. The solid curves give the model (i.e., "exact") profile; the dots give the lidar retrieval; and the error bars give the expected 1σ uncertainty calculated from Eqs. (11) or (12). Although for this case the error bars somewhat overestimate the rms difference between the retrieval and the model, close inspection has shown that this was caused by fortuitously small random errors drawn for R_{\min} and transmission in this case.

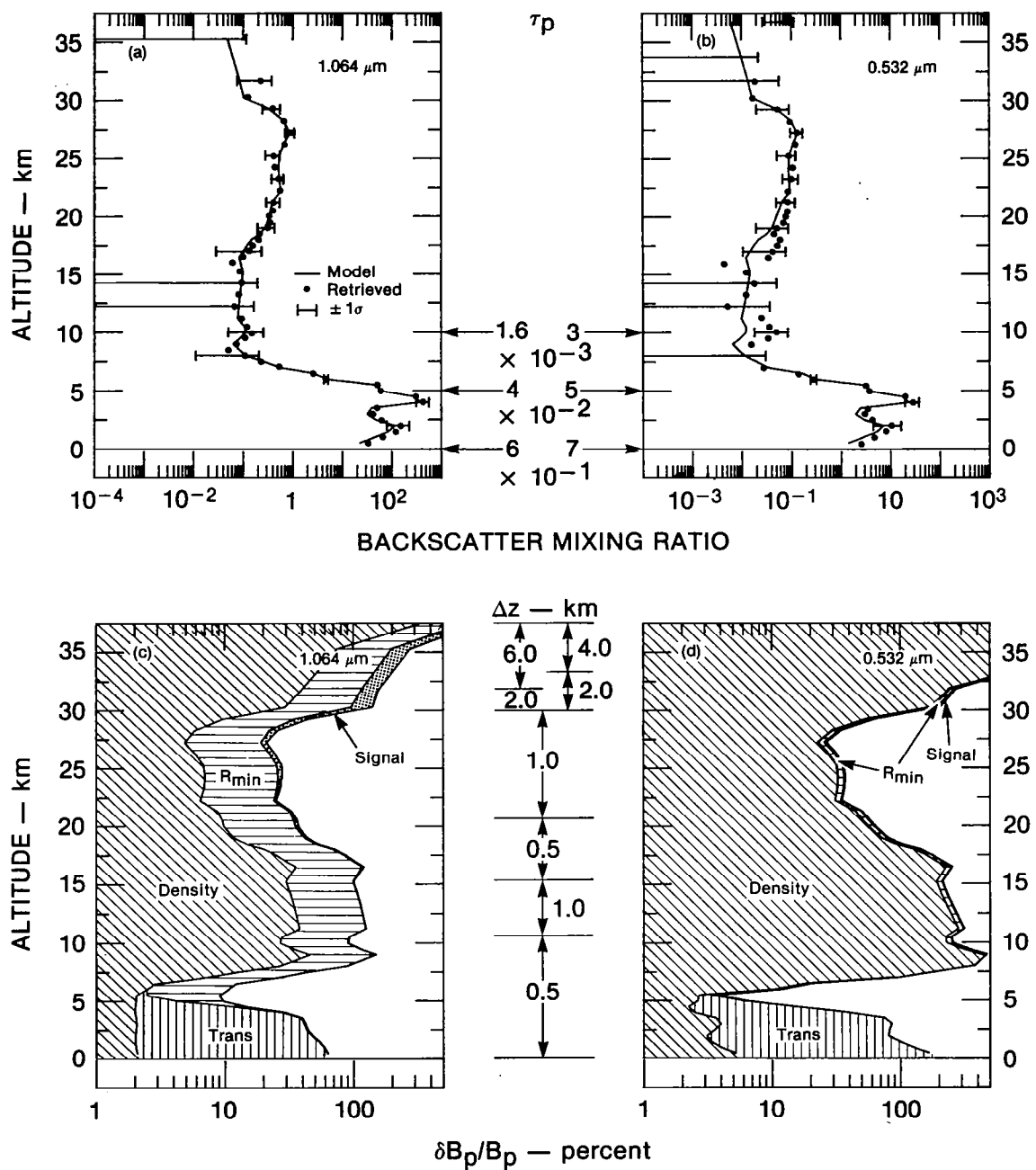


FIGURE 5 LOW-LATITUDE NIGHTTIME SIMULATION RESULTS, 1.064 AND 0.532 μm , USING CONVENTIONAL DENSITY DATA

(a,b) Backscatter mixing ratio profiles; (c,d) Relative uncertainty in particulate backscattering broken down by source.

Many simulations run in this study and previously⁷ have substantiated the validity of the algebraic expressions Eqs. (11) and (12).

For this scenario both wavelengths give quite good retrievals below 7 km and between 22 and 30 km. Between 8 and 20 km, where backscatter mixing ratios are near their minimum, relative uncertainties increase, and the quality of the retrievals is poorer, especially for $\lambda = 0.53 \mu\text{m}$. The reason for this is shown in Figure 5(c,d), where the relative uncertainty in particulate backscattering is broken down by source. For $0.53 \mu\text{m}$, at all heights above 6 km, uncertainties in molecular density are the dominant source of error. This simulation assumes a relative density uncertainty of 0.02 below 30 km, which is appropriate for density profiles in remote areas derived by interpolation from current conventional data. Because the backscatter mixing ratio B_p/B_g at $0.53 \mu\text{m}$ is only about 0.01 to 0.02 between 8 and 20 km, the density uncertainties alone lead to B_p uncertainties of 100 to 200 percent in this region. At $1.06 \mu\text{m}$, backscatter mixing ratios are considerably larger (~ 0.08 to 0.20), and the density-induced relative uncertainty in B_p is proportionately reduced.

Note, however, the greatly increased calibration uncertainty at the longer wavelength, caused by uncertainties in R_{\min} . Uncertainties in $R_{\min}(1.06 \mu\text{m})$ considerably exceed those in $R_{\min}(0.53 \mu\text{m})$, because even very tenuous aerosol layers can perturb $R_{\min}(1.06 \mu\text{m})$ by several percent, whereas the same aerosol layers perturb $R_{\min}(0.53 \mu\text{m})$ much less. (Compare the backscatter mixing ratios in Figure 2.) Thus, at $0.53 \mu\text{m}$, one is more likely to find a "calibration layer" where gas backscattering strongly dominates particle backscattering, thus permitting one to calibrate the entire received signal profile in terms of backscattering coefficient.

Between 7 and 5 km, in the top of the strong Saharan dust layer, relative uncertainties are greatly reduced at both wavelengths because of the sharp increase in B_p . However, with increasing penetration into the Sahara layers, transmission uncertainties begin to degrade the

retrieval, and the overall uncertainty again increases. These transmission errors are discussed in more detail in connection with the next scenario.

Note that signal errors do not make a significant contribution in this scenario, except above ~30 km, especially at 1.06 μm . However, the weaker signals at these heights have had the indirect effect of forcing a coarser vertical resolution there (through rebinning to reduce signal errors). This effect would have become more serious, and penetrated lower, if the integration time (horizontal resolution) had been decreased below 28 s (~200 km).

b. Daytime (Zenith Sunlit Ocean), $\Delta x \approx 100 \text{ km}$

Figure 6 shows simulated retrievals and uncertainty breakdowns for the same model atmosphere as Figures 5 and 2(a), but with the lidar in its daytime configuration (Table 1) and a background radiance that approximates that of a sunlit ocean (Table 2). (The sun is assumed to be near the zenith, but not exactly at the zenith, as this would cause a very large specular reflection into the lidar telescope.) As can be seen from Figure 3(b), signals above 20 km are background-dominated, and no useful retrievals are possible; hence, results are shown only below 20 km on an expanded scale. Note, however, that within the Sahara layer and the underlying marine layer, even the daytime background is small compared to the backscattered signal at both wavelengths. Hence, both vertical and horizontal resolution can be fine. This simulation assumes $\Delta x \approx 100 \text{ km}$ (140 shots, 14 s), with $\Delta z = 0.25 \text{ km}$ below 7 km, and $\Delta z = 1 \text{ km}$ above. (Note, however, the coarser vertical resolution above 10 km for 1.06 μm , caused by rebinning.) The only reason for making Δx as large as 100 km is to provide a relatively accurate signal profile in the clean upper troposphere, for normalization (calibration) of the entire profile. Measurement of the vertical structure of the Saharan and marine aerosol layers, and of their relative backscattering strengths (to within the transmission errors noted below) is possible on a single-shot basis. This also applies at night.

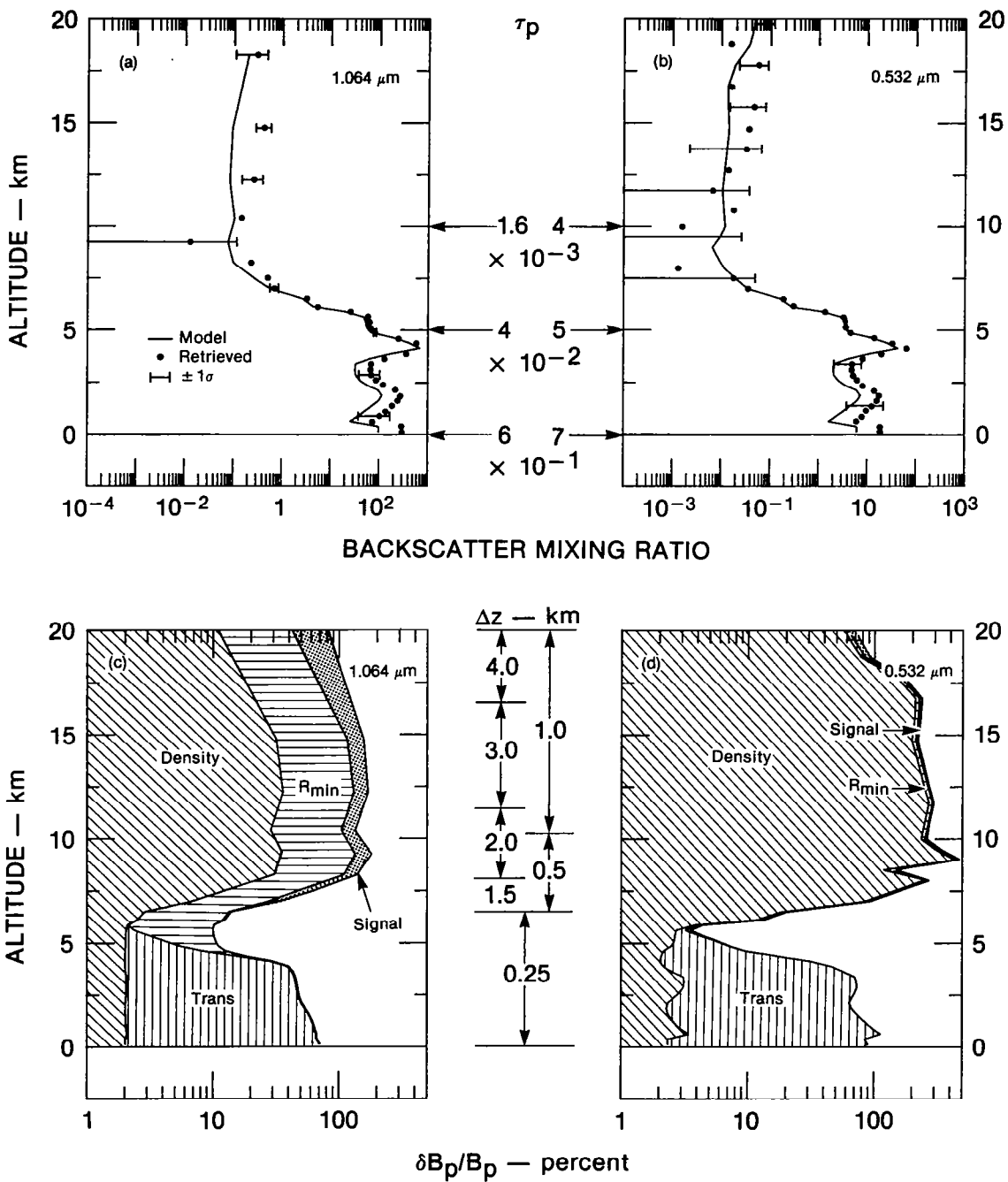


FIGURE 6 LOW-LATITUDE DAYTIME SIMULATION RESULTS, 1.064 AND 0.532 μm , USING CONVENTIONAL DENSITY DATA

(a,b) Backscatter mixing ratio profiles; (c,d) Relative uncertainty in particulate backscattering broken down by source.

Figure 6 shows that retrievals at both wavelengths are very good in the upper part of the Saharan layer, but that retrievals are degraded by transmission errors as penetration increases. However, because transmission errors change the shape of retrieved profiles in a gradual way, the presence and height of the lower Sahara layer at 2 km and the marine layer near the surface are well detected, even though backscatter strengths are not retrieved correctly. Thus, for example, an inference of marine aerosol layer depth should be possible in spite of transmission errors. This inference holds as long as extinction is not large enough to degrade signal measurement accuracy significantly.

A final point to notice in Figure 6 is that the error bars in Figure 6(a), in contrast to those in Figure 5(a), appear to underestimate systematically the 1σ difference between the retrieval (dots) and the model (solid line). Also, the retrieved profile is systematically offset to the right (i.e., too large), even above the height where transmission errors systematically distort the profile. The reason for the offset is a relatively large (~ 20 percent) negative error in the signal profile at 9.25 km, caused by drawing a random number that differed from the mean by about twice the distribution standard deviation, $\delta S^* = 0.10S^*$. The normalization procedure [Eq. (4)] then led to the systematic offset of the entire profile by an amount that exceeded the 1σ uncertainty $\delta S(z^*)$. This type of error will also occur occasionally in analyzing actual lidar data, and will then produce retrieved profiles that differ systematically from the true profile by more than the derived 1σ error bars. Note that the 1σ uncertainties given by Eqs. (11) and (12) describe the expected rms deviation of retrievals from actuality in an ensemble containing many profile measurements, rather than within one retrieved profile.

2. Midlatitude, Volcanic, Cirrus, Marine

a. Nighttime (Zenith Moonlit Cloud), $\Delta x \approx 200$ km

Figure 7 shows simulated retrievals for a midlatitude model atmosphere that includes a mesospheric aerosol layer at 46 to 54 km (see Appendix A). This simulation assumes density uncertainties of 3 percent below 40 km and 10 percent above. Even the relatively large density uncertainty of 10 percent is small compared to the mesospheric aerosol backscatter mixing ratio peak [~ 1.0 at $1.06 \mu\text{m}$; ~ 0.6 at $0.53 \mu\text{m}$; see also Figure 2(b)]. Thus, density uncertainties do not prevent a measurement of the mesospheric aerosol at either wavelength. However, signal errors do prevent a useful measurement above 45 km at $1.06 \mu\text{m}$; hence, the mesospheric layer is not detectable at this long wavelength. At $0.53 \mu\text{m}$, signal errors are considerably less, because of both increased backscatter coefficient and increased quantum efficiency. As can be seen in Figure 7(b,d), the peak of the mesospheric aerosol layer is unambiguously detected at this wavelength, with a measurement uncertainty of about 25 to 50 percent for the aerosol model used here (see Appendix A.3).

In the stratospheric aerosol layer (16 to 25 km) the moderate volcanic enhancement modeled here yields backscatter mixing ratios that are a factor of 3 to 6 larger than those of the background midlatitude stratospheric aerosol.^{16,18} As a result, the relative retrieval error caused by density errors is proportionately reduced. Both wavelengths give good retrievals in the stratospheric aerosol peak; however, the region of good retrieval extends farther from the peak at $1.06 \mu\text{m}$ because of the reduced effect of density errors at that wavelength.

Both wavelengths give good quantitative retrievals of the subvisible and visible cloud layers, and both detect the presence of the elevated and surface marine aerosol layers below the clouds. However, transmission errors degrade the quantitative retrievals below the lowest cloud.

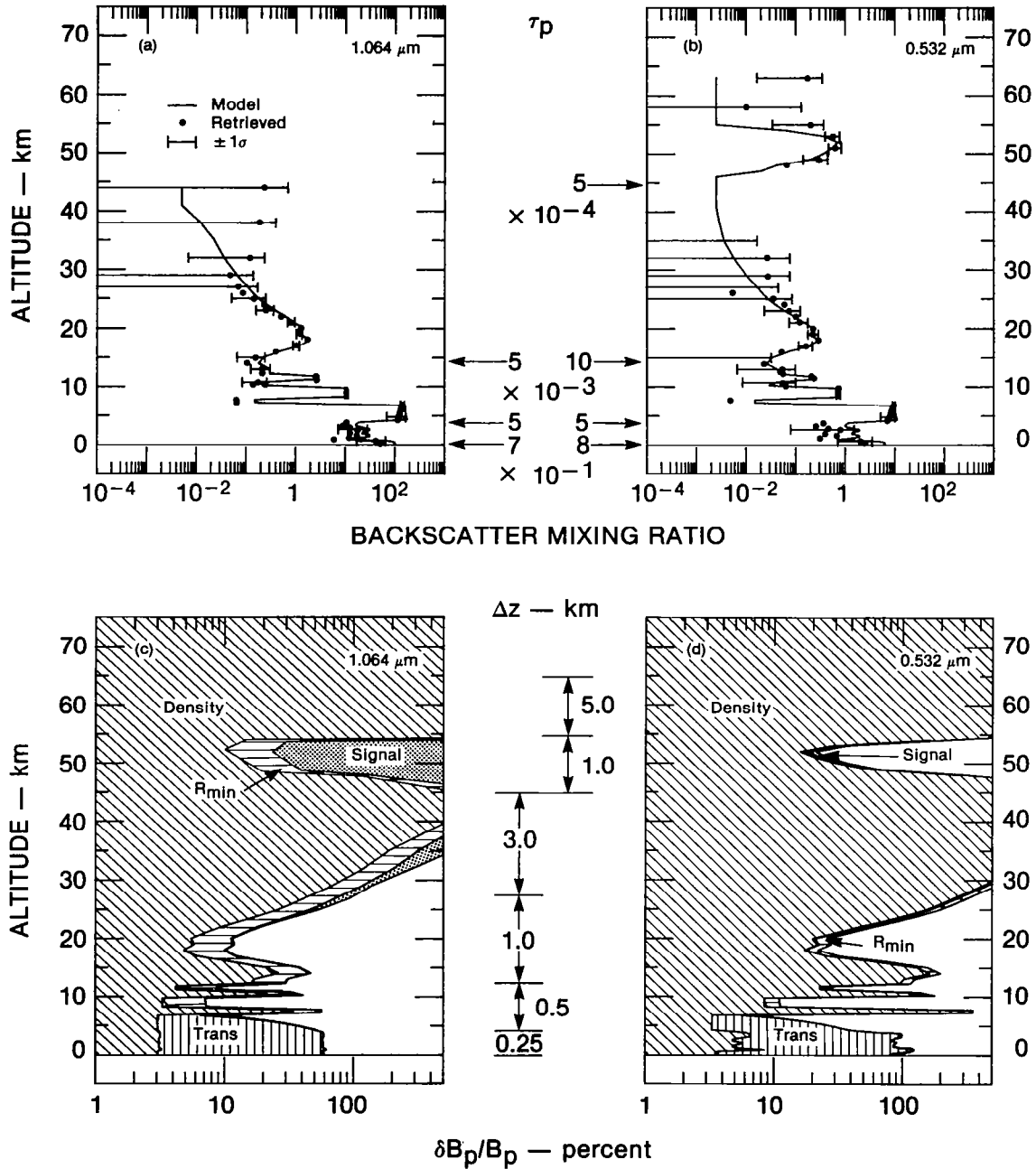


FIGURE 7 MID-LATITUDE NIGHTTIME SIMULATION RESULTS, 1.064 AND 0.532 μm , USING CONVENTIONAL DENSITY DATA

(a,b) Backscatter mixing ratio profiles; (c,d) Relative uncertainty in particulate backscattering broken down by source.

b. Daytime (Zenith Sunlit Cloud), $\Delta x \approx 100$ km

Figure 8 shows results for the same model atmosphere as Figures 7 and 2(b), but now for the daytime lidar configuration (Table 1) and a sunlit cloud background radiance. At both wavelengths, signal errors prevent useful measurements above 35 km, so the mesospheric aerosol layer is not detectable during the daytime. However, at $0.53 \mu\text{m}$, signal errors are small enough that the moderate volcanic stratospheric aerosol layer is barely detectable; notice, though, that use of noisy signals above 25 km for normalization leads to a normalization error that affects the uppermost cloud retrieval significantly. At $1.06 \mu\text{m}$, even the moderate-volcanic stratospheric aerosol layer is not detectable by day, and normalization is achieved below its height, above and between the clouds.

As with the nighttime case, both wavelengths give good quantitative retrievals for the backscattering coefficient at the top of each sub-visible or visible cloud layer, with the exception noted above caused by poor normalization. However, transmission errors in the lowest cloud significantly degrade quantitative retrievals below that cloud's top. As noted previously, these errors do not affect the heights inferred for the lowest aerosol layers, but they do prevent quantitative inferences of the amount of aerosol present. Notice that heights are retrieved with a vertical resolution of 0.25 km in this simulation; in fact signal-to-noise ratios permit even finer vertical resolution--see Section V-B-3-b.

Notice that the transmission errors in Figure 8(a,b) are opposite in sign to those in Figure 7(a,b). This simulates the use by the analyst of two different erroneous transmission profiles in the two different scenarios: overestimating the transmission in Figure 7(a,b), and underestimating it in Figure 8(a,b).

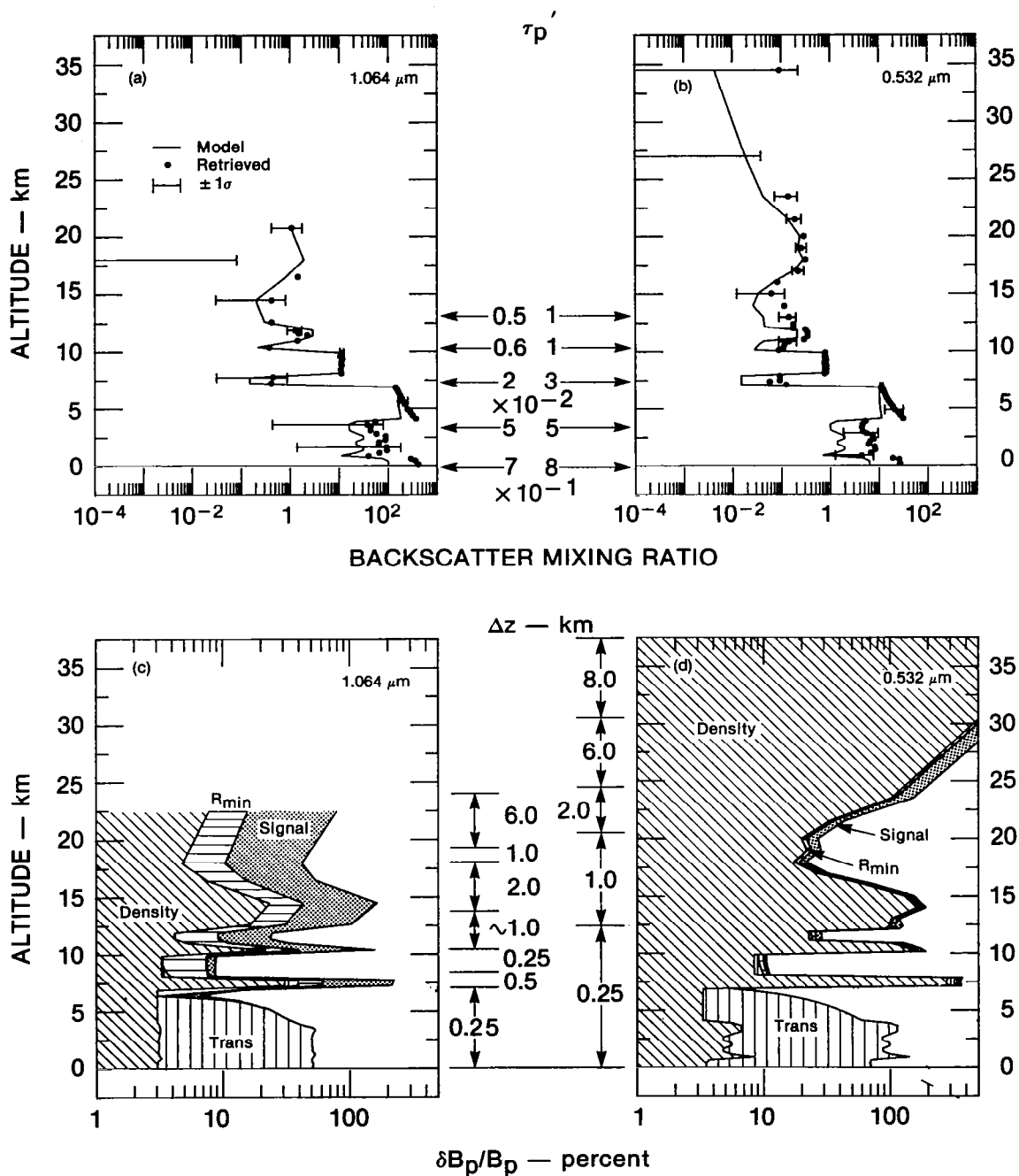


FIGURE 8 MID-LATITUDE DAYTIME SIMULATION RESULTS, 1.064 AND 0.532 μm , USING CONVENTIONAL DENSITY DATA

(a,b) Backscatter mixing ratio profiles; (c,d) Relative uncertainty in particulate backscattering broken down by source.

3. High-Latitude, Nonvolcanic, Noctilucent Cloud, Marine

a. Nighttime (Moonlit Cloud, $\cos \theta_0 = 0.5$), $\Delta x \approx 2000$ km

Figure 9 shows results for a high-latitude model atmosphere [Figure 2(c)] that includes both a noctilucent cloud (at 80 km) and an enhanced mesospheric aerosol layer (63 to 73 km) of the type that accompanied noctilucent clouds (NLCs) in the measurements of Fiocco and Grams.^{28,29} This simulation assumes density uncertainties of 3 percent below 40 km and 10 percent above. As in the previous case, density errors are not critical for measurements of the mesospheric layers, but signal errors are, especially at 1.06 μm . To see whether increased measurement time might significantly aid the 1.06- μm measurement, this scenario assumes integration for 280 s (2800 shots, $\Delta x \approx 2000$ km). At the high-latitude extreme of an orbit with inclinations 70 to 80°, such a distance on the suborbital path would cover only $\sim 5^\circ$ of latitude and 40° of longitude; thus, the mesospheric aerosol layer (though probably not the NLC) may be uniform enough in this integration distance to provide a meaningful average.

Figure 9(a) shows that even with such a long integration period 1.06- μm signal errors are too large to permit a useful retrieval of the mesospheric aerosol layer. However, because the 1.06- μm signal from the noctilucent cloud is comparable to that from the stratospheric aerosol [see Figure 3(c)], the NLC is readily detected. Figure 9(b) shows a simulated retrieval at 0.53 μm for the same integration period. The retrieval of both the mesospheric aerosol and the NLC is quite good, and Figure 9(d) shows that, for this wavelength and integration time, signal errors are a minor source of uncertainty. In fact, a similar retrieval could be obtained with an integration time of 70 s (700 shots, $\Delta z \approx 500$ km). At the 0.53 μm wavelength, the NLC layer can be detected with a single shot. [See Figure 3(c)]. Hence, the layer's height could be monitored on a very fine horizontal scale, for example to trace out wave motions. (At 10 Hz and 7 km s⁻¹, the suborbital shot-to-shot distance is 700 m.)

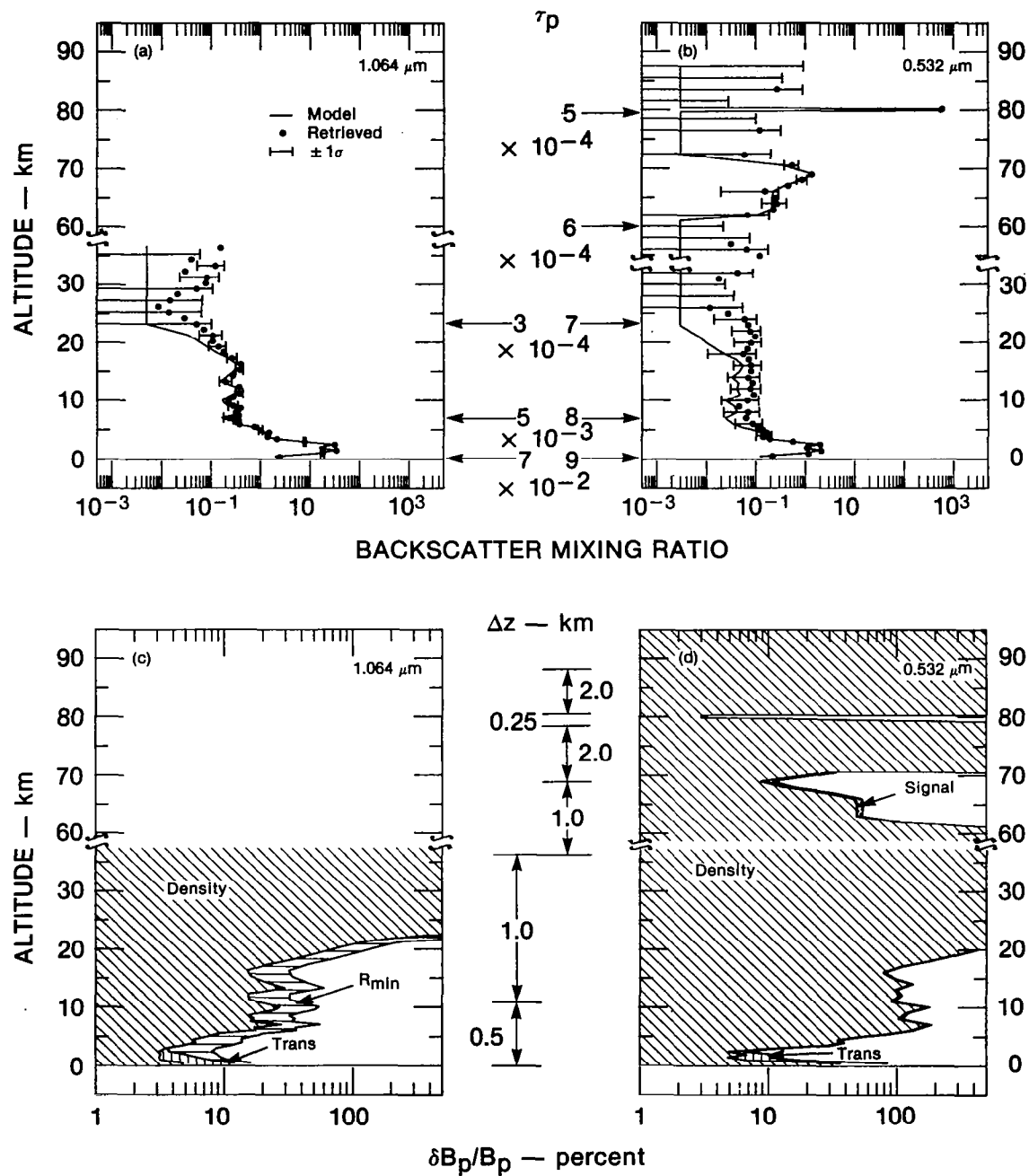


FIGURE 9 HIGH-LATITUDE NIGHTTIME SIMULATION RESULTS, 1.064 AND 0.532 μm , USING CONVENTIONAL DENSITY DATA

(a,b) Backscatter mixing ratio profiles; (c,d) Relative uncertainty in particulate backscattering broken down by source.

In the stratosphere, the high-latitude nonvolcanic aerosol layer is lower (~12 to 18 km) than at other latitudes (cf. Figure 2), and the increased gas backscattering B_g at the lower heights yields smaller backscatter mixing ratios B_p/B_g for a given particulate backscattering B_p . At $0.53 \mu\text{m}$, the model stratospheric aerosol backscatter mixing ratios (0.03 to 0.05) are comparable to the assumed 1σ uncertainty in molecular density (0.03). Hence, detection of the layer is barely possible, and measurement errors make it impossible to retrieve the layer's vertical structure. At $1.06 \mu\text{m}$, the considerably larger backscatter mixing ratios (0.2 to 0.3) greatly reduce the effect of density errors, permitting a good retrieval of layer vertical structure. Uncertainty in R_{\min} increases the uncertainty of absolute backscatter retrievals to 30 to 60 percent [Figure 9(c)], but this uncertainty does not affect retrieved vertical structure.

Both wavelengths give good quantitative retrievals of the elevated marine aerosol layers (1 to 3 km). In fact, as the next scenario shows, considerably finer vertical resolution is possible, permitting a retrieval of the surface-based marine aerosol layer's height.

- b. Daytime (Sunlit Cloud or Ice, $\cos \theta_0 = 0.5$)
 $\Delta x \approx 100 \text{ km}$

Figure 10 shows results for the same model atmosphere as Figures 9 and 2(c), but with the daytime lidar configuration (Table 1) and a background approximating a sunlit cloud (Table 2). At both wavelengths the nonvolcanic stratospheric aerosol is retrieved very poorly (if at all); however, the marine aerosol layers are retrieved very well with a vertical resolution of 0.1 km.

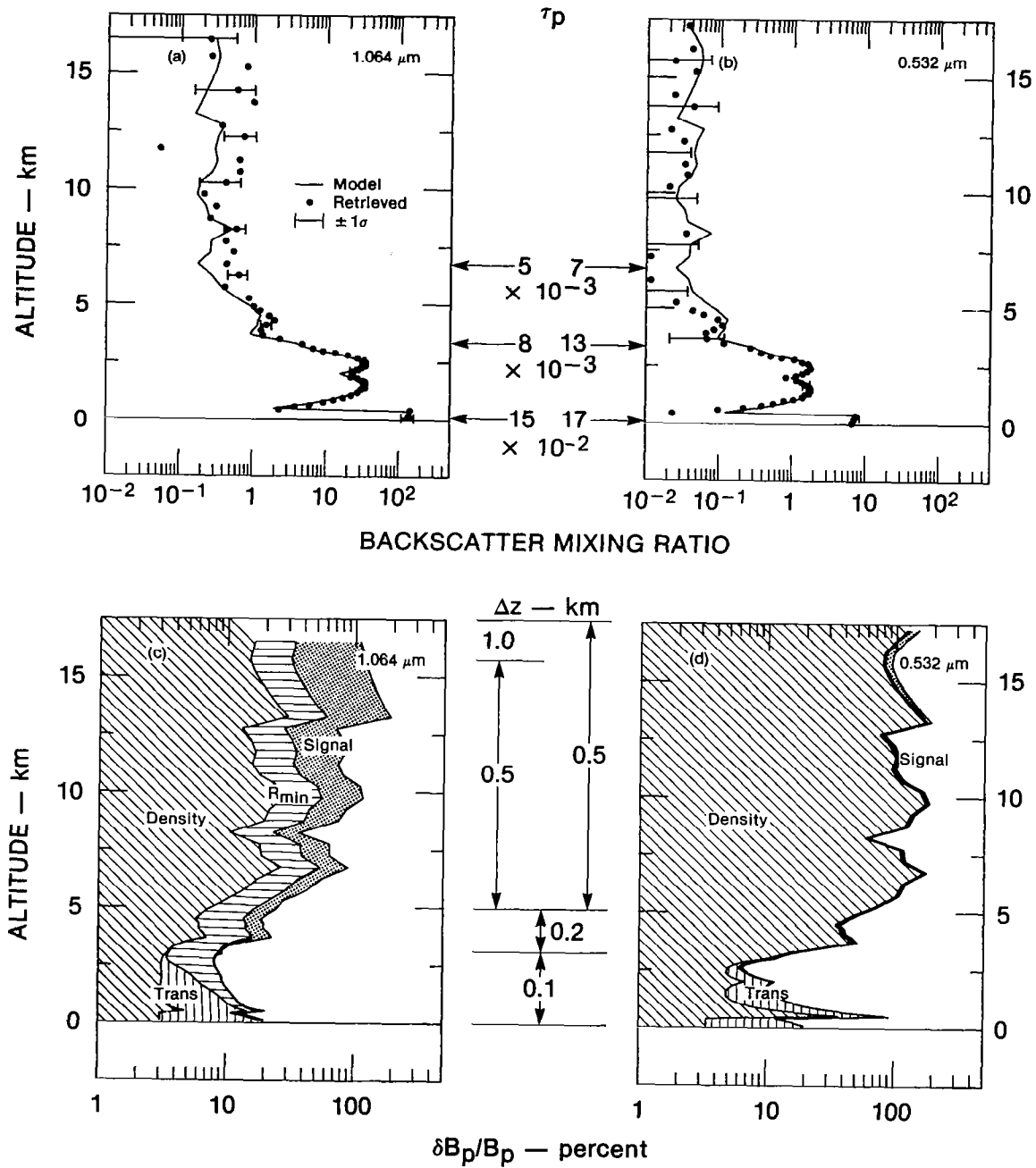


FIGURE 10 HIGH-LATITUDE DAYTIME SIMULATION RESULTS, 1.064 AND 0.532 μm , USING CONVENTIONAL DENSITY DATA

(a,b) Backscatter mixing ratio profiles; (c,d) Relative uncertainty in particulate backscattering broken down by source.

VI SUMMARY AND CONCLUSIONS

We have evaluated the expected accuracy of retrieved particle backscatter information for a proposed shuttleborne lidar operating over three model atmospheres, each with nighttime and daytime background lighting. The model atmospheres, representing low, middle, and high latitudes, include profiles of total gas density, ozone, tenuous clouds (subvisible and visible), and mesospheric, stratospheric, and tropospheric (Saharan and marine) aerosols. Each model is based on previous optical and physical measurements, so as to represent conditions likely to occur in practice. The background lighting conditions simulate radiances from sunlit clouds, a sunlit ocean, and moonlit clouds.

The data profile from each lidar wavelength was assumed to be analyzed independently of data from other wavelengths, using the scattering ratio/normalization method of analysis. A further assumption was that only conventional total gas density profiles were available, and that these had rms errors ranging from 2 to 3 percent below 30 km to 5 to 10 percent above 40 km in data-sparse regions of the globe, where most shuttle lidar measurements will be made. For each scenario, expected errors in retrieved particle backscatter were calculated from algebraic expressions and also checked by numerical simulations using random number generators. Both the algebraic expressions and the simulations include all four sources of error that we have encountered in actual lidar measurements and analyses: namely, errors in (1) measuring the backscattered signal, (2) accounting for transmission losses, (3) determining the total gas density profile at the lidar location, and (4) calibrating signals in terms of backscatter using an atmospheric layer where gas backscatter dominates particle backscatter.

The results show that useful retrievals can be made for the following constituents and conditions:

- By day: Vertical structure of tenuous clouds (subvisible and visible), Saharan aerosols, and boundary-layer aerosols (at both 0.53- and 1.06- μm wavelengths), and strong volcanic stratospheric aerosols (at 0.53 μm). Quantitative backscatter can be determined for all of the preceding, provided particulate optical depth does not exceed ~ 0.3 .
- By night: Vertical structure and quantitative backscatter for all of the above, plus upper tropospheric and stratospheric aerosols (at 1.06 μm) and mesospheric aerosols and noctilucent clouds (at 0.53 μm). (Again, quantitative backscatter retrievals suffer when particulate optical depth exceeds ~ 0.3 .)

These results were obtained with vertical resolutions of 0.1 to 0.5 km in the troposphere and 0.5 to 2.0 km in the stratosphere and above, except within the mesospheric aerosol and noctilucent cloud layers, where resolutions of 1.0 and 0.25 km, respectively, were used. Horizontal resolution was 100 km in the troposphere, 200 km in the stratosphere and lower mesosphere (below ~ 60 km), and 2000 km in the upper mesosphere (to ~ 85 km). Vertical structure of the stronger layers (noctilucent and cirrus clouds, lower tropospheric aerosols) could be observed on much finer horizontal scales (sometimes on single shots--about 700 m apart); moreover, these fine-scale results could be converted to quantitative backscatter if a transmit energy monitor or stable transmit energy were provided.

In general, the principal virtue of the 1.06- μm wavelength is its reduced sensitivity to gas density errors, which are the dominant error source for upper tropospheric and nonvolcanic stratospheric aerosols. Also, 1.06- μm retrievals are somewhat less susceptible to transmission errors in the stronger layers. The principal virtue of the 0.53- μm wavelength is the stronger signal available (because of both atmospheric backscatter and quantum efficiency). These stronger signals are essential for observing the mesospheric aerosol layers at useful horizontal and vertical resolutions.

At both 0.53 and 1.06 μm , errors in the gas density profile are the dominant source of uncertainty in measuring nonvolcanic stratospheric and upper tropospheric aerosols. Although useful retrievals of these aerosols can be made at 1.06 μm by using conventional density information, retrievals at both wavelengths would be improved by better density information. Part Two⁶ describes a method for obtaining such information from the lidar itself.

Appendix A

ATMOSPHERIC MODELS

A. Molecular Density

At heights above about 30 km, our model molecular densities are equal to the corresponding seasonal and latitudinal models in the U.S. Standard Atmosphere Supplements, 1966.³⁰ Below about 30 km, our model molecular densities are computed from temperature and pressure measurements made on each balloon flight described in Section D of this appendix. These balloon-measured densities differ by less than 10 percent from the corresponding seasonal and latitudinal models of the U.S. Standard Atmosphere Supplements, 1966.³⁰

An exception to this rule is the high-latitude case, in which the 30- to 90-km model is for July, 60°N, whereas the balloon flight was made in November, at 72°N. In this case we replaced the balloon densities with the 60°N July model densities at all heights to avoid a mismatch in the density profile.

B. Ozone

Our model ozone concentration profiles are taken from the seasonal and latitudinal plots assembled in the review by Wu.³¹

C. Noctilucent Cloud and Mesospheric Aerosol

The mesospheric aerosol model is based on lidar observations made at the ruby-laser wavelength 0.694 μm by Fiocco and Grams^{28,29} who observed vertical distributions of mesospheric aerosols at high latitudes when noctilucent cloud (NLC) displays were expected. These measurements indicated that, at high latitudes, the altitude region from 60

to 70 km contains significant particulate material during the summer, and that the amount of this material appears to be slightly enhanced (by a factor of ~2) during periods of NLC activity. The experiments also provided information on the optical thickness and vertical structure of an NLC.

The first series of experiments²⁸ were carried out with a lidar system installed near Fairbanks and a mobile lidar system operated at several locations in Sweden during the summer of 1964. These experiments gave evidence for a scattering layer between 68 and 72 km on two consecutive nights for which NLC were observed on the horizon at each location. The average particulate optical thickness of the layer during that time was estimated to be $(1 \pm 0.2) \times 10^{-6}$. During the summer of 1964, NLC activity was moderate, and displays were never observed overhead when the lidar was in operation.

The second series of lidar NLC experiments²⁹ was conducted near Oslo from early July to mid-August 1966. These experiments provided further evidence for a broad region of enhanced backscattering throughout the summer in the 60- to 70-km interval with a well-defined maximum in the region from 66 to 68 km. The echoes from that layer were strongest on nights during which NLC were present--as would be expected from the 1964 results. The average particulate optical thickness for the 2-km interval from 66 to 68 km was $(7 \pm 1) \times 10^{-6}$ for all nights when NLC were visually observed; this is more scattering by a factor of about 3 than would be expected from that interval for molecular density profiles specified by the U.S. Standard Atmospheric Supplements, 1966³⁰ in the July standard atmosphere for 60°N. For nights without NLC displays, the average particulate optical thickness for that same altitude interval was estimated to be about 3×10^{-6} --about one-half the value observed during NLC activity. The above results document the existence below the NLC region of a layer of particles that is normally located near the mesopause at about 80 km. Fiocco and Grams³² discuss possible mechanisms for formation of a 70-km layer, while Grams and Fiocco³³ discuss the conditions necessary for formation of NLC layers at

the mesopause. The experimental results described above are based on an analysis of data obtained by summing the number of photoelectrons received in 2-km altitude intervals between 40 and 100 km. For the single case during the summer of 1966 when the lidar was operating with an overhead NLC display, oscilloscope photographs for each individual laser pulse were analyzed to provide data for a detailed study of the transient features of the NLC. Range resolution was about 100 m. Those results indicated that an NLC detected by the lidar at about 75 km was no more than 0.5 km thick. The optical thickness of the layer was estimated to be 10^{-4} during the short time the NLC was directly over the lidar system.

We used the data in Figure 1 of Ref. 29 to derive scattering ratio profiles referenced to the atmospheric density profile specified in the 60°N July model of the U.S. Standard Atmosphere Supplements, 1966.³⁰ Our "typical" high-latitude mesospheric aerosol profile, for nights without NLC displays, is shown in Figure A-1. Our model for nights with NLC is shown in Figure A-2. In both figures, the "backscattering coefficient" is the radar cross section, per unit volume and 4π sr, of the aerosol (solid line) and the air molecules (dashed line) at the wavelength 0.6943 μm .

Our choice of a size distribution for the 60- to 70-km layer was also guided by results presented in the same publication. Shettle and Fenn³⁴ proposed a very broad log-normal distribution function for extraterrestrial meteoric debris with geometric mean radius $r_g = 0.03 \mu\text{m}$ and geometric standard deviation of $\sigma_g = 3$. If we assume the particle density is $\sim 2 \text{ g cm}^{-3}$, the results of Ref. 29 suggest that the meridional circulation pattern has three effects: to remove all particles with radius less than $\sim 0.02 \mu\text{m}$; to enhance significantly the concentration of particles with radius between 0.02 and 0.1 μm ; and to cause only minor changes at larger particle radii. We therefore chose a narrower distribution function with $r_g = 0.04 \mu\text{m}$ and $\sigma_g = 1.5$ for both the "typical" and the "high-concentration" cases. For the refractive index, we used results for the "synthetic aerosol" model published by Ivlev and

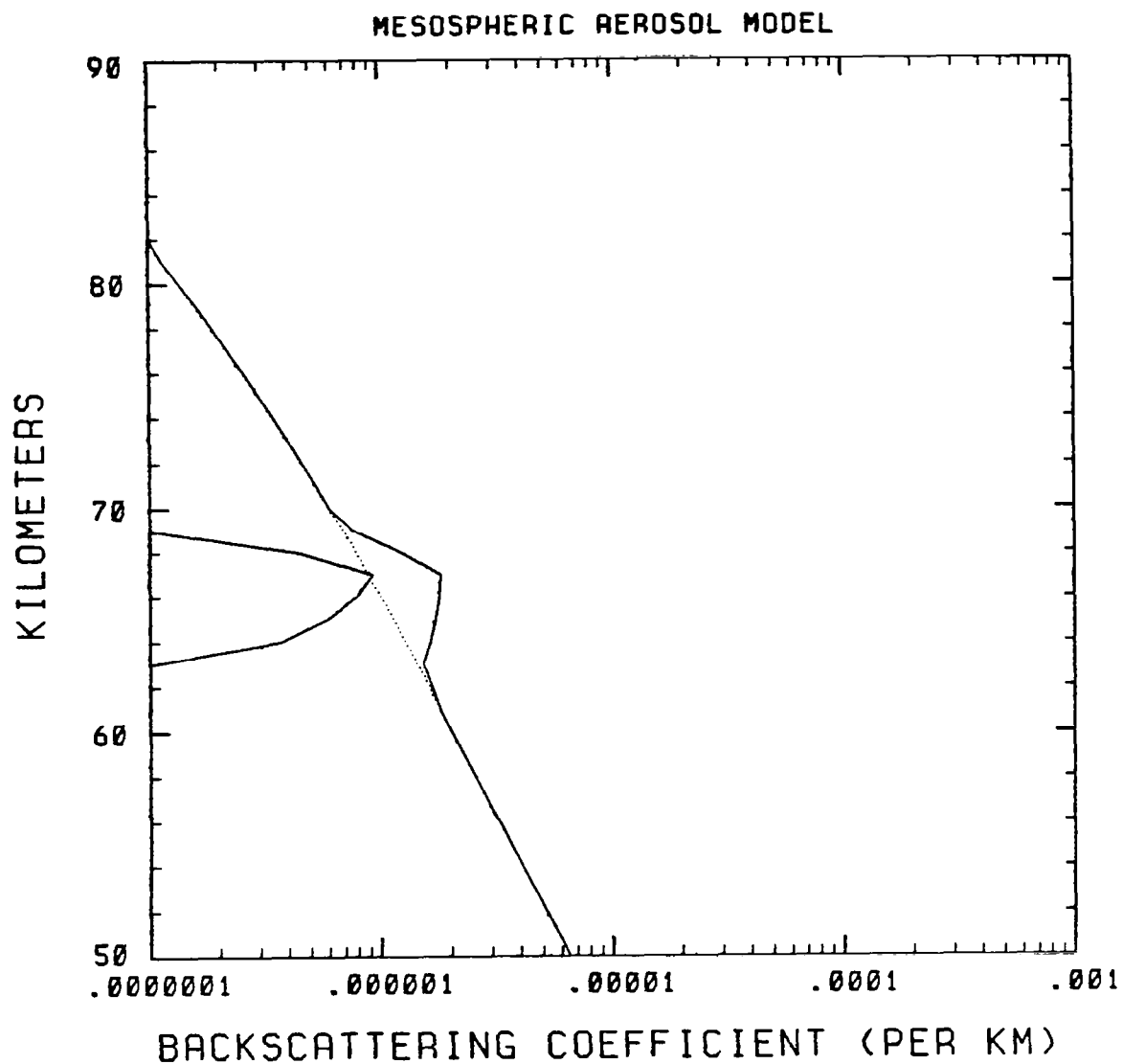


FIGURE A-1 BACKSCATTERING COEFFICIENTS (PER 4π sr) AT THE WAVELENGTH $\lambda = 0.694 \mu\text{m}$ FOR THE "TYPICAL" MESOSPHERIC AEROSOL MODEL (CURVE WITH SOLID LINE ON THE LEFT SIDE) ALONG WITH COEFFICIENTS FOR MOLECULAR SCATTERING (DASHED LINE) AND TOTAL SCATTERING (SOLID LINE)

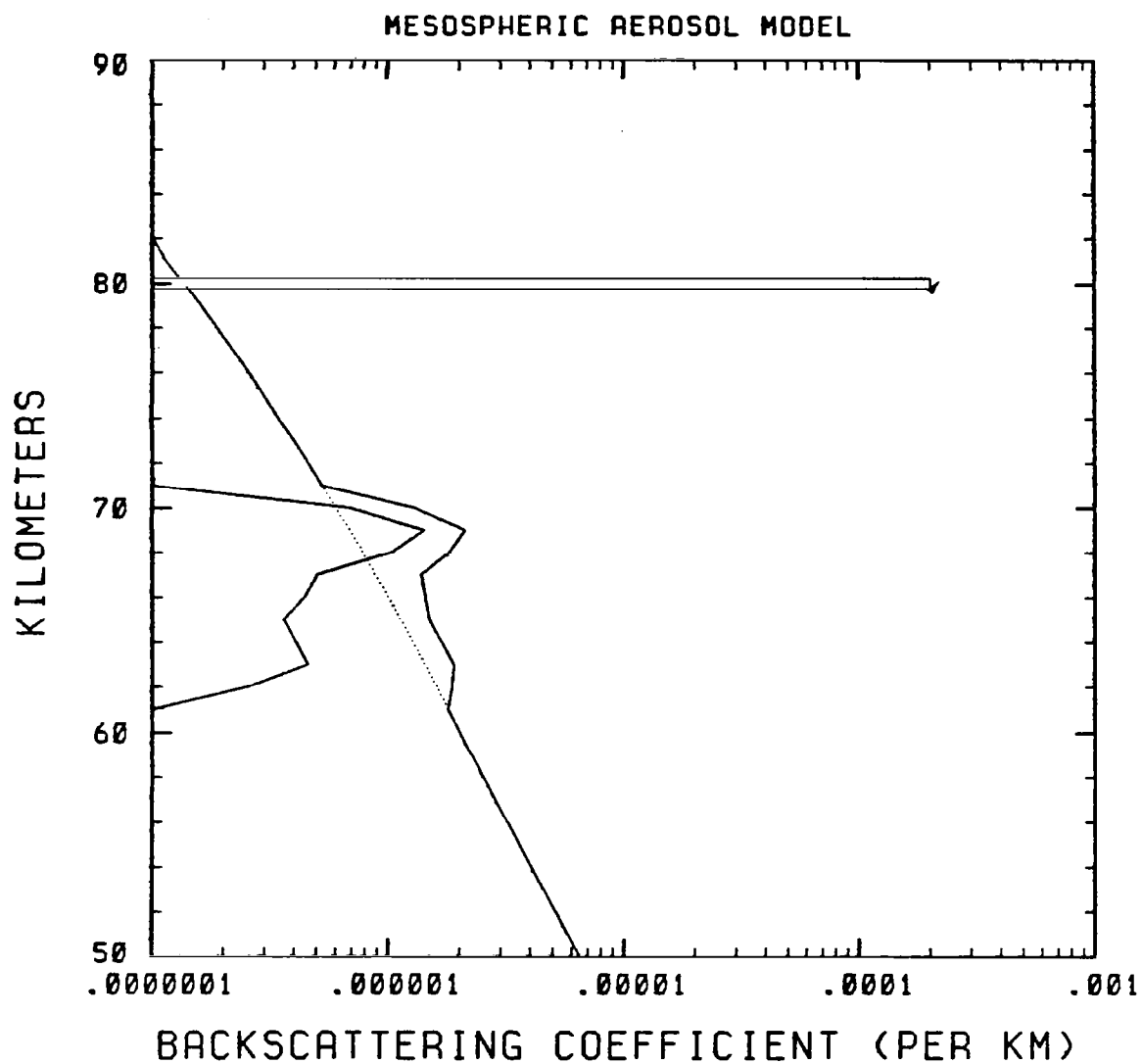


FIGURE A-2 SAME AS FIGURE A-1 EXCEPT FOR THE NLC OR HIGH CONCENTRATION MESOSPHERIC AEROSOL MODEL

Popova,³⁵ which was also used by Fiocco et al.³⁶ to specify optical properties of high altitude aerosols in a study of the energetic equilibrium of small particles in the upper atmosphere.

For the NLC case, we added a 0.5-km-thick layer of particles centered at 80-km altitude to the high-concentration 70-km layer. The lidar backscattering cross section of the NLC was taken to be $1.6 \times 10^{-5} \text{ km}^{-1} \text{ sr}^{-1}$ at $\lambda = 0.6943 \text{ }\mu\text{m}$ in accordance with the lidar NLC observations of Ref. 29. For the refractive index of NLC particles, we chose to use a real refractive index of $m = 1.33$ for our calculations--as did Grams and Fiocco³⁶ for visible wavelength calculations in their study of the equilibrium temperatures of NLC particles. The NLC particles are assumed to be somewhat larger than the extraterrestrial particles in the 60- to 70-km layer with a larger, more sharply peaked size distribution, which is consistent with the expectations for particle formation. We used $r_g = 0.1 \text{ }\mu\text{m}$ and $\sigma_g = 1.3$ for the NLC particles; the peak in the particle area distribution function for those log-normal parameters is very close to the often- $0.13 \text{ }\mu\text{m}$ value quoted for NLC particles.³⁷⁻⁴⁰

We also used our high-latitude mesospheric aerosol model to specify optical parameters for a midlatitude mesospheric layer. The intent here is to simulate particle layers near the 50-km level that have been occasionally observed by investigators using techniques other than lidar. We believe, in accordance with the mechanisms discussed in Ref. 32, that the midlatitude, 50-km layer may be a southward extension of the same scattering layer that Fiocco and Grams observed in the 60- to 70-km region at higher latitudes. In this case we would expect the layer to be located at a somewhat lower altitude (e.g., 50 km) at midlatitude locations and, furthermore, we would expect that the mixing ratio of the particles in the layer would be approximately the same as had been observed for the high-latitude layer. We therefore specify our midlatitude mesospheric aerosol model by assuming that our high-latitude mesospheric layer was transported downward from the 60- to 70-km level and centered at the 50-km level. We furthermore assumed that this layer has

the same mixing ratio that it had in the higher altitude and latitude, i.e., that the aerosol concentration is increased in the same proportion as the increase in molecular density between the two altitudes. The proposed mechanism applies only to summertime conditions, and the molecular density profile for our midlatitude mesospheric aerosol model is taken from the 45°N July atmospheric model described in Ref. 30. As noctilucent clouds are not observed in midlatitudes, the midlatitude mesospheric model does not include an NLC layer for the high-concentration case.

The optical parameters used in the mesospheric aerosol model are summarized in Table A-1.

D. Stratospheric and Upper Tropospheric Aerosol

Each upper tropospheric/stratospheric aerosol model was derived from a two-channel vertical profile of particle number measured by a dustsonde (optical particle counter) flown by the University of Wyoming.⁴¹⁻⁴³ The locations and dates of the dustsonde measurements are:

- Nonvolcanic low-latitude model: Panama (9°N), November 1973
- Nonvolcanic mid-latitude model: Wyoming (41°N), September 1978
- Nonvolcanic high-latitude model: Greenland (64°N), November 1978
- Volcanic mid-latitude model: Missouri (41°N), July 1975.

The dustsonde data are shown in Figure A-3. Each dustsonde flight yields vertical profiles of $N_{0.15}$ and $N_{0.25}$, where N_r is the number of particles with radius greater than r microns. These particle number profiles were converted to backscattering profiles at five wavelengths by using the optical modeling procedure described in detail by Russell et al.⁴⁴ This procedure divides the stratosphere and upper troposphere into layers, each having a range of refractive indices and relative size distributions. Table A-2 summarizes the three main layers (or subsets); between each layer is a transition layer in which optical properties are interpolated to yield a smooth transition. All allowed size distribution types and refractive indices are based on previously published

Table A-1

OPTICAL PARAMETERS FOR MESOSPHERIC AEROSOL MODEL:
 LOG-NORMAL DISTRIBUTION FUNCTIONS $dn/d \log r$ WITH INDICATED VALUES OF
 GEOMETRIC MEAN RADIUS r_g AND GEOMETRIC STANDARD DEVIATION σ_g
 AND INDICATED VALUES OF COMPLEX REFRACTIVE INDEX
 $m = (n_{RE}, n_{IM})$.
 All profiles use N_p values that are consistent with
 observed B_p values at $0.6943 \mu m$

Model	r_g (μm)	σ_g	(cm^{-3})	n_{RE}	n_{IM}	λ (μm)	B_p ($10^{-12}/km/sr$)	E_p ($10^{-11}/km$)	B_p/E_p (sr^{-1})
NLC	0.1	1.3	1.0	1.33	0	0.266	5.16	5.22	0.0099
						0.355	3.06	2.85	0.0107
						0.532	2.29	0.999	0.0229
						0.694	2.20	0.458	0.0480
						1.064	0.912	0.107	0.0849
Mesospheric layer	0.04	1.5	1.0	1.65	-0.005	0.266	1.48	0.862	0.0172
						0.355	1.12	0.411	0.0273
						0.532	0.637	0.109	0.0583
						0.694	0.323	0.0426	0.0759
						1.064	0.0727	0.00934	0.0779

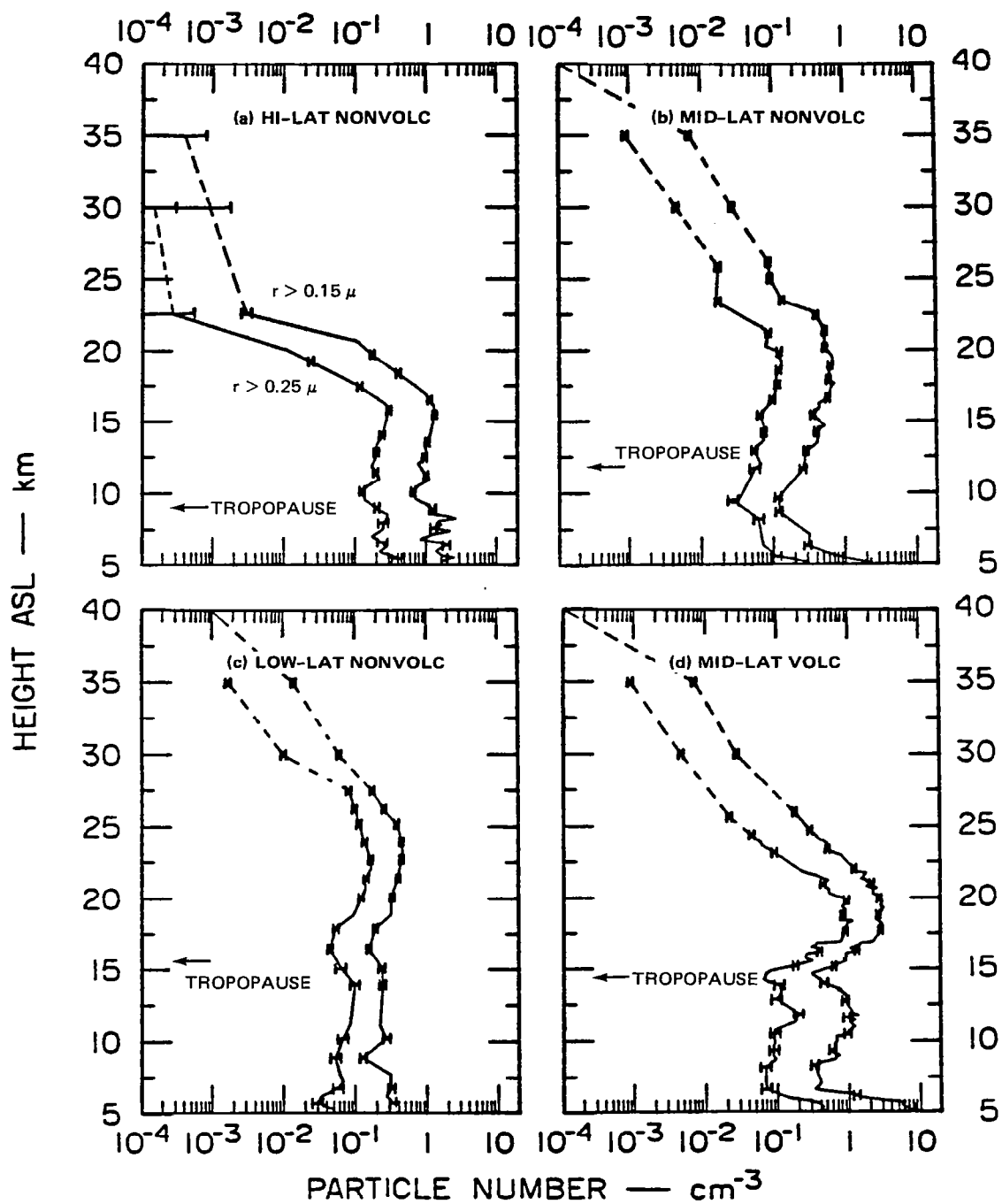


FIGURE A-3 DUSTSONDE DATA USED TO DERIVE STRATOSPHERIC AEROSOL BACKSCATTER MODELS

Dashed lines are extrapolations. Arrows mark tropopause height. See text for measurement sites and dates.

Table A-2

STRATOSPHERIC AND UPPER TROPOSPHERIC AEROSOL
MODEL SIZE DISTRIBUTIONS AND REFRACTIVE INDICES

Subset Name	Height Range*	Relative Size Distribution Types	Refractive Indices
Inner stratospheric	T + 4 km to 30 km	1 log-normal, 1 exponential, 1 truncated power law, 3 zold, 3 modified gamma (each adjusted to match dustsonde measurement)	1.40-0i, 1.42-0i 1.43-0i, 1.52-0i
Tropopause layer	0.7T to T + 2 km	3 segmented power law fits to 10-16 km data of Bigg ^{45,46} [41 flights] and Gras and Michael ⁴⁷ [3 flights]	1.40-0i, 1.42-0i 1.43-0i, 1.52-0i
Upper troposphere	0.3T to 0.6T	Segmented power law (Toon and Pollack ⁴⁸)	1.33-0i, 1.52-0i, 1.525-0.005i

* T is tropopause height. For details see Russell et al.⁴⁴

measurements and inferences. Detailed references to the original publications, as well as the rationale for layer height boundaries, are given in Ref. 44.

As noted in Table A-2, within the "inner stratospheric" layer, size distributions are adjusted at each height to agree with the dustsonde data ($N_{0.15}$ and $N_{0.25}$) from the measurement being analyzed. This procedure makes use of the limited information on particle size distribution available from the dustsonde measurement, while estimating unmeasured size distribution details from the models. Because the dustsonde measurements do not totally constrain the models, a range of models is allowed for each measurement height. Mie-scattering calculations were made to transform this allowed range of models to a corresponding range (or set) of ratios relating backscatter to particle number (specifically, $N_{0.15}$). The mean of this set of backscatter-to-number ratios is taken as the most probable ratio, and the standard deviation is taken as its 1 σ uncertainty. (The uncertainties were not explicitly used in this project.)

The above process was performed on the dustsonde data of Figure A-3 for each of the wavelengths (1.064, 0.694, 0.532, 0.355, 0.266 μm) used in this study. Figure A-4 shows the resulting multiwavelength backscatter profiles. The upper stratosphere--above 40 km--is not included because of the lack of aerosol measurements there. Between 40 km and the top of the dustsonde data (22 to 30 km, depending on the particular measurement), the data have been extrapolated.

As a test of the optical modeling procedure, we have compared the derived backscatter profiles at wavelength 0.694 μm with ruby lidar measurements made at the time and place of the dustsonde measurements (except for the Panama measurement, for which no lidar measurements were made). In each case, the measured and modeled scattering ratio profiles agreed to within the combined measurement and conversion uncertainties (roughly speaking, an uncertainty of 0.03 in scattering ratio).

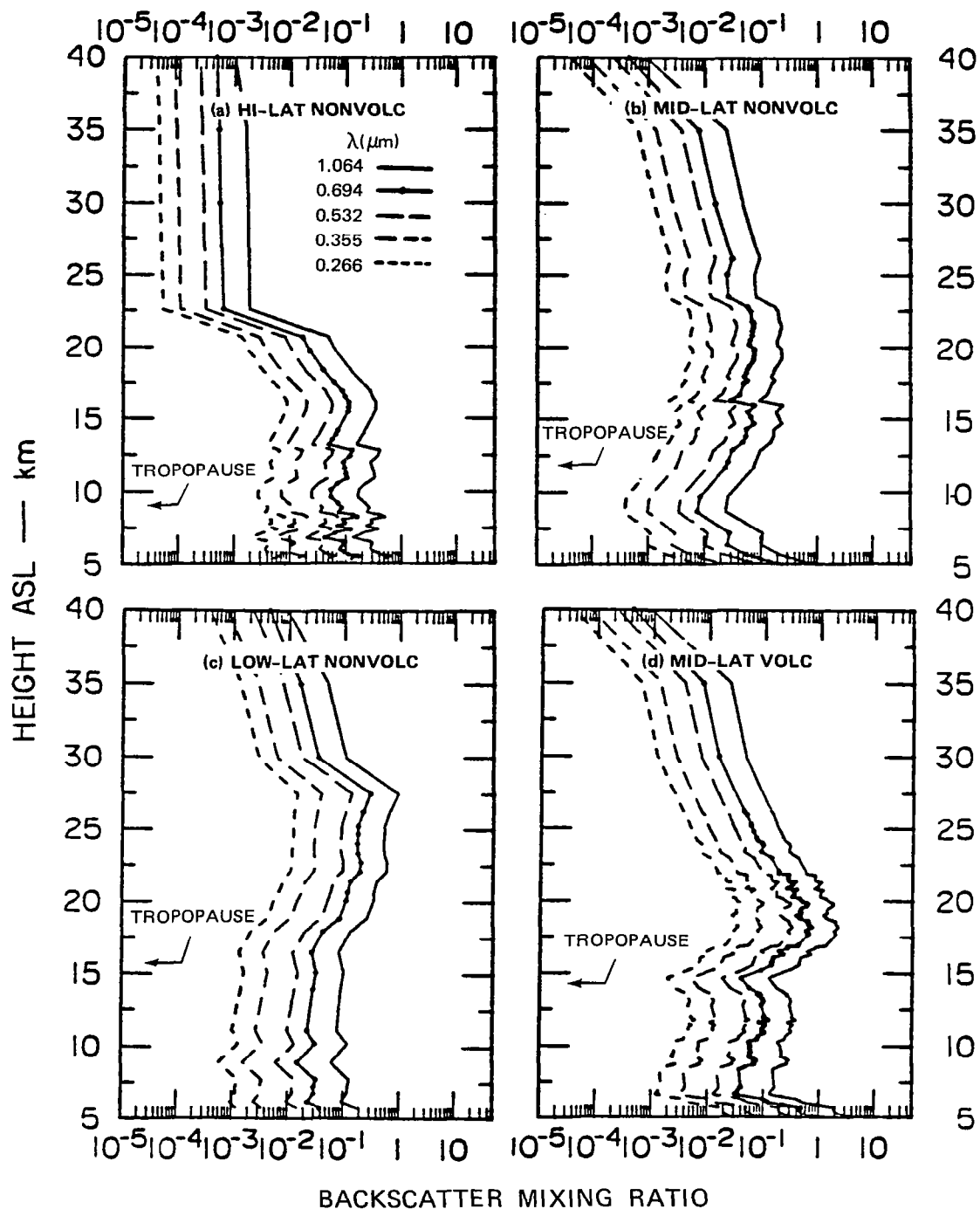


FIGURE A-4 MODEL BACKSCATTER MIXING RATIO PROFILES DERIVED FROM THE DUSTSONDE DATA OF FIGURE A-3 AND THE OPTICAL MODEL OF TABLE A-2

Although this comparison does not prove the validity of the backscattering profiles derived at other wavelengths, it lends confidence in the modeling procedure and is the best test than can be made on the basis of currently available data.

E. Saharan Aerosol

The Saharan aerosol layer consists of crustal aerosol particles that are generated in the deserts of northwest Africa and transported across the tropical Atlantic ocean north of the equator. The Saharan aerosol layer is generally confined between the tradewind inversion at ~1 km and an altitude of 4 to 6 km, with a well-defined top. The transport is most important during summer.

The Saharan aerosol model is based on a series of measurements of the refractive indices, size distribution, concentrations, and vertical profiles of the Saharan aerosol layer that have been made in the eastern Atlantic (Sal Island and the GATE study area) and in the western Atlantic (Barbados and the BOMEX study area). From these data, we consider three cases of aerosol concentration: high, typical, and low. The molecular density profiles are assumed to be given by the 15⁰ annual model of the atmosphere.³⁰

The size distributions in each case have been chosen to be single modal log-normal distributions of the form

$$\frac{dN}{d \log r} = \frac{N_p}{\sqrt{2\pi} \log \sigma_g} \exp \left[-\frac{(\log r - \log r_g)^2}{2 \log^2 \sigma_g} \right], \quad (\text{A-1})$$

with N , r_g , and σ_g being, respectively, the number (per cm³), the geometric mean radius (μm), and the geometric standard deviation. The parameters of the distributions are shown in Table A-3. The size distribution for the typical concentration was chosen on the basis of various continental measurements reported by Patterson and Gillette⁴⁹ as well as the series of measurements during GATE reported by Savoie and

Table A-3

SAHARAN AEROSOL MODEL

	r_g (μm)	σ_g	N_p^* (cm^{-3})	λ (μm)	n_R	n_{IM}	σ_e (km^{-1})	σ_a (km^{-1})	β ($\text{km}^{-1}\text{sr}^{-1}$)	β/σ_e
Low concentration	0.30	2.00	1.00	1.064	1.530	-0.004	0.201E-02	0.193E-02	0.114E-03	0.567E-01
				0.694	1.550	-0.004	0.195E-02	0.183E-02	0.171E-03	0.879E-01
				0.532	1.560	-0.006	0.185E-02	0.164E-02	0.169E-03	0.916E-01
				0.500	1.560	-0.008	0.181E-02	0.156E-02	0.148E-03	0.816E-01
				0.355	1.580	-0.022	0.168E-02	0.113E-02	0.651E-04	0.388E-01
				0.266	1.600	-0.048	0.161E-02	0.888E-03	0.152E-04	0.942E-02
Typical concentration	0.35	2.20	1.00	1.064	1.530	-0.004	0.347E-02	0.326E-02	0.235E-03	0.678E-01
				0.694	1.550	-0.004	0.325E-02	0.296E-02	0.278E-03	0.858E-01
				0.532	1.560	-0.006	0.308E-02	0.261E-02	0.237E-03	0.771E-01
				0.500	1.560	-0.008	0.304E-02	0.245E-02	0.198E-03	0.650E-01
				0.355	1.580	-0.022	0.289E-02	0.179E-02	0.705E-04	0.244E-01
				0.266	1.600	-0.048	0.283E-02	0.154E-02	0.147E-04	0.521E-02
High concentration	0.60	2.10	1.00	1.064	1.530	-0.004	0.831E-02	0.760E-02	0.610E-03	0.733E-01
				0.694	1.550	-0.004	0.762E-02	0.667E-02	0.596E-03	0.783E-01
				0.532	1.560	-0.006	0.734E-02	0.587E-02	0.429E-03	0.585E-01
				0.500	1.560	-0.008	0.731E-02	0.549E-02	0.337E-03	0.461E-01
				0.355	1.580	-0.022	0.717E-02	0.422E-02	0.790E-04	0.110E-01
				0.266	1.600	-0.048	0.702E-02	0.380E-02	0.167E-04	0.238E-02

* Nominal value of particle concentration; actual values are determined by the profiles.

Prospero.⁵⁰ The distribution for our typical concentration is approximately that reported by Savoie and Prospero as the geometric mean for the distributions observed at Sal Island. These data, as well as the results discussed by Grams et al.,⁵¹ indicate that the highest concentrations are characterized by the presence of relatively large particles, so our high concentration model has a slightly larger mass mean radius. The size distribution for the low concentration model is representative of the conditions measured on Barbados by Savoie and Prospero; the characteristic sizes are smaller than the other cases, reflecting losses of larger particles during their transport across the Atlantic.

The refractive indices of the Saharan aerosol model are those reported by Patterson et al.⁵² and by Patterson.⁵³ Patterson et al.⁴⁹ reported the real index of refraction n_{RE} at two wavelengths: $0.63 \mu\text{m}$ and a rather broad interval centered at $0.55 \mu\text{m}$. From these data points, a wavelength dependence was estimated for the interval between 0.45 and $0.7 \mu\text{m}$. This estimated n_{RE} was used for the laser wavelengths of 0.53 and $0.69 \mu\text{m}$; the modeled n_{RE} at 0.266 and 0.355 ; and $1.06 \mu\text{m}$ was determined by extrapolation. The imaginary index of refraction n_{IM} was measured between 0.25 and $0.70 \mu\text{m}$ as shown in Figure A-5. n_{IM} at $1.06 \mu\text{m}$ was assumed to be equal to that at $0.7 \mu\text{m}$, an assumption based on several measurements that show little variation in n_{IM} between 0.7 and $1.0 \mu\text{m}$ (Ref. 54, for example). Measurements of Saharan aerosol samples collected on both sides of the Atlantic showed no significant variation in either real or imaginary index with distance from the source; consequently, we chose the same wavelength-dependent refractive indices for our models. Also, since the crustal aerosol is nonhygroscopic, no corrections to these measured optical properties to account for variations in relative humidity were applied.

Although the size and refractive index measurements discussed above show a great deal of uniformity, the concentrations and vertical distributions of the Saharan aerosol can vary widely. Some measured relative concentration profiles for the eastern Atlantic and the western

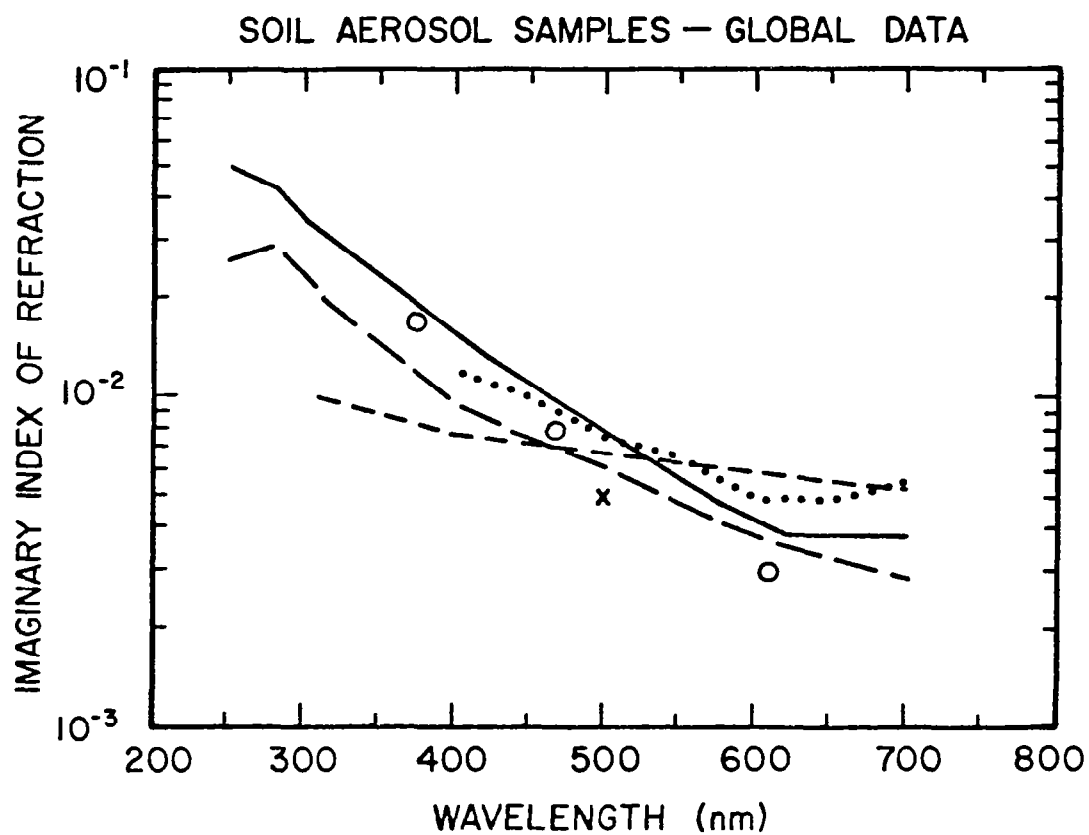


FIGURE A-5 n_{IM} VALUES DETERMINED FOR CRUSTAL AEROSOLS FROM VARIOUS GLOBAL SOURCES

Saharan aerosols (—, O); North American aerosols (---, x); and a southwest Asian desert aerosol (···). Also shown is a relative n_{IM} curve determined from absorption data (— · —) (from Patterson⁵³).

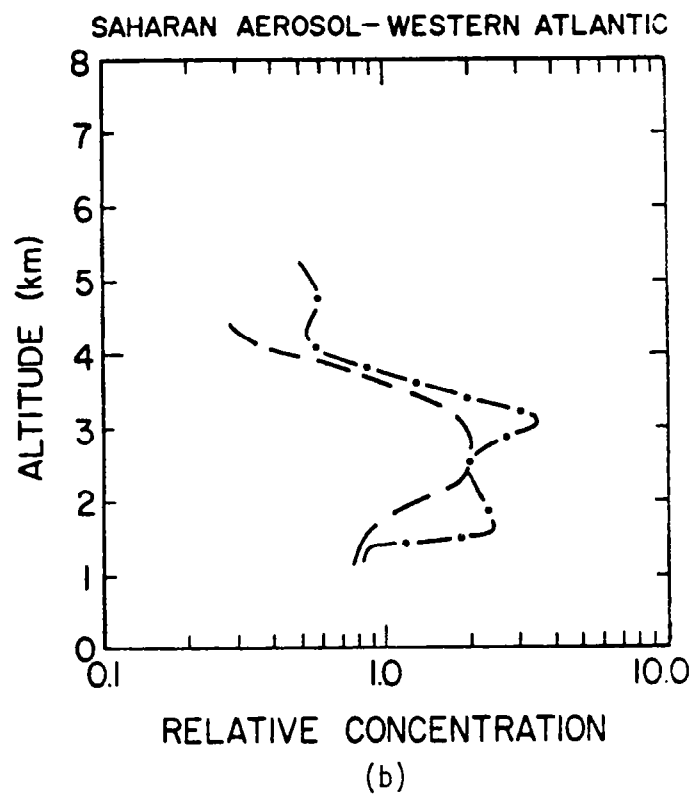
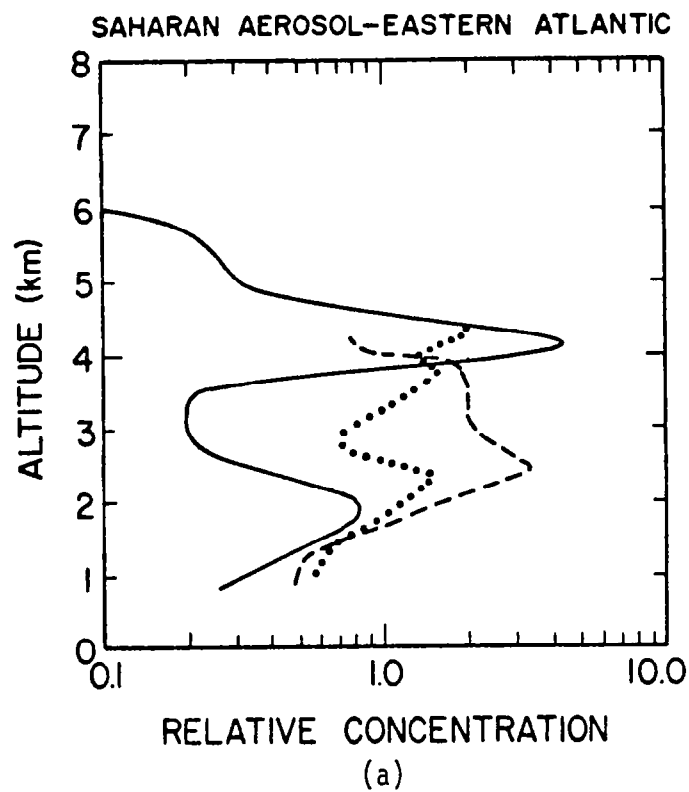


FIGURE A-6 RELATIVE CONCENTRATION PROFILES OF THE SAHARAN AEROSOL MEASURED IN THE EASTERN ATLANTIC (a) AND IN THE WESTERN ATLANTIC (b)

The data are those of Grams et al.⁵¹ (···, ---), Kondratyev et al.⁵⁵ (—), and Prospero and Carlson⁵⁶ (——, -·-·-·).

Atlantic are shown in Figure A-6(a,b). The profiles in Figure A-6(a) are derived from Kondratyev⁵⁵ and Grams (unpublished data); those in Figure A-6(b) were reported by Prospero and Carlson.⁵⁶ The Kondratyev profile is based on a measurement of relative number, that of Grams on relative light scattering cross sections, and that of Prospero on relative mass concentrations. Each profile is consistent, having a base at approximately 1 km and a top at 4 to 5 km. The layering in these profiles is a common feature of the aerosol distribution, but the details are quite variable. For our model, we chose the profile published by Kondratyev⁵⁵ for the high and the typical concentration cases and the layered profile published by Prospero⁵⁶ for the low concentrations cases. The aerosol concentrations in our model were normalized to the total optical depth of the Saharan layer, as measured during summer. We chose optical depths of approximately 1 for high concentrations, 0.5 for typical concentrations, and 0.2 for low concentrations. The high concentration value is based on the averages of Carlson and Caverly⁵⁷ for high turbidity days at Sal Island during GATE; the typical concentration optical depth is based on average turbidities at Sal Island during GATE; and the low concentration value is based on average turbidities for Barbados during GATE. These summer measurements represent maximum turbidities for the time at which the transport of dust is at a maximum; winter measurements may be lower by as much as a factor of ten. In addition, a time series of concentration measurements for the Barbados samples for the years 1965-75 shows that the GATE measurements of summer 1974 were among the highest in the time considered. The lowest summer measurements were lower by approximately a factor of 3 than the summer maxima considered in our model. The winter minima were approximately equal in all of the years.

F. Marine Aerosol

The size distributions and refractive indices used in the marine aerosol models are based on the work of Toon and Pollack⁴⁸ and Shettle and Fenn.³⁴ Table A-4 summarizes these properties.

Table A-4

SIZE DISTRIBUTIONS, REFRACTIVE INDICES, AND OPTICAL CONVERSION RATIOS FOR THE MARINE AEROSOL MODELS

Size Distribution	Refractive Index	$B_p(\lambda)/E_p(\lambda) - \text{sr}^{-1}$					$B_p(\lambda)/N(r \geq 0.15 \mu\text{m}) - 10^{-6} \text{ km}^{-1} \text{ sr}^{-1}/\text{cm}^{-3}$					
		$\lambda(\mu\text{m}) =$					$\lambda(\mu\text{m}) =$					
		0.266	0.353	0.532	0.694	1.064	0.266	0.353	0.532	0.694	1.064	Weight
Segmented power law [Eqs. (A2,A3)]*	1.52-01	0.069	0.067	0.067	0.067	0.066	109.0	103.7	96.3	91.0	81.9	0.333
	1.525-0.0051	0.037	0.038	0.041	0.043	0.046	57.7	58.1	58.4	58.2	56.5	0.167
Bimodal log normal [Eq. (A4)]†	1.52-01	0.062	0.065	0.072	0.075	0.076	127.1	123.0	121.7	121.8	116.6	0.333
	1.525-0.0051	<u>0.031</u>	<u>0.035</u>	<u>0.043</u>	<u>0.049</u>	<u>0.055</u>	<u>62.6</u>	<u>65.2</u>	<u>73.0</u>	<u>78.9</u>	<u>83.7</u>	<u>0.167</u>
	Weighted average	0.055	0.056	0.060	0.062	0.064	98.7	96.1	94.5	93.8	89.5	
	Standard deviation, %	31.	28.	24.	22.	19.	31.	29.	27.	26.	26.	

* Reference 48.

† Reference 34.

The equation of the Toon and Pollack⁴⁸ size distribution is

$$n(r) = \begin{cases} C & r \leq 0.1 \text{ } \mu\text{m} \\ C \left(\frac{0.1}{r} \text{ } \mu\text{m} \right)^{v+1} & 0.1 \text{ } \mu\text{m} \leq r \leq 5.0 \text{ } \mu\text{m} \\ 0 & r \geq 5.0 \text{ } \mu\text{m}, \end{cases} \quad (\text{A-2})$$

where

$$v = \begin{cases} 2.0 & 0.1 \text{ } \mu\text{m} \leq r \leq 5.0 \text{ } \mu\text{m} \\ 4.0 & 5.0 \text{ } \mu\text{m} \leq r \leq 50 \text{ } \mu\text{m} \end{cases}, \quad (\text{A-3})$$

and $n(r)dr$ is the number of particles with radii between r and $r + dr$. Toon and Pollack⁴⁸ developed this equation as a best-fit solution to a collection of tropospheric aerosol measurements selected to represent the global background aerosol for heights below 3 km. Because most of the Earth's surface is covered by oceans, we adopted this distribution as a likely descriptor of the marine aerosol (i.e., the aerosol present over the ocean surface, whether of continental or marine origin).

The equation of the Shettle and Fenn³⁴ marine aerosol is

$$n(r) = \sum_{i=1}^2 \frac{N_i}{\ln 10 \text{ } r \sigma_i \sqrt{2\pi}} \exp - \left[\frac{(\log r - \log r_i)^2}{2\sigma_i^2} \right], \quad (\text{A-4})$$

where

$$\begin{aligned} N_2 &= N_1 \times 4.71 \times 10^{-4} \\ r_1 &= 0.005 \text{ } \mu\text{m} \\ r_2 &= 0.3 \text{ } \mu\text{m} \\ \sigma_1 &= 0.475 \\ \sigma_2 &= 0.4. \end{aligned}$$

The small-particle mode [$i = 1$ in Eq. (A-4)] represents particles of continental origin; the large-particle mode [$i = 2$] represents those of

sea-spray origin. Although this suggests that the two modes are likely to have different refractive indices, for the purposes of our model we keep refractive index independent of particle size.

With guidance from Toon and Pollack⁴⁸ we modeled the marine aerosol composition as one-third soil particles (taken as basalt), two-thirds sea salt (taken as NaCl), and traces of sulfate [taken as $(\text{NH}_4)_2\text{SO}_4$]. The refractive index of the soil particles is taken as 1.525-0.005i^{48,58,59} and that of the sea salt and sulfate as 1.52-0i (see Table A-4). The latter value is somewhat less than that quoted in the literature for pure NaCl (1.58-1.53--see Toon et al.⁶⁰) and allows for a small water admixture caused by the deliquescence of NaCl and the typically high relative humidity of marine environments. We modeled these refractive indices independently of wavelength. The data of Toon et al.⁶⁰ show that, for NaCl and $(\text{NH}_4)_2\text{SO}_4$, this approximation is good to an accuracy of ± 0.02 for the real part and 10^{-7} for the imaginary part over the wavelength region 0.35 to 1.06 μm .

Mie-scattering calculations were made for each combination of size distribution and refractive index shown in Table A-4. Each combination yielded the multiwavelength backscatter-to-extinction and backscatter-to-number ratios shown. Weighted averages of these ratios were then taken and used to derive multiwavelength backscattering profiles from specified midvisible optical thickness values and relative vertical profiles, as described below. Our reason for averaging the results of the Mie-scattering calculations, rather than averaging the refractive indices input to the Mie calculations, was to avoid errors caused by the nonlinear dependence of scattering and extinction on refractive index. These errors are discussed at some length by Bergstrom⁶¹ and Toon et al.⁶⁰

The vertical distribution of our marine aerosol models was based on the lidar measurements reported by Livingston and Uthe,⁶² who noted that the surface-based marine haze layer in the Atlantic and Mediterranean had a mean height of 0.5 km with a standard deviation of 0.3 km for the 22-day cruise they reported. They also noted that elevated layers below

3.6 km in altitude were usually present, and that as a result the surface-based layer typically accounted for less than one-half of the vertically integrated backscatter below 3.6 km.

With these results in mind, we adopted a three-layer model for the marine aerosol. As shown in Figure 2 of the main text, the surface-based layer has constant backscatter mixing ratio up to a height of 0.4 km for the high-latitude version and 0.6 km for the mid- and low-latitude versions. The elevated layers are independent of latitude and centered at heights of 1.5 and 2.5 km, with approximately Gaussian shapes and half-width (HWHM) of 0.5 km. These layers have equal peak values for backscatter mixing ratio, with the peak value adjusted so that the surface-based layer contains only about 50 percent of column backscatter below 3.6 km.

The absolute backscattering coefficients in our marine aerosol models were determined by combining backscatter-to-extinction ratios for the averaged model optical properties (Table A-4) with the requirement that the midvisible ($\lambda = 0.53 \mu\text{m}$) optical depth of the marine aerosol be 0.16 for the high-latitude case and 0.19 for the low- and mid-latitude cases. These values may be compared with a large set of time-averaged maritime tropospheric midvisible optical depths summarized by Toon and Pollack.⁴⁸ The values selected by Toon and Pollack⁴⁸ to represent cases with little continental influence ranged from 0.02 to 0.17, with the larger values tending to occur at low latitudes. The midvisible particulate extinction coefficient $E_p(0.53 \mu\text{m})$ at the surface for each of our marine aerosol models is 0.167 km^{-1} . Using the fact that $E_p(0.53 \mu\text{m}) \approx E_p(0.55 \mu\text{m})$ and that the gaseous Rayleigh extinction coefficient $E_{sg}(0.55 \mu\text{m}) \approx 0.012$ yields a total extinction coefficient,

$$E(0.55 \mu\text{m}) \approx 0.18 \text{ km}^{-1} . \quad (\text{A-5})$$

The Koschmieder relation,

$$V = \frac{3.91}{E(0.55 \mu\text{m})} , \quad (\text{A-6})$$

yields a surface meteorological range V of 22 km (13.5 miles) for each model. As noted by Elterman⁶³ and Collis and Russell,⁶⁴ such a meteorological range is associated with very light haze conditions, usually described as "clear." Thus, although our marine aerosol models tend to have somewhat larger optical thicknesses than the globally averaged, no-continental-influence values of Toon and Pollack,⁴⁸ they nevertheless represent light haze conditions.

G. Cirrus Clouds

In contrast to our aerosol models, our cirrus cloud models are based on empirical (visual, lidar, radiometric, in-situ) observations of cloud macroproperties, rather than on calculations from cloud microproperties (ice crystal number density, size distribution, shape, and orientation). Since clouds are highly variable, we have included three cirrus layers of different density, height, and geometrical thickness in each latitude band of the model, rather than trying to describe some "typical" state. Figure A-7 shows the cirrus layers in terms of multiwavelength backscatter mixing ratios, each superimposed on the nonvolcanic aerosol model for the corresponding latitude band. Table A-5 lists several properties of these layers.

The properties listed in Table A-5 were derived as follows. Each layer's top height is given by h_T , and its geometrical thickness by Δh . The mean midvisible gas backscattering coefficient in the layer, $B_g(0.53 \mu\text{m})$, is computed from the corresponding profile of gas density D using

$$B_g(0.53 \mu\text{m}) = \gamma(0.53 \mu\text{m}) D(h_T, \Delta h) , \quad (\text{A-7})$$

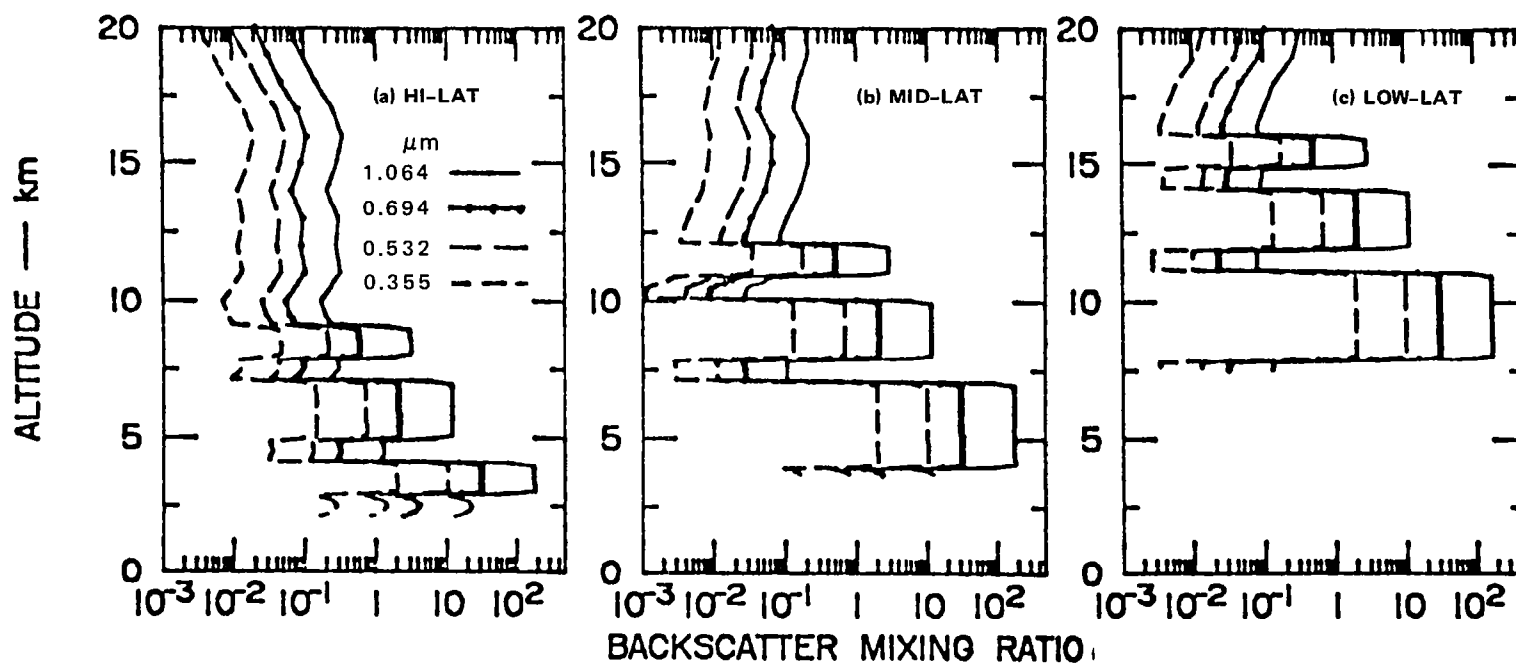


FIGURE A-7 CIRRUS CLOUD MODEL BACKSCATTER MIXING RATIOS SUPERIMPOSED ON THE MODEL AEROSOL IN EACH LATITUDE BAND

Table A-5

PROPERTIES OF MODEL CIRRUS CLOUD LAYERS

h_T (km)	Δh (km)	$R(0.53 \mu m)$	$B_g(0.53 \mu m)$ ($m^{-1} sr^{-1}$)	B_p ($m^{-1} sr^{-1}$)	r^*	r^\dagger	Visibility ‡	w^s ($g m^{-3}$)
High-Latitude								
9	1	1.16	6×10^{-7}	1×10^{-7}	0.005	0.002	s	1.5×10^{-4}
7	2	1.67	8×10^{-7}	5×10^{-7}	0.05	0.02	s	7×10^{-4}
4	1	11.00	1×10^{-6}	1×10^{-5}	0.5	0.2	v	1.5×10^{-1}
Mid-Latitude								
12	1	1.16	4×10^{-7}	5×10^{-8}	0.013	0.0012	s	7×10^{-5}
10	2	1.67	6×10^{-7}	4×10^{-7}	0.04	0.016	s	6×10^{-4}
7	3	11.00	8×10^{-7}	8×10^{-5}	1.2	0.48	v	1×10^{-1}
Low-Latitude								
16	1	1.16	1×10^{-7}	2×10^{-8}	0.001	0.0004	s	5×10^{-5}
14	2	1.67	3×10^{-7}	2×10^{-7}	0.02	0.008	s	3×10^{-4}
11	3	11.00	6×10^{-7}	6×10^{-6}	0.9	0.36	v	2×10^{-1}

* Assumes intrinsic backscatter-to-extinction ratio, $\Gamma = 0.02 sr^{-1}$.

† Assumes effective backscatter-to-extinction ratio, $\Gamma' = 0.05 sr^{-1}$.

‡ Based on B_p , Δh , and previous comparisons of lidar, human observer, and satellite TV data. See Table A-6.

§ Assumes effective particle radius, $a = 50 \mu m$.

where γ is the Rayleigh backscatter-to-mass ratio for air, given by:

$$\gamma(0.53 \mu m) = 1.30 \times 10^{-9} m^2 sr^{-1} g^{-1} . \quad (A-8)$$

Cloud particle backscattering coefficients are then derived using the specified scattering ratios R and

$$B_p = B_g(0.53 \mu m) \times [R(0.53 \mu m) - 1] . \quad (A-9)$$

Note that we have omitted a wavelength descriptor from the left side of Eq. (A-9) because the size of cirrus particles is large compared to the wavelengths used in this study. We therefore used the geometric optics approximation that cloud particle backscatter and extinction were independent of wavelength.

Optical thicknesses τ are obtained from

$$\tau = B_p \Delta h / \Gamma , \quad (\text{A-10})$$

where Γ is the cloud particle backscatter-to-extinction ratio. Following the empirical data of Platt,⁶⁵ we modeled cirrus clouds as having

$$\Gamma = 0.020 \text{ sr}^{-1} . \quad (\text{A-11})$$

Again, because cirrus crystals are large in comparison to the wavelengths used in this study, lidar measurements of cirrus can be strongly affected by multiple scattering. That is, light-scattering by cirrus particles is very strongly forward-peaked, thus returning much scattered light to (or near) the original direction of travel. These multiple scattering effects can be described in an approximate way by using an effective backscatter-to-extinction ratio Γ' in computing lidar pulse transmissivities. Platt⁶⁵ has had success using

$$\Gamma' = 0.05 \text{ sr}^{-1} \quad (\text{A-12})$$

in his studies, and we have adopted his value in our models. Note that Γ' exceeds Γ because multiple scattering tends to decrease the effective extinction coefficient for a given backscatter coefficient. Lidar pulse transmission is described by an effective optical thickness, defined analogously to Eq. (A-10) as:

$$\tau' = B_p \Delta h / \Gamma' . \quad (\text{A-13})$$

To aid in relating our model cloud layers to observable physical characteristics, the last two columns of Table A-5 give approximate descriptors of cloud visibility and water content. A cloud's visibility to ground-based human observers can be related to backscatter or optical thickness values only very approximately. Nevertheless, some useful distinctions can be developed on the basis of the large set of lidar, human observer, and satellite TV observations acquired in many seasons and latitudes by Evans.¹ These distinctions are summarized in Table A-6. On the basis of Table A-6 we classified each of our model cirrus layers as either visible or subvisible (to a ground-based human observer). As can be seen from Table A-5, in each latitude band of the model the top two cloud layers are nominally subvisible, whereas the bottom layer is nominally visible. Further, the top layer in each band is similar in optical and physical density to the weakest cloud described by Uthe and Russell.⁶⁶ However, the model layer is geometrically thicker than the measured layer.

Cloud water content can be approximately derived from the backscatter values by treating the particles as spheres and assuming an effective particle radius, a . Again, using the geometric optics approximation, one can relate particle number density N and extinction coefficient E_p by

$$N = \frac{E_p}{2\pi a^2} . \quad (A-14)$$

Cloud water content is given by

$$W = \frac{4}{3} \pi a^3 \rho N , \quad (A-15)$$

Table A-6

APPROXIMATE RELATIONSHIPS BETWEEN CIRRUS CLOUD BACKSCATTER,
THICKNESS, AND VISIBILITY*

Particle Backscatter Coefficient ($\text{m}^{-1} \text{sr}^{-1}$)				
10^{-7}	10^{-6}	10^{-5}	10^{-4}	10^{-3}
	Weak Cirrus	Medium Cirrus	Strong Cirrus	
Never observed visually	Daytime visible only if $\Delta h > 2 \text{ km}$	Daytime visible if $\Delta h > 0.5 \text{ km}$	Always daytime visible; may even appear opaque	
	Seldom detected via satellite TV		Moonlight visible under good conditions if $\Delta h > 1 \text{ km}$	

* Based on Reference 1.

where ρ is particle mass density (0.92 g cm^{-3} for ice, 1 g cm^{-3} for water). Combining Eqs. (A-14) and (A-15) with the definition of the backscatter-to-extinction ratio,

$$\Gamma \equiv B_p/E_p \quad , \quad (\text{A-16})$$

then yields

$$W = \frac{2}{3} \frac{a\rho}{\Gamma} B_p \quad . \quad (\text{A-17})$$

For ice crystals, this in turn yields

$$W(\text{g m}^{-3}) = 30a(\mu\text{m})B_p(\text{m}^{-1} \text{sr}^{-1}) \quad . \quad (\text{A-18})$$

The W values shown in Table A-5 were derived from Eq. (A-18) using an effective particle radius a of $50 \mu\text{m}$. By comparison, the in-situ

measurements of Varley and Brooks⁶⁷ showed that the particle radius contributing most effectively to ice content in sampled cirrus clouds ranged approximately from 10 to 100 μm .

Appendix B

BACKSCATTER-TO-EXTINCTION RATIOS

The lidar data analysis method assumed in this study constructs particulate extinction profiles $E_p(z)$ by dividing lidar-derived backscatter profiles $B_p(z)$ by a possibly height-dependent model backscatter-to-extinction ratio, $\gamma_p(z)$. Thus, the uncertainty in γ_p contributes to the uncertainty in particulate optical depth τ_p . In fact, for the cases of practical concern in this study, where $0.01 \leq \tau_p \leq 1.0$, $\delta\gamma_p/\gamma_p$ is the dominant contributor to $\delta\tau_p/\tau_p$. In some cases this dominance results from a need to solve iteratively for $B_p(z)$ and $E_p(z)$ profiles that are consistent with the model $\gamma_p(z)$ profile.

Because of the importance of $\delta\gamma_p/\gamma_p$ in determining $\delta\tau_p/\tau_p$ [and hence the transmission-induced uncertainty in $B_p(z)$ --see Eqs. (12), (20), and (24)] we have surveyed model and measured values of γ_p as a means of evaluating the possible range of values (and hence the uncertainty in any chosen model value). Also, we have searched for correlations between γ_p and the parameter α defined by

$$\frac{B_p(0.53 \text{ } \mu\text{m})}{B_p(1.06 \text{ } \mu\text{m})} = \left(\frac{0.53}{1.06} \right)^{-\alpha}, \quad (\text{B-1})$$

or

$$\alpha = \frac{\ln[B_p(0.53 \text{ } \mu\text{m})/B_p(1.06 \text{ } \mu\text{m})]}{\ln 2}. \quad (\text{B-2})$$

Our reason for investigating this correlation is that α can be determined from a lidar measurement of $B_p(0.53 \text{ } \mu\text{m})/B_p(1.06 \text{ } \mu\text{m})$; hence, if α and γ_p are correlated, knowledge of $B_p(0.53 \text{ } \mu\text{m})/B_p(1.06 \text{ } \mu\text{m})$ can be used to reduce uncertainty in γ_p . [For an illustration of this process, see Ref. 44.]

The results of this survey are shown in Figure B-1. Figures B-1(a) and B-1(c) show model values of $\gamma_p(0.53 \mu\text{m})$ and $\gamma_p(1.06 \mu\text{m})$ calculated for the various aerosol and cloud models used in this study, each plotted versus the corresponding value of α . (For details on model size distributions and refractive indices, see Appendix A, Sections A-3 through A-7.) These results indicate that γ_p does not depend very strongly on wavelength. Figure B-1(b) shows values of $\gamma_p(0.69 \mu\text{m})$ measured in experiments using ruby lidars. Since α was not measured in these experiments, $\gamma_p(0.69 \mu\text{m})$ cannot be plotted versus α , but nevertheless the range of $\gamma_p(0.69 \mu\text{m})$ can be seen.

A. Stratospheric Aerosols

Many comparison studies have shown that stratospheric aerosols are described fairly well by spherical-particle models of the type used to construct the curves in Figure B-1(a,c). (For a summary of such comparisons, see Appendix A and Ref. 44.) Thus, although measurements of stratospheric γ_p are not available, the model results in Figures B-1(a,c) can be adopted with some confidence. These results indicate that for the stratospheric aerosol, α is a good predictor of $\gamma_p(0.53 \mu\text{m})$, provided $\alpha \leq 1.5$, as it is for most stratospheric aerosols. However, the practical value of this predictive ability is diminished by the facts that:

- For the background stratospheric aerosol, α is difficult to measure by lidar because $B_p(0.53 \mu\text{m})$ is difficult to measure. [Uncertainties in molecular density severely degrade measurements of $B_p(0.53 \mu\text{m})$ at most stratospheric heights, even when using the three-wavelength analysis technique.]
- Highly accurate particulate backscatter-to-extinction ratios are not required for deriving lidar backscatter profiles in the unperturbed stratosphere, because stratospheric particulate transmission is nearly unity and thus is a small source of uncertainty in analyzing lidar data.

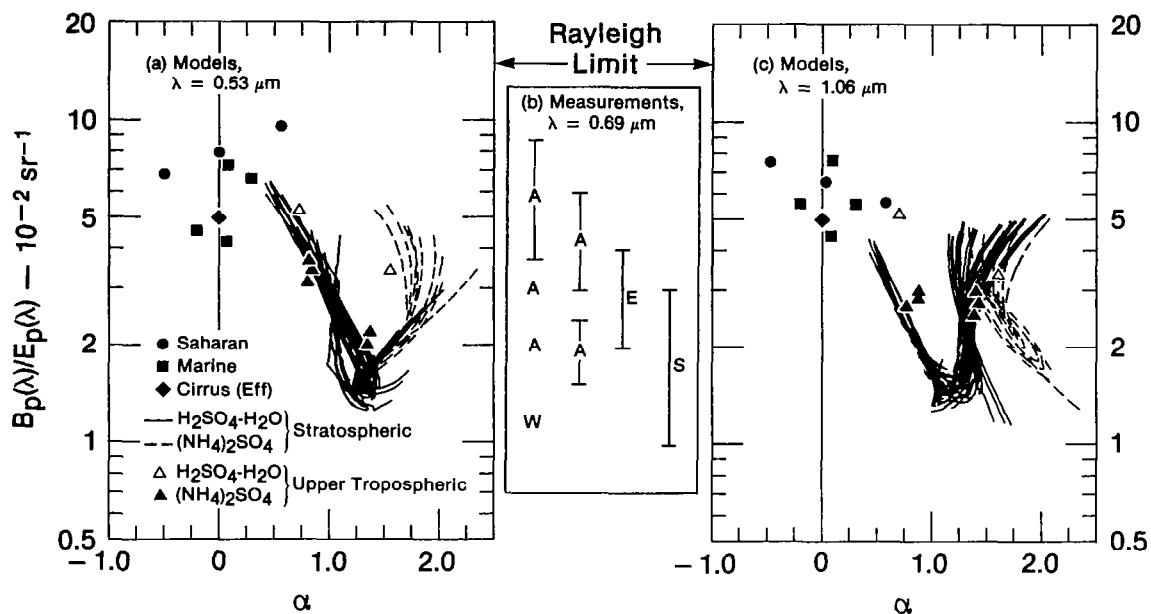


FIGURE B-1 MODEL AND MEASURED VALUES OF PARTICULATE BACKSCATTER-TO-EXTINCTION RATIO, γ_p

(a) Model values for $\lambda = 0.53 \mu\text{m}$, plotted versus α defined by Eq. (B-2); (b) Measured values for $\lambda = 0.69 \mu\text{m}$. Letters indicate locations (all lower tropospheric). A = Tucson, Arizona (Refs. 68-71); S = San Francisco (Ref. 20); W = Seattle, Washington (Ref. 73); E = Hempstead, England (Ref. 74); (c) as in (a) but for $\lambda = 1.06 \mu\text{m}$.

B. Tropospheric Aerosols

The most critical need for a well-defined relationship of γ_p versus α is in the troposphere, because it is here that aerosol transmission uncertainties become significant error sources in analyzing lidar data. Here, α can frequently be measured more accurately than in the stratosphere. Unfortunately, Figures B-1(a,c) show that, for the tropospheric aerosol models, the correlation between γ_p and α is very weak. In fact, any systematic variation of γ_p appears to be as well predicted by location (plus backscatter strength) as by α --that is, the marine and Saharan values for γ_p systematically exceed those for the upper troposphere (excluding the Saharan cases). The reason that there is no well-defined relationship for γ_p versus α within any of these groups is

the large range and sometimes strong wavelength dependence of refractive index (real and imaginary) in the troposphere as compared to the stratosphere.

Given this result, one can adopt the alternate approach of selecting γ_p on the basis of aerosol location, independent of α . A measure of the uncertainty for this approach can be obtained by calculating the mean and standard deviation of the appropriate groups of data points in Figures B-1(a,c). The results, shown in Table B-1(a,b) yield 1 σ uncertainties ranging from 19 to 37 percent of the mean.

However, this approach may underestimate tropospheric $\delta\gamma_p/\gamma_p$, and overestimate γ_p , because the input set of models is limited--in particular by excluding all highly absorbing urban aerosols and all nonspherical aerosol particles. Such particles typically have smaller γ_p values than do spherical-particle models with little or moderate absorption. This concern is supported by the measured lower tropospheric data points in Figure B-1(b), which are systematically smaller than the corresponding model points in Figures B-1(a,c). It would be useful to calculate the mean and standard deviation of all the measured data points in the experiments referred to in Figure B-1(b). However, this is not possible because many of the references do not give individual data points. An approximate approach is to calculate the mean and standard deviation of two sets shown in Figure B-1(b): (1) The eight "central" data points; and (2) the central data points plus the ten upper and lower error bar extremes. The results are shown in Table B-1(c). Note the smaller values for γ_p and larger values for $\delta\gamma_p/\gamma_p$, as compared to the model values in Table B-1(b).

C. Clouds

The only cloud value for γ_p included in Figures B-1(a,c) is the cirrus value 0.05 sr^{-1} (independent of wavelength). This is an effective value adopted by Platt⁶⁵ and by the authors of this study to include multiple scattering effects. Recently, several studies^{74,75}

Table B-1

MODEL AND MEASURED AEROSOL PARTICLE BACKSCATTER-TO-EXTINCTION RATIOS

(a) Model Values, Upper Troposphere (excluding Saharan) [Figs. B1(a,c)]			
$\lambda(\mu\text{m})$	$\gamma_p(\text{sr}^{-1})$	$\delta\gamma_p(\text{sr}^{-1})$	$\delta\gamma_p/\gamma_p(\%)$
0.53	0.023	0.007	31
1.06	0.023	0.005	19
(b) Model Values, Marine and Saharan [Figs. B1(a,c)]			
$\lambda(\mu\text{m})$	$\gamma_p(\text{sr}^{-1})$	$\delta\gamma_p(\text{sr}^{-1})$	$\delta\gamma_p/\gamma_p(\%)$
0.53	0.054	0.020	37
1.06	0.053	0.016	32
(c) Measured Values, Lower Troposphere, $\lambda = 0.69 \mu\text{m}$ [Fig. B1(b)]			
Set*	$\gamma_p(\text{sr}^{-1})$	$\delta\gamma_p(\text{sr}^{-1})$	$\delta\gamma_p/\gamma_p(\%)$
1	0.028	0.014	50
2	0.033	0.021	66

* See text for definition of sets.

have shown that single-scattering γ_p values for a wide range of spherical water-droplet cloud and fog models vary by only about 15 percent around the mean value 0.06 sr^{-1} for wavelengths between 0.5 and $1.06 \mu\text{m}$. However, this small variation must be viewed with caution in lidar studies. First, water-droplet clouds are usually optically dense, so that multiple scattering effects must be taken into account in attempting to infer quantitative values of B_p from the lidar return. Second, although

cirrus clouds are frequently tenuous, the large size of the crystals produces very strong forward scattering (a multiple scattering effect that decreases effective extinction); also, the crystals can be markedly aspherical. Thus, the small variation of single-scattering spherical water-droplet γ_p is not applicable to the lidar measurements in this study. Given the wide range of crystal shapes, orientations, and sizes, as well as cloud optical densities, it appears that the relative uncertainty in cirrus γ_p must be considerably larger than 15 percent.

D. Summary

On the basis of the above results, we have adapted 50 percent as a rough measure of the relative 1σ uncertainty in γ_p , and hence in τ_p , for our simulations. (See the first paragraph of this appendix.) However, it can be seen that this value should be revised upward or downward in particular circumstances, and hence this is an area for careful attention in individual measurements.

REFERENCES

1. Evans, W.E.: Remote Probing of High Cloud Cover via Satellite-Borne Lidar. NASA CR-96893, 1968.
2. Shipley, S.T.; Joseph, J.H.; Trauger, J.T.; Guetter, P.J.; Eloranta, E.W.; Lawler, J.E.; Wiscombe, W.J.; Odell, A.P.; Roesler, F.L.; and Weinman, J.A.: The Evaluation of a Shuttle Borne Lidar Experiment to Measure the Global Distribution of Aerosols and Their Effect on the Atmospheric Heat Budget. (Department of Meteorology, University of Wisconsin, Madison, Wisconsin 53706; NASA Grant NSG 1057.) April 1975. (NASA CR-146134, 1975.)
3. Collis, R.T.H.; Hake, R.D.; Russell, P.B.; and Bowhill, S.A.: Lidar in Space. Optical Engineering, vol. 17, no. 1, Jan.-Feb. 1978, pp. 23-29.
4. Greco, R.V.: Atmospheric Lidar Multi-User Instrument System Definition Study. NASA CR-3303, 1980.
5. Shuttle Atmospheric Lidar Research Program. Final Report of the Atmospheric Lidar Working Group, NASA SP-433, 1979.
6. Brehm, W.F.; and J.L. Buckley: Design Study of a Laser Radar System for Spaceflight Application. Final Report, General Electric Space Division, to Air Force Geophysics Laboratory, Hanscom AFB, Massachusetts. (AFGL-TR-79-0624, 1979.)
7. Russell, P.B.; Swissler, T.J.; and McCormick, M.P.: Methodology for Error Analysis and Simulation of Lidar Aerosol Measurements. Appl. Opt., vol. 18, no. 22, Nov. 15, 1979, pp. 3783-3797.

8. Fiocco, G.; and Grams, G.W.: Optical Radar Observations of Mesospheric Aerosols in Norway During the Summer 1966. *J. Geophys. Res.*, vol. 74, no. 10, May 15, 1969, pp. 2453-2458.
9. Kent, G.S.; Clemesha, B.R.; and Wright, R.W.: High Altitude Atmospheric Scattering of Light from a Laser Beam. *J. Atm. Terr. Phys.*, vol. 29, 1967, pp. 169-181.
10. Clemesha, B.R.; and Nakamura, Y.: Dust in the Upper Atmosphere. *Nature*, vol. 237, June 9, 1972, pp. 328-329.
11. Clemesha, B.R.; and Simonich, D.M.: Stratospheric Dust Measurements, 1970-1977. *J. Geophys. Res.*, vol. 83, no. C5, May 20, 1978, pp. 2403-2408.
12. Gambling, D.J.; Bartusek, K.; and Elford, W.G.: A 12-Month Study of Aerosols Below 60 km. *J. Atm. Terr. Phys.*, vol. 33, 1971, pp. 1403-1413.
13. Fegley, R.W.; and Ellis, H.T.: Optical Effects of the 1974 Stratospheric Dust Cloud. *Appl. Opt.*, vol. 14, no. 8, Aug. 1975, pp. 1751-1752.
14. Itabe, T.; Fujiwara, M.; and Hirono, M.: Temporal Variation of the Stratospheric Aerosol Layer After the Fuego Eruption Observed by Lidar in Fukuoka. *J. Met. Soc. Japan*, vol. 55, no. 6, Dec. 28, 1977, pp. 606-612.
15. Fernald, F.G.; and Schuster, B.G.: Wintertime 1973 Airborne Lidar Measurements of Stratospheric Aerosols. *J. Geophys. Res.*, vol. 82, no. 3, Jan. 20, 1977, pp. 433-437.
16. McCormick, M.P.; Swissler, T.J.; Chu, W.P.; and Fuller, W.H.: Post-Volcanic Stratospheric Aerosol Decay as Measured by Lidar. *J. Atmos. Sci.*, vol. 35, July 1978, pp. 1296-1303.

17. Reiter, R.; Jager, H.; Carnuth, W.; and Funk, W.: Lidar Observations of the Mount St. Helens Eruption Clouds Over Mid-Europe, May to July 1980. *Geophys. Res. Lett.*, vol. 7, December 1980, pp. 1099-1101.
18. Russell, P.B.; and Hake, R.D.: The Post-Fuego Stratospheric Aerosol; Lidar Measurements, With Radiative and Thermal Implications. *J. Atmos. Sci.*, vol. 34, no. 1, Jan. 1977, pp. 163-177.
19. Gambling, D.J.; and Bartusek, K.: Lidar Observations of Tropospheric Aerosols. *Atmos. Env.*, vol. 6, 1972, pp. 181-190.
20. Russell, P.B.; Livingston, J.M.; and Uthe, E.E.: Aerosol-Induced Albedo Change: Measurement and Modeling of an Incident. *J. Atmos. Sci.*, vol. 36, no. 8, Aug. 1979, pp. 1588-1608.
21. Thekakera, M.P.: Extraterrestrial Solar Spectrum, 3000-6100A at 1-A Intervals. *Appl. Opt.*, vol. 13, no. 3, 1974, pp. 518-522.
22. Evans, W.E.: Design of an Airborne Lidar for Stratospheric Aerosol Measurements. NASA CR-145179, 1977.
23. Russell, P.B., ed.: Sage Ground Truth Plan--Correlative Measurements for the Stratosphere Aerosol and Gas Experiment (SAGE) on the AEM-B Satellite. NASA TM-80076, 1979.
24. Young, A.T.: Revised Depolarization Corrections for Atmospheric Extinction. *Appl. Opt.*, vol. 19, no. 20, 15 Oct. 1980, pp. 3427-3428.
25. Noxon, J.F.; Whipple, E.C.; and Hyde, R.S.: Stratospheric NO₂ 1.: Observational Method and Behavior at Mid-Latitude. *J. Geophys. Res.*, vol. 84, no. C8, 20 Aug. 1979, pp. 5047-5065.
26. Hudson, R.D. ed.: Chlorofluoromethanes and the Stratosphere. NASA RP-1010, p. 31, 1977. (Original Reference: Bass, A.M.; Ledford, A.L.; and Laufer, A.H.: *J. Res. NBS*, vol. 80A, 1976, pp. 143-166.)

27. Evans, W.E.: Evaluation of a Near-Infrared Photomultiplier for Airborne Lidar Applications. (Final Report 6919, SRI International, Menlo Park, California. NASA Contract NAS1-14520.) NASA CR-145380, 1978.
28. Fiocco, G.; and Grams, G.W.: Observations of the Upper Atmosphere by Optical Radar in Alaska and Sweden during the Summer 1964. *Tellus*, vol. 18, 1966, pp. 34-38.
29. Fiocco, G.; and Grams, G.W.: Optical Radar Observations of Mesospheric Aerosols in Norway During the Summer 1966. *J. Geophys. Res.*, vol. 74, 1969, pp. 2453-2458.
30. U.S. Standard Atmosphere Supplements, 1966. U.S. Government Printing Office, Washington, D.C. 20402.
31. Wu, M.-F.: Observation and Analysis of Trace Constituents in the Stratosphere. Report DOT-TST-74-7, Environmental Research and Technology, Lexington, Massachusetts (NTIS, Springfield, Virginia), 1973.
32. Fiocco, G.; and Grams, G.W.: On the Origin of Noctilucent Clouds. Extraterrestrial Dust and Trapped Water Molecules. *J. Atmos. Terr. Phys.*, vol. 33, 1971, pp. 815-824.
33. Grams, G.W.; and Fiocco, G.: Equilibrium Temperatures of Spherical Ice Particles in the Upper Atmosphere and Implications for Noctilucent Cloud Formation. *J. Geophys. Res.*, vol. 82, 1977, pp. 961-966.
34. Shettle, E.P.; and Fenn, P.W.: Models of the Atmospheric Aerosols and Their Optical Properties. Paper presented at AGARD Electromagnetic Wave Propagation Panel, 22nd Technical Meeting on Optical Propagation in the Atmosphere, 27-31 Oct. 1975, The Technical University of Denmark, Lyngby, Denmark, 1975. (Available from NTIS, Acc. No. N76-29817.)

35. Ivlev, L.S.; and Popova, S.I.: The Complex Refractive Indices of Substances in the Dispersed Phase. *Izv. Acad. Sci. USSR Atmos. Oc. Phys.*, vol. 9, 1973, pp. 1034-1043.
36. Fiocco, G.; Grams, G.W.; and Visconti, G.: Equilibrium Temperatures of Small Particles in the Earth's Upper Atmosphere (50-110 km). *J. Atmos. Terr. Phys.*, vol. 37, 1975, pp. 1327-1337.
37. Fogel, G.; and Rees, M.H.: Spectral Measurements of Noctilucent Clouds. *J. Geophys. Res.*, vol. 77, 1972, pp. 720-725.
38. Tozer, W.F.; and Beeson, D.E.: Optical Model of Noctilucent Clouds Based on Polarimetric Measurements from Two Sounding Rocket Campaigns. *J. Geophys. Res.*, vol. 79, 1974, pp. 5607-5612.
39. Hummel, J.R.: Contribution to Polar Albedo from a Mesospheric Aerosol Layer. *J. Geophys. Res.*, vol. 81, 1977, pp. 3177-3178.
40. Gadsden, M.: The Sizes of Particles in Noctilucent Clouds-- Implications for Mesospheric Water Vapor. *J. Geophys. Res.*, vol. 83, 1978, pp. 1155-1156.
41. Rosen, J.M.; Hofmann, D.J.; and Laby, J.: Stratospheric Aerosol Measurements. II: The Worldwide Distribution. *J. Atmos. Sci.*, vol. 32, 1975, pp. 1457-1462.
42. Hofmann, D.J.; Rosen, J.M.; Pepin, T.J.; and Pinnick, R.G.: Stratospheric Aerosol Measurements. I: Time Variations at Northern Midlatitudes. *J. Atmos. Sci.*, vol. 32, 1975, pp. 1446-1456.
43. Hofmann, D.J.; and Rosen, J.M.: Balloon Observations of the Time Development of the Stratospheric Aerosol Event of 1974-1975. *J. Geophys. Res.*, vol. 82, 1977, pp. 1435-1440.
44. Russell, P.B.; McCormick, M.P.; Swissler, T.J.; Chu, W.P.; Livingston, J.M.; Fuller, W.H.; Rosen, J.M.; Hofmann, D.J.; McMaster, L.R.; Woods, D.C.; Grams, G.W.; and Pepin, T.J.: Satellite and Correlative Measurements of the Stratospheric Aerosols. -

- II: Comparison of Measurements made by SAM II, Dustsondes, and an Airborne Lidar. J. Atmos. Sci., vol 38, no. 6, June 1981.
45. Bigg, E.K.: Stratospheric Particles. J. Atmos. Sci., vol. 32, 1975, pp. 910-917.
46. Bigg, E.K.: Size Distributions of Stratospheric Aerosols and Their Variations with Altitude and Time. J. Atmos. Sci., vol. 33, 1976, pp. 1080-1086.
47. Gras, J.L.; and Michael, C.G.: Measurement of the Stratospheric Aerosol Particle Size Distribution. J. Appl. Meteor., vol. 18, 1979, pp. 855-860.
48. Toon, O.B.; and Pollack, J.B.: A Global Average Model of Atmospheric Aerosols for Radiative Transfer Calculations. J. Appl. Meteor., vol. 15, 1976, pp. 225-246.
49. Patterson, E.M.; and Gillette, D.A.: Commonalities in Measured Size Distribution for Aerosols Having a Soil-Derived Component. J. Geophys. Res., vol. 82, 1977, pp. 2074-2082.
50. Savoie, D.; and Prospero, J.M.: Saharan Aerosol Transport Across the Atlantic Ocean: Characteristics of the Input and Output. Bul. Am. Meteorol. Soc., vol. 57, 1976, p. 144.
51. Grams, G.W.; Blifford, I.H., Jr.; Gillette, D.A.; Patterson, E.M.; Wartburg, A.F.; and Wyman, C.M.: Measurements of the Light Scattering Properties of the Saharan Dust Layer. Proc. Symposium on Radiation in the Atmosphere (Garmisch-Partenkirchen, FRG, 19-28 Aug. 1976), H. Bolle, Editor, Science Press, Princeton, New Jersey, 1977, pp. 79-81.
52. Patterson, E.M.; Gillette, D.A.; and Stockton, B.H.: Complex Index of Refraction Between 300 and 700 nm for Saharan Aerosols. J. Geophys. Res., vol. 82, 1977, pp. 3153-3161.

53. Patterson, E.M.: Optical Properties of the Crustal Aerosol--Relation to Physical and Chemical Characteristics. *J. Geophys. Res.*, vol. 86, no. C4, April 20, 1981, pp. 3236-3246.
54. Lindberg, J.D.; and Laude, L.S.: Measurement of the Absorption Coefficient of Atmospheric Dust. *Appl. Opt.*, vol. 13, 1974, pp. 1923-1927.
55. Kondratyev, K.Ya.; Barteneva, O.D.; Chapursky, L.I.; Cherenko, A.P.; Grishechkin, V.S.; Ivlev, L.S.; Ivanov, V.A.; Korzov, V.I.; Lipatov, V.B.; Prokofyev, M.A.; Tolkatchev, V.K.; Vasiliev, O.B.; and Zhvaley, V.F.: Aerosol in the GATE Area and Its Radiative Properties. Translated from Russian, *Atmos. Sci. Pap.* 247, Colorado State University, Fort Collins, 1976.
56. Prospero, J.M.; and Carlson, T.N.: Vertical and Areal Distribution of Saharan Dust over the Western Equatorial North Atlantic Ocean. *J. Geophys. Res.*, vol. 77, 1972, pp. 5255-5265.
57. Carlson, T.N.; and Caverly, R.S.: Radiative Characteristics of Saharan Dust at Solar Wavelengths. *J. Geophys. Res.*, vol. 82, 1977, pp. 3141-3152.
58. Grams, G.W.; Blifford, I.H.; Gillette, D.A.; and Russell, P.B.: Complex Index of Refraction of Airborne Soil Particles. *J. Appl. Meteor.*, vol. 13, 1976, pp. 459-471.
59. Pollack, J.B.; Toon, O.B.; and Khare, B.N.: Optical Properties of Some Terrestrial Rocks and Glasses. *Icarus*, vol. 19, 1973, pp. 372-379.
60. Toon, O.B.; Pollack, J.B.; and Khare, B.N.: The Optical Constants of Several Atmospheric Aerosol Species: Ammonium Sulfate, Aluminum Oxide, and Sodium Chloride. *J. Geophys. Res.*, vol. 81, 1976, pp. 5733-5748.

61. Bergstrom, R.W.: Extinction and Absorption Coefficients of the Atmospheric Aerosol as a Function of Particle Size. Contrib. Atmos. Phys., vol. 46, 1973, pp. 223-234.
62. Livingston, J.M.; and Uthe, E.E.: Vertical Aerosol Distributions over the North Atlantic and Mediterranean. (Final Report 6342, SRI International, Menlo Park, California; NRL Contract N00173-77-C-0141.) 1979.
63. Elterman, L.: Vertical-Attenuation Model with Eight Surface Meteorological Ranges, 2 to 13 Kilometers. Environmental Research Papers, no. 318, AFCRL-70-0200, Air Force Cambridge Research Laboratories, Hanscom Field, Bedford, Massachusetts, 1970.
64. Collis, R.T.H.; and Russell, P.B.: Laser Monitoring of the Atmosphere. Lidar Measurement of Particles and Gases by Elastic Back-scattering and Differential Absorption, E.D. Hinkley, Ed. (Springer-Verlag, New York, 1976), 1976, pp. 72-151.
65. Platt, C.M.R.: Lidar and Radiometric Observations of Cirrus Clouds. J. Atmos. Sci., vol. 30, 1973, pp. 1191-1204.
66. Uthe, E.E.; and Russell, P.B.: Lidar Observations of Tropical High-Altitude Cirrus Clouds. Proc. Symp. Rad. in Atmos., Science Press, Princeton, 1972, pp. 242-244.
67. Varley, D.J.; and Brooks, D.M.: Cirrus Particle Distribution Study, Part 2. AFGL-TR-78-0248, Air Force Geophysical Laboratory, Hanscom AFB, Maine 01731, 1978.
68. Reagan, J.A.; Herman, B.M.: Three Optical Methods for Remotely Measuring Aerosol Size Distributions. AIAA Paper no. 71-1057, presented at Joint Conference on Sensing of Environmental Pollutants, Palo Alto, California, 8-10 Nov. 1971.

69. Fernald, F.G.; Herman, B.M.; and Reagan, J.A.: Determination of Aerosol Height Distributions by Lidar. *J. Appl. Meteor.*, vol. 11, no. 3, Apr. 1972, pp. 482-489.
70. Spinhirne, J.D.; Reagan, J.A.; and Herman, B.M.: Vertical Distribution of Aerosol Extinction Cross Section and Inference of Aerosol Imaginary Refractive Index in the Troposphere by Lidar Technique. *J. Appl. Meteor.*, vol. 19, no. 4, Apr. 1980, pp. 426-438.
71. Reagan, J.A.; Bruhns, T.V.; D'Souza, D.D.; and Box, G.P.: Extinction Properties of Tropospheric Aerosols over Tucson, Arizona as Determined by Lidar Measurements. *Amer. Meteor. Soc., Conference Abstracts, Tenth International Laser Radar Conference, Silver Spring, Maryland, 6-9 Oct. 1980, p. 3.*
72. Waggoner, A.P.; Ahlquist, N.C.; and Charlson, R.J.: Measurement of the Aerosol Total Scatter-Backscatter Ratio. *Appl. Opt.*, vol. 11, no. 12, December 1972, pp. 2886-2889.
73. Hamilton, P.M.: Lidar Measurement of Backscatter and Attenuation of Atmospheric Aerosol. *Atmos. Env.*, vol. 3, 1969, pp. 221-223.
74. Derr, V.E.: Estimation of the Extinction Coefficient of Clouds from Multiwavelength Lidar Backscatter Measurements. *Appl. Opt.*, vol. 19, no. 14, 15 July 1980, pp. 2310-2314.
75. Pinnick, R.G.; Jennings, S.G.; Chylek, P.; and Ham, C.: Backscatter and Extinction in Water Clouds. *Conference Abstracts, Tenth International Laser Radar Conference, Am. Meteor. Soc., Silver Spring, Maryland, 6-9 Oct. 1980, pp. 40-41.*

Part 3

ORBITING LIDAR SIMULATIONS:
DENSITY, TEMPERATURE, AEROSOL AND CLOUD MEASUREMENTS
BY A WAVELENGTH-COMBINING TECHNIQUE

I INTRODUCTION

Part Two of this report simulated aerosol and cloud retrievals for a proposed space shuttle lidar using independent-wavelength analysis techniques and conventional density information. It showed that for upper tropospheric and nonvolcanic stratospheric aerosols in areas remote from radiosonde soundings (i.e., over most of the globe), errors in the density profiles inferred from gridded meteorological analysis are usually a leading source of error in retrieved particle backscatter profiles. Moreover, obtaining a density profile from gridded meteorological analysis for each lidar measurement location and time entails considerable expense and delay. The alternative--using model density profiles--reduces expense and delay, but even if the models are carefully selected by location and season, the resulting errors exceed those of gridded analysis. Clearly, the quality, speed, and cost-effectiveness of retrieving cloud and aerosol information from lidar measurements would be enhanced by density information from the lidar itself, provided the lidar density errors were less than those from models or gridded analysis.

Previous experimental studies¹⁻⁴ demonstrated that single-wavelength, low-spectral-resolution lidar measurements can yield very useful relative density profiles and temperature profiles in regions of the atmosphere where particulate backscattering at the lidar wavelength is negligible compared to gas backscattering. However, these single-wavelength techniques clearly fail in obtaining density or temperature profiles in regions where particulate backscattering at the laser wavelength is a nonnegligible fraction of gas backscattering, and they have no means of showing when this particulate contamination occurs. This shortcoming can jeopardize the credibility of any unusual results, which may be of the greatest interest (e.g., unusual density striations or wavelike structures).

DeLuisi et al.⁵ presented a technique for combining lidar signals at three wavelengths and two zenith (or nadir) angles, so as to obtain separate profiles of molecular density and particulate backscatter and extinction. They also showed how the molecular density profile could be combined with the hydrostatic equation and the ideal gas law to obtain a temperature profile (as in Ref. 3). The DeLuisi technique⁵ assumes a specific one-parameter form (linear for the published cases) for the wavelength dependence of particulate backscattering, and uses two of the three lidar wavelengths to solve for the wavelength-dependence parameter. The effect of actual aerosol populations that do not follow the assumed functional form for wavelength dependence was not investigated. Thus, the size of density and temperature errors caused by various aerosol concentrations, wavelength dependences, and lidar parameters could not be evaluated.

This paper presents an alternate, but related, technique for obtaining profiles of gas density and temperature, as well as aerosol and cloud backscattering. A major goal of this technique is to make the minimum possible extension to single-wavelength, single-angle analysis techniques that have been applied for many years, and for which the practical error sources are fairly well understood.⁶ As will be shown, this technique also produces large density and temperature errors when aerosol or cloud concentrations are sufficiently large. However, it minimizes these errors by using a short laser wavelength (to strengthen gas backscatter), and it automatically provides the user with an estimate of these errors at all heights by using cloud and aerosol information determined from a simultaneous longer-wavelength measurement. (It also reduces errors somewhat by using the longer-wavelength measurement to correct for short-wavelength aerosol effects.)

After describing the technique we present an error analysis that includes the effects of errors in lidar signal profiles, transmission profiles, density normalization, and reference pressure or temperature, as well as aerosol or cloud contamination of the lidar density profile.

Finally, we simulate the measurement and retrieval process in order to test the algebraic error expressions and indicate the range of results possible.

For purposes of illustration we assume 1.064 and 0.355 μm as the primary wavelengths for input to the retrieval calculations. These wavelengths are of special interest because:

- They are produced by the Nd:YAG laser (plus frequency-tripling optics), a source that is becoming increasingly popular for current and proposed lidar systems (ground-, air-, and space-based).
- They are sufficiently separated that gas backscattering is much stronger at one than the other.
- The tripled wavelength, 0.355 μm , while short enough to be strongly backscattered by gas molecules, is just long enough to avoid significant absorption by the Hartley-Huggins bands of ozone.

However, the analysis techniques are quite general and could be applied to any other set of wavelengths with some or all of these attributes.

II SOLUTION TECHNIQUE

A. Gas Density and Particle Backscatter Profiles

Figure 1 illustrates the solution technique. The numbers shown indicate the following steps:

Step 1: Use the long-wavelength signal profile $S(\lambda_1, z)$ and a conventional density profile $\rho_c(z)$ (model or interpolated from measurements) to solve for the long-wavelength scattering ratio profile $R(\lambda_1, z)$, and its uncertainty $\delta R(\lambda, z)$, using the conventional single-wavelength technique [Eqs. (4) to (9) and (11) of Part Two of this report].

Step 2: Use the long-wavelength scattering ratio profile and uncertainty with an assumed, typical wavelength dependence (and uncertainty) of particulate backscattering to estimate the short-wavelength scattering ratio profile $R(\lambda_3, z)$ and its uncertainty $\delta R(\lambda_3, z)$. The estimate for $R(\lambda_3, z)$ is given by

$$R(\lambda_3, z) = 1 + [R(\lambda_1, z) - 1] \Psi(\lambda_3, \lambda_1, z) \lambda_1^{-\epsilon(\lambda_1)} \lambda_3^{\epsilon(\lambda_3)}, \quad (1)$$

where Ψ is a best-estimate for the ratio of particulate backscattering at wavelength λ_3 to that at λ_1 , and $\epsilon(\lambda)$ is the wavelength exponent for gaseous elastic backscattering.^{8,9}

[$\delta R(\lambda_3, z)$ is defined in Section III-A.]

Step 3: Use the estimated short-wavelength scattering ratio profile $R(\lambda_3, z)$ and the measured short-wavelength signal profile

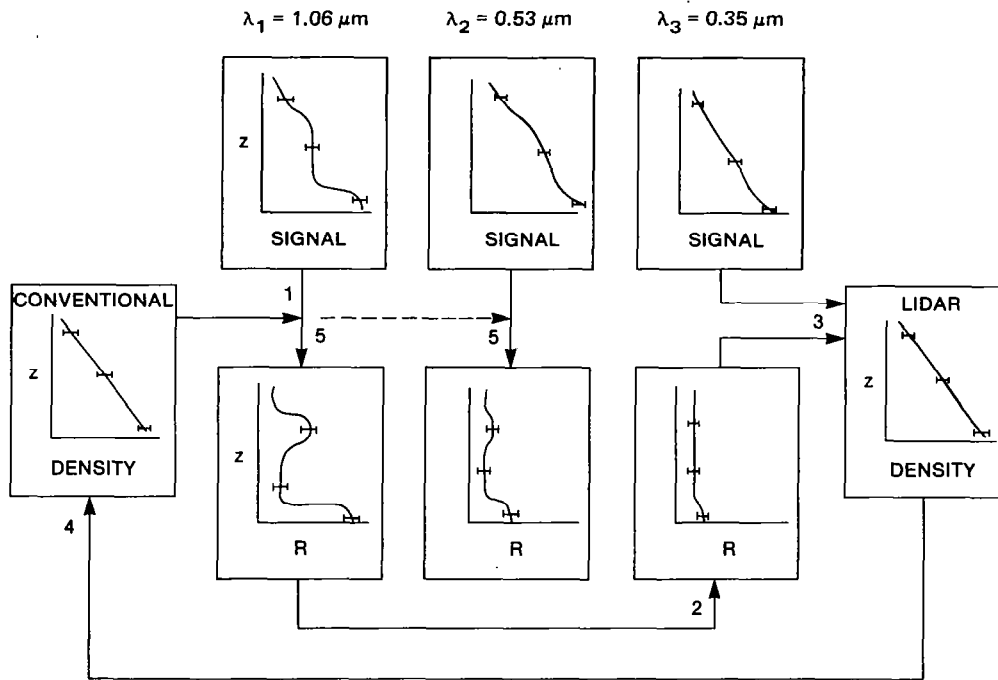


FIGURE 1 MULTIWAVELENGTH ANALYSIS PROCEDURE TO RETRIEVE PROFILES OF SCATTERING RATIO AND MOLECULAR DENSITY

Numbers indicate steps described in the text.

$S(\lambda_3, z)$ to obtain the lidar-derived density profile and its uncertainty. The relative density profile is

$$D(z) \equiv \frac{(z - z_L)^2 S(\lambda_3, z)}{Q^2(\lambda_3, z, z_L) R(\lambda_3, z)}, \quad (2)$$

which follows from Eq. (2) of Part Two of this report, where the symbols are defined. If absolute density ρ is known at any height \hat{z} , the absolute density profile can be obtained as

$$\rho_L(z) = \rho(\hat{z}) \frac{D(z)}{D(\hat{z})}. \quad (3)$$

In this paper we usually choose \hat{z} to be an assumed isopycnic level,¹⁰ where the density can be estimated to high accuracy a priori, because of the very small natural variability there. The uncertainty in Eqs. (2) and (3), including the uncertainty in assuming an isopycnic level, is discussed in Section III-A.

Step 4: Substitute the lidar-derived density $\rho_L(z)$ for the conventional density $\rho_c(z)$ at all heights z where $\delta\rho_L(z) < \delta\rho_c(z)$. Retain the conventional values elsewhere. Call the resulting profile the "composite" density profile.

Step 5: Repeat Step 1 using the composite density profile and its uncertainty in place of the conventional density profile and its uncertainty. Also, if other lidar wavelengths are available (e.g., 0.53 μm in Figure 1), use the composite density profile with the signal profile at each other wavelength to derive the corresponding scattering ratio profiles.

The key to this rather simple procedure is that the ratio of particle to gas backscattering depends very strongly on wavelength. For example, the approximate λ^{-4} wavelength dependence of gas backscattering yields

$$B_g(0.355 \mu\text{m})/B_g(1.064 \mu\text{m}) \approx 81, \quad (4)$$

whereas a typical $\lambda^{-\alpha}$ wavelength dependence of particle backscattering, with typically^{11,12}

$$0 < \alpha < 2 ,$$

yields

$$B_p(0.355 \mu\text{m})/B_p(1.064 \mu\text{m}) \approx 1 \text{ to } 9. \quad (5)$$

This combination yields backscatter mixing ratios B_p/B_g that are much larger at the longest wavelength than at the shortest wavelength. For example, combining Eqs. (4) and (5) yields

$$\frac{B_p(0.355 \text{ } \mu\text{m})}{B_g(0.355 \text{ } \mu\text{m})} \approx (0.012 \text{ to } 0.11) \times \frac{B_p(1.064 \text{ } \mu\text{m})}{B_g(1.064 \text{ } \mu\text{m})} \quad (6)$$

Figures 2 through 4 of Part Two of this report show that, below 40 km, Eq. (6) applies for all aerosol and cloud components of each model atmosphere. This is significant because the aerosol backscatter mixing ratios shown in that figure were derived from Mie-scattering calculations for the size distributions and refractive indices appropriate to each model component (mesospheric, stratospheric, upper tropospheric, Saharan, and marine) rather than for an assumed wavelength dependence, such as the $\lambda^{-\alpha}$ used above for illustration. (Unfortunately, we know of no measurements of natural aerosol and cloud particulate backscatter spanning the wavelength range 0.35 to 1.06 μm .)

This typical wavelength dependence of backscatter mixing ratio means that an aerosol or (subvisible) cloud layer that yields a 0.355- μm scattering ratio of 1.01 (hence perturbing the lidar signal profile by 1 percent) typically yields a 1.064- μm scattering ratio of 1.09 to 1.81; hence, this layer is easily detectable in the 1.064- μm profile, even if errors of 2 to 5 percent are present in the conventional density profile used in Step 1. Detection of such a particulate layer alerts the user to the possible contamination of the lidar-derived density profile and, through Step 2, allows for an approximate, yet useful, correction for these effects. Section III quantifies these arguments and shows how the indication of particulate contamination is automatically included in the error bar $\delta\rho_L$.

Some possible refinements in the multiwavelength solution scheme of Figure 1 are immediately apparent. For example, one could iterate, following Step 5 with several repeats of Steps 2-5, or one could include information on $R(\lambda_2 = 0.53 \text{ } \mu\text{m})$ in Step 2 when estimating $R(\lambda_3)$ from $R(\lambda_1)$. However, the stability of such an iterative scheme is not

guaranteed, and the larger relative errors in $B_p(\lambda_2)/B_g(\lambda_2)$ [see Part Two of this report] may actually degrade the accuracy of estimated $R(\lambda_3)$, unless care is taken to exclude results from λ_2 that do not satisfy some error criterion. For these reasons, and also because our simulations indicate that the basic scheme in Figure 1 can yield very useful results in many situations, we have limited the analyses in this paper to the basic scheme. Refinements of the basic scheme are probably best left until new insights have been developed by applying the basic scheme to actual measurements.

B. Pressure and Temperature Profiles

To derive pressure and temperature profiles from the density profile obtained above, we combine the hydrostatic relation

$$dP(z) = -g(z)\rho(z)dz \quad (7)$$

with the ideal gas law

$$T(z) \approx T'_v(z) = \frac{P(z)}{C_g \rho(z)} \quad (8)$$

In these equations P is pressure, g is the acceleration of gravity, C_g is the gas constant for dry air, T is the absolute air temperature, and T'_v is the adjusted virtual temperature.¹³ Differences between T'_v and the actual temperature T are caused by the presence of water vapor; however, at heights above ~5 km (to which we will find our density measurement technique is limited in practice), typical relative humidities and temperatures yield¹³

$$|T - T'_v| < 1 \text{ K}, \quad (9)$$

and so we henceforth approximate the two as being equal. Since Eq. (7) is in practice applied to the finite interval

$$\Delta z_{i,i\pm 1} \equiv z_i - z_{i\pm 1} \quad , \quad (10)$$

where i identifies a lidar range bin, and since $\rho(z)$ is increasing or decreasing exponentially in this interval, we explicitly integrate Eq. (7) over the finite interval $\Delta z_{i,i\pm 1}$ by assuming a constant scale height in this interval. This yields

$$\Delta P_{i,i\pm 1} = - \int_{z_i}^{z_{i\pm 1}} g(z) \rho(z_i) e^{-(z-z_i)/H_{i,i\pm 1}} dz \quad (11)$$

$$= \bar{g}(z_i, z_{i\pm 1}) H_{i,i\pm 1} [\rho(z_{i\pm 1}) - \rho(z_i)] \quad , \quad (12)$$

where $H_{i,i\pm 1}$ is the scale height, obtained from

$$H_{i,i\pm 1} \equiv (z_{i\pm 1} - z_i) / \ln[\rho(z_i)/\rho(z_{i\pm 1})] \quad . \quad (13)$$

Note that Eq. (11) is equivalent to

$$\Delta P_{i,i\pm 1} = -\bar{g}(z_i, z_{i\pm 1}) \bar{\rho}(z_i, z_{i\pm 1}) \Delta z_{i,i\pm 1} \quad , \quad (14)$$

provided we define

$$\bar{\rho}(z_i, z_{i\pm 1}) \equiv \frac{\rho(z_{i\pm 1}) - \rho(z_i)}{\ln[\rho(z_i)/\rho(z_{i\pm 1})]} \quad . \quad (15)$$

Use of Eq. (15) in place of the linear average

$$\bar{\rho}(z_i, z_{i\pm 1}) = 0.5 [\rho(z_i) + \rho(z_{i\pm 1})] \quad (16)$$

improves accuracy significantly when $\Delta z_{i,i\pm 1}$ is an appreciable fraction of the scale height $H_{i,i\pm 1}$. The choice of a linear or logarithmic definition for the interval-average gravitational acceleration \bar{g} is not critical, because $g(z)$ is a very slowly varying function of z .

If we now define a reference height \bar{z} at which the pressure or temperature can be guessed with an accuracy $\delta\tilde{P}$ or $\delta\tilde{T}$, we have

$$P(z_I) = \tilde{P} + \Delta\tilde{P}_I, \quad (17)$$

where

$$\Delta\tilde{P}_I = -\bar{g}(z_I, \bar{z})\bar{\rho}(z_I, \bar{z})\Delta\bar{z}_I, \quad (18)$$

$$\Delta\bar{z}_I \equiv z_I - \bar{z}, \quad (19)$$

and $I, I+1$ are the indices of the lidar data heights surrounding \bar{z} . The complete pressure profile can then be generated using

$$P(z_i) = P(z_I) + \sum_{j=I+1}^i \Delta P_{j,j-1} \quad (20)$$

for $i > I$ and

$$P(z_i) = P(z_I) + \sum_{j=I-1}^i \Delta P_{j,j+1} \quad (21)$$

for $i < I$. Substituting Eqs. (14), (15), and (17) through (19) into Eq. (20) yields, for the complete pressure profile,

$$P(z_i) = \tilde{P} + K\rho(\bar{z}, z_I) + \sum_{j=I+1}^i k_{j,j-1} \bar{\rho}(z_j, z_{j-1}), \quad (22)$$

with an analogous expression for $i < I$. Here, we have defined

$$\kappa \equiv -\bar{g}(z_I, \bar{z}) \Delta \bar{z}_I, \quad (23)$$

$$k_{j,j\pm 1} \equiv -\bar{g}(z_j, z_{j\pm 1}) \Delta z_{j,j\pm 1}. \quad (24)$$

The temperature profile is obtained by substituting Eq. (22) into Eq. (7) to yield

$$T(z_i) = \frac{\bar{p}}{c_g \rho(z_i)} + \frac{\kappa}{c_g} \frac{\bar{p}(\bar{z}, z_I)}{\rho(z_i)} + \sum_{j=I+1}^i \frac{k_{j,j-1}}{c_g} \frac{\bar{p}(z_j, z_{j-1})}{\rho(z_i)}. \quad (25)$$

If a reference temperature T , rather than a pressure P , is specified, it is convenient to rewrite Eq. (25) as

$$T(z_i) = \bar{T} \frac{\bar{p}}{\rho(z_i)} + \frac{\kappa}{c_g} \frac{\bar{p}(\bar{z}, z_I)}{\rho(z_i)} + \sum_{j=I+1}^i \frac{k_{j,j-1}}{c_g} \frac{\rho(z_j, z_{j-1})}{\rho(z_i)}, \quad (26)$$

where \bar{p} is obtained by exponential interpolation between ρ_I and ρ_{I+1} .

III ERROR ANALYSIS

A. Gas Density and Particle Backscatter Profiles

Applying standard error-propagation techniques¹⁴ to Eq. (1) yields

$$\left(\frac{\delta R_3}{R_3}\right)^2 = \left(\frac{R_3 - 1}{R_3}\right)^2 \left[\left(\frac{\delta R_1}{R_1 - 1}\right)^2 + \left(\frac{\delta \Psi_{3,1}}{\Psi_{3,1}}\right)^2 \right], \quad (27)$$

where we have introduced the shorthand notations

$$R_n \equiv R(\lambda_n, z), \quad (28)$$

$$\Psi_{m,n} \equiv \Psi(\lambda_m, \lambda_n, z). \quad (29)$$

Similarly, one obtains from Eqs. (2) and (3)

$$\left(\frac{\delta \rho_L}{\rho_L}\right)^2 = \left(\frac{\delta \hat{\rho}}{\hat{\rho}}\right)^2 + \left(\frac{\delta(D/\hat{D})}{D/\hat{D}}\right)^2, \quad (30)$$

where

$$\left(\frac{\delta(D/\hat{D})}{D/\hat{D}}\right)^2 = \left(\frac{\delta S_3}{S_3}\right)^2 + \left(\frac{\delta \hat{S}_3}{\hat{S}_3}\right)^2 + \left(\frac{\delta Q^2(\lambda_3, z, \hat{z})}{Q^2(\lambda_3, z, \hat{z})}\right)^2 + \left(\frac{\delta R_3}{R_3}\right)^2 + \left(\frac{\delta \hat{R}_3}{\hat{R}_3}\right)^2, \quad (31)$$

with the shorthand notations

$$\hat{\rho} = \rho(\hat{z}), \quad (32)$$

$$S_m = S(\lambda_m, z), \quad \hat{S}_m = S(\lambda_m, \hat{z}) \quad (33)$$

$$\hat{R}_m = R(\lambda_m, \hat{z}) \quad (34)$$

Also, we have made use of the fact that

$$Q^2(\lambda, \hat{z}, z_L)/Q^2(\lambda, z, z_L) = Q^2(\lambda, \hat{z}, z) = \exp \left[-2 \int_z^{\hat{z}} E(\lambda, z') dz' \right]. \quad (35)$$

[See Eq. (8) of Part Two and discussion.]

Equation (31) neglects a negative term proportional to the covariance of R_3 and \hat{R}_3 . This covariance is nonzero because R_3 and \hat{R}_3 are positively correlated through their dependence on $\Psi_{3,1}$, and also because R_1 and \hat{R}_3 are positively correlated through their dependence on $R_{\min}(\lambda_1)$, $\rho_c(z^*)$, and $S(\lambda, z^*)$ [cf. Eq. (4) of Part Two and Eq. (27) of this part.] However, an algebraic solution for the covariance term is extremely complicated, and its magnitude turns out to be small for the practical cases we will simulate. Because the neglected covariance term in Eq. (31) is negative, Eqs. (30) and (31) give a slight overestimate for $\delta\rho_L/\rho_L$, and are thus conservative. The simulations in Section IV shed light on the magnitude of the neglected covariance for practical cases.

B. Temperature Profiles

In assessing uncertainties in the lidar-derived temperature profile, we make use of the fact that density ρ occurs only as a ratio in Eq. (26) and in all terms but the first in Eq. (25). As a result, lidar-derived T is independent of any constant multiplier in the lidar-derived density profile--particularly of the lidar-derived factor \hat{D} and the assumed isopycnic density $\hat{\rho}$ [see Eqs. (2) and (3)]. [This is true at all heights if the parameter specified at the reference height \tilde{z} is

temperature; if instead the reference parameter is pressure, T depends on \hat{p}/\hat{D} near and above \tilde{z} because of the first term in Eq. (25).]

Substituting Eqs. (3) and (2) into Eq. (26) and approximating density averages by the linear form in Eq. (16) yields

$$T_1 = \tilde{T} \left(\frac{\tilde{D}'}{D_1} \right)^2 + \frac{1}{2 C_g} \left\{ \frac{1}{D_1} \left[K(\tilde{D}' + D_1') + \sum_{j=I+1}^{i-1} k_{j,j-1} (D_{j-1}' + D_j') + k_{i,i-1} D_{i-1}' \right] + k_{i,i-1} \right\}, \quad (36)$$

where

$$D_j' \equiv D(z_j) Q^2(\lambda_3, z_1, z_L) = \frac{(z_j - z_L)^2 S(\lambda_3, z_j)}{Q^2(\lambda_3, z_j, z_1) R(\lambda_3, z_j)}. \quad (37)$$

When pressure P is specified at the reference height, we still can derive Eq. (36) from Eq. (25), except that the first term is replaced by

$$\frac{\tilde{P}}{C_g D_1} \frac{\hat{D}}{\hat{p}}. \quad (38)$$

The primed relative densities D_j' defined by Eq. (37) are identical to the unprimed quantities defined by Eq. (2), except that all two-way transmissions Q^2 are referred to the height z_1 where temperature is being computed. This definition removes the effect of errors in transmission over all heights except those between z_1 and z_j . (Recall that all z_j are between z_1 and \tilde{z} .) This removal occurs because transmission errors at all other heights affect D_1 and D_j equally, and thus cancel in the density ratios of Eqs. (25) and (26). Hence, although D_1 and D_j are correlated in this respect, D_1 and D_j are not. Writing Eq. (36) in terms of primed relative densities therefore

simplifies the error analysis by replacing a correlated set of variables by a set that has this correlation removed.

Applying error propagation analysis¹⁴ to Eqs. (36) and (38) yields

$$(\delta T_I)^2 = \left(\frac{1}{\rho_I} \right)^2 (X + Y + Z) , \quad (39)$$

where

$$Y \equiv \left(\frac{1}{2C_g} \right)^2 \left[\left(\frac{\delta D_I'}{D_I} \right)^2 \rho_I^2 (K + k_{I+1,I})^2 + \sum_{j=I+1}^{i-1} \left(\frac{\delta D_j'}{D_j} \right)^2 \rho_j^2 (k_{j,j-1} + k_{j+1,j})^2 \right] , \quad (40)$$

$$Z = \left(\frac{1}{C_g} \right)^2 \left(\frac{\delta D_i'}{D_i} \right)^2 (P_i - 0.5 \rho_i k_{i,i-1})^2 . \quad (41)$$

If the parameter at the reference height z is temperature, then

$$X \equiv \tilde{\rho}^2 \left[(\delta T)^2 + \left(\frac{\delta \tilde{D}'}{\tilde{D}'} \right)^2 \left(\tilde{T} + \frac{K}{2C_g} \right)^2 \right] ; \quad (42)$$

if instead pressure is specified, then

$$X \equiv \left(\frac{1}{C_g} \right)^2 \left\{ (\delta \tilde{P})^2 + \tilde{P}^2 \left[\left(\frac{\delta Q_1^2}{Q_1} \right)^2 + \left(\frac{\delta \hat{D}}{\hat{D}} \right) + \left(\frac{\delta \hat{\rho}}{\hat{\rho}} \right)^2 \right] + \tilde{\rho}^2 \frac{K}{2} \left(\frac{\delta \tilde{D}'}{\tilde{D}'} \right)^2 \right\} \quad (43)$$

IV SIMULATION PROCEDURE

To test the algebraic error expressions described above, and also to develop insights and data reduction software, we extended the simulation procedure described in Part Two. The extended procedure follows the analysis flow shown in Figure 1. In Steps 1 and 5, which are conventional single-wavelength retrievals, random errors are introduced into the simulated measurements and retrievals as described in Part Two. (See Figure 1 of Part Two.) In Step 2, $R(\lambda_3, z)$ is computed from Eq. (1). Currently we are using

$$\Psi(\lambda_3, \lambda_1, z) \equiv \frac{B_p(\lambda_3, z)}{B_p(\lambda_1, z)} = \left(\frac{\lambda_3}{\lambda_1} \right)^{-1}, \quad (44)$$

independent of height, in this step. The "random errors" in this step are provided by the differences between Eq. (44) and the wavelength dependence of the input aerosol and cloud models at each height. [Recall that multiwavelength backscattering for each aerosol submodel is calculated directly from size distribution and refractive index, rather than from an assumption, such as Eq. (44); the resulting height and latitude dependence of Ψ can be seen in Figures 2 through 4 of Part Two.]

In Step 3 [Eqs. (2) and (3)], random errors in signal and transmission are introduced, just as in the single-wavelength simulations described in Part Two. In addition, a random error is added to the model value for $\rho(\hat{z})$ to simulate an incorrect guess for density at the assumed isopycnic level.

No random errors are added in Step 4.

In Step 5, care is taken to retain the same errors in the conventional density profile as were used in Step 1, as well as the same signal, transmission, and normalization errors for λ_1 .

V SIMULATION INPUTS

The simulations shown in this paper use the same atmospheric models, lidar parameters, background lighting, and error sources for signal, conventional molecular density, transmission, and R_{\min} as used in Part Two. In addition, we have used

$$\frac{\delta \Psi}{\Psi} = 100\% \quad (45)$$

and

$$\left(\frac{\delta \hat{\rho}}{\hat{\rho}} \right) = 2\%, \quad \hat{z} = 8 \text{ km} \quad (46)$$

as measures of the 1 σ uncertainty in the assumption of Eq. (44) and in estimating an "isopycnic" density, respectively. Equation (45) was obtained by inspecting the range of Ψ values, and their rms deviation from Eq. (44), for the aerosol and cloud models described in Appendix A of Part Two. Equation (46) is a very rough estimate obtained by inspecting a collection of model molecular density profiles, plus a small set of balloon-measured temperature, pressure, and density profiles. We recommend that Eq. (46) be reevaluated using a large set of radiosonde data. However, for the present we note that retrieved scattering ratio profiles and temperature profiles are independent of $\hat{\rho}$, so Eq. (46) has no effect on these products or their uncertainties. [Note the discussion just before Eq. (36) for the exception to this case for temperature profiles.] However, retrieved particulate backscattering profiles, density profiles, and pressure profiles do depend on $\hat{\rho}$, and hence their derived uncertainties are sensitive to Eq. (46).

VI SIMULATED PERFORMANCE

A. Tropical, Nonvolcanic, Cloud-Free, Saharan; Nighttime; $\Delta x \approx 200$ km

Figure 5(a) of Part Two¹ has shown the profile of 1.06- μm backscatter mixing ratio ($B_p/B_g = R - 1$) obtained from a simulated nighttime retrieval that combined the 1.06- μm signal profile with a conventional density profile. That retrieval is Step 1 of the multiwavelength analysis procedure (see Figure 1 of this paper). Step 2 uses the 1.06- μm scattering ratio profile (and its uncertainty) with Eqs. (1), (27), (44), and (45) to estimate a 0.355- μm profile of scattering ratio (or backscatter mixing ratio) and its uncertainty. The result is shown in Figure 2(a). The estimated profile (dots) is directly proportional to the 1.06- μm profile in Figure 5(a) of Part Two, because of the assumption of a height-independent Ψ in Eq. (44). Also, the error bar on each dot in Figure 2(a) extends at least from zero to twice the dot, because of the assumed ± 100 percent error in Ψ . [See Eqs. (45) and (27).]

Comparison of the estimate (dots) with the model (solid line) in Figure 2(a) shows that for the aerosol model in this scenario, Eq. (44) leads to a systematic underestimation of $R(0.355 \mu\text{m})$ in the stratosphere and a systematic overestimation in the lower troposphere. This suggests that errors could be reduced by using a height-dependent Ψ that assumes a steeper wavelength dependence for particulate backscattering in the stratosphere, and a less steep one in the troposphere. However, confirming this would require careful inspection of large sets of size distribution and composition data, plus associated Mie-scattering calculations, or, better yet, analysis of a representative set of multiwavelength backscatter measurements. This is beyond the scope of the

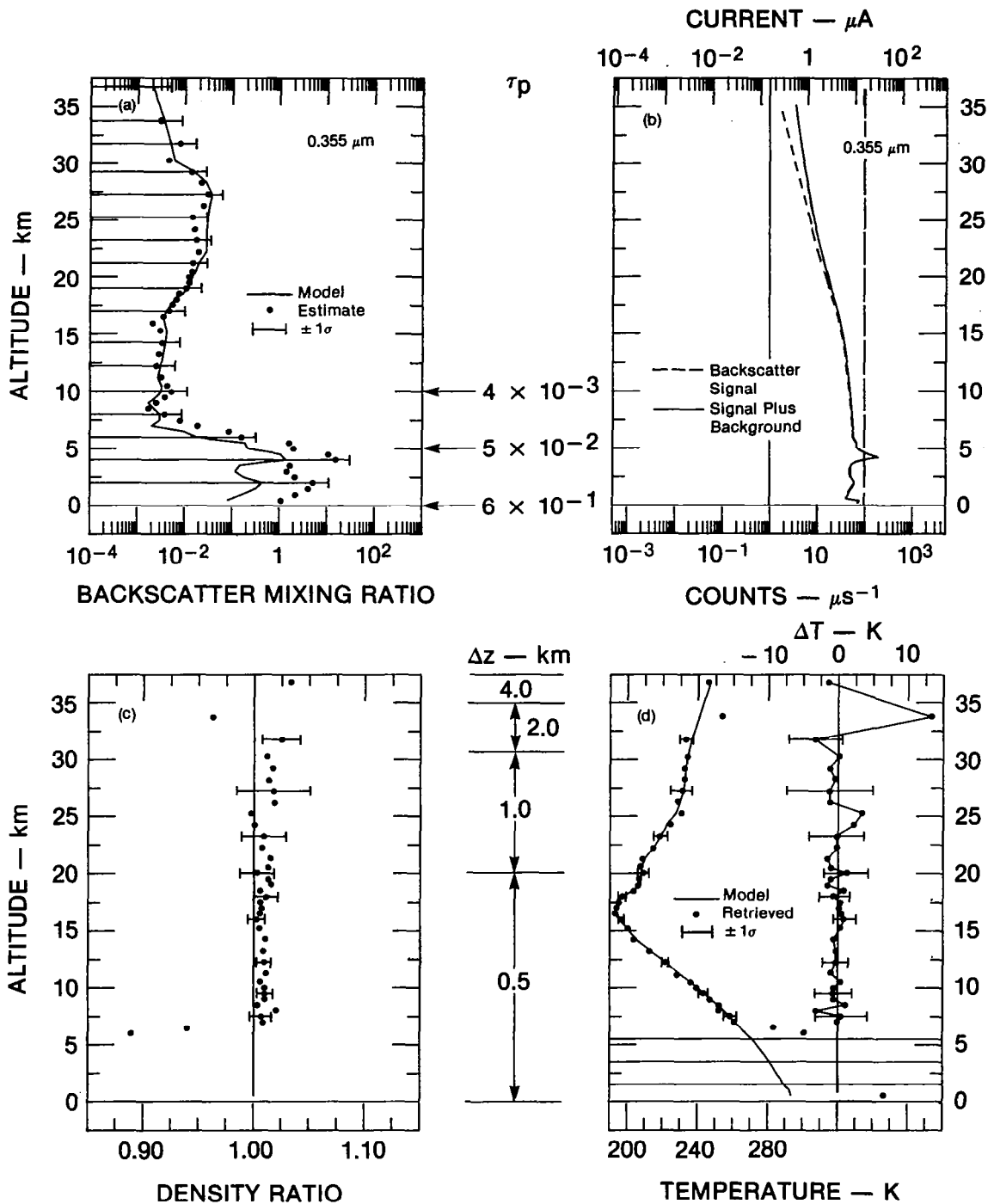


FIGURE 2 LOW-LATITUDE NIGHTTIME SIMULATION RESULTS, $0.355 \mu\text{m}$

(a) Backscatter mixing ratio profile inferred from $1.064\text{-}\mu\text{m}$ profile in Figure 5(a) of Part Two; (b) Signal and background profiles; (c) Density profile retrieved from (a) and (b), expressed as ratio to model; (d) Temperature profile derived from (c), compared to model.

current study; moreover, the simple forms in Eqs. (44) and (45) provide quite useful results and also demonstrate the analysis method.

Step 3 (see Figure 1) combines the estimated backscatter mixing ratio profile in Figure 2(a) with the measured signal profile [shown for a single shot in Figure 2(b)] to obtain the lidar-derived density profile given by Eqs. (2) and (3). The simulated result is shown in Figure 2(c), expressed as a ratio to the exact (model) density profile. Notice that the lidar-derived profile is biased to the right. This results from a 2 percent error in the value guessed for $\hat{\rho}$ at the assumed isopycnic level (8 km), and a partially offsetting error in signal \hat{S} at the same height. [See Eqs. (2), (3), and (30) through (35).] The error bars in Figure 2(c) contain only the uncertainty in the relative profile $D(z)$ as given by Eq. (31). Both the error bars and the scatter among the dots show that the lidar-derived relative density profile for this simulation has a relative ~~10~~ error of ~ 1 percent or less for heights between 8 and 20 km. This is considerably better than the 2 percent assumed for the conventional density profile and, moreover, it comes in a height region where reduction of density errors is most strongly needed to improve particulate retrievals (see below).

Figure 2(d) shows the temperature profile derived from the relative density profile in Figure 2(c) using Eq. (26) and an estimated reference temperature \tilde{T} at 42 km. In the case shown, \tilde{T} was in error by +8 K, and also $D(z)$ was in error by $\sim +2$ percent and ~ -3 percent at 37 and 33 km, respectively (because of lidar signal measurement errors). However, errors in retrieved temperature rapidly become independent of these high-altitude errors, and the errors decrease to between ± 1 and ± 2 K between 20 and 8 km. [This can be most easily seen in the expanded scale on the right of Figure 2(d).] These small errors, combined with lidar's excellent vertical resolution (0.5 km in this height region and scenario), give an excellent retrieval of the tropopause structure. Existing spaceborne nadir-viewing sensors are unable to perform such tropopause retrievals.

Effects of the tropical nonvolcanic stratospheric aerosol layer can barely be seen in Figure 2(c), especially between 22 and 27 km, where the underestimate in $R(0.355 \mu\text{m})$ is greatest [see Figure 2(a)]. However, these effects are comparable in magnitude (~1 percent) to the signal-measurement errors, and so are hard to distinguish from the signal error. Effects of the strong Sahara and marine aerosol layer are very obvious below 7 km, leading to extremely large errors in the lidar-derived density and temperature profiles. However, the error bars, calculated from Eqs. (30) and (39), include the effects of these aerosol layers (detected in the Step 1 analysis at $1.06 \mu\text{m}$) and immediately warn of their presence.

Figure 3 shows results of aerosol retrievals at 1.064 and $0.532 \mu\text{m}$ using the lidar-derived density profile [Figure 2(c)] above 7 km and the conventional density profile below. These results can be compared with Figure 5 of Part Two, which was obtained from the same signal measurements but used the conventional density data at all heights. (Simulated conventional density rms errors were 2 percent below 30 km and 3 percent above.) This comparison shows that the $0.53 \mu\text{m}$ retrieval that uses the lidar density profile [Figure 3(b)] is considerably better in the upper troposphere and lower stratosphere (~8 to 20 km), where density measurement errors have their largest effect (because of the small backscatter mixing ratios). Despite these small backscatter mixing ratios, this is an important region for aerosol measurements, because absolute backscatter and extinction here are comparable to those in the stratospheric peak. Hence, this region contributes significantly to the total stratospheric/upper tropospheric optical depth, and erroneous measurements here can significantly degrade the accuracy of derived optical thickness and column backscatter values. Studies of stratospheric-tropospheric exchange also require accurate measurements in this region.

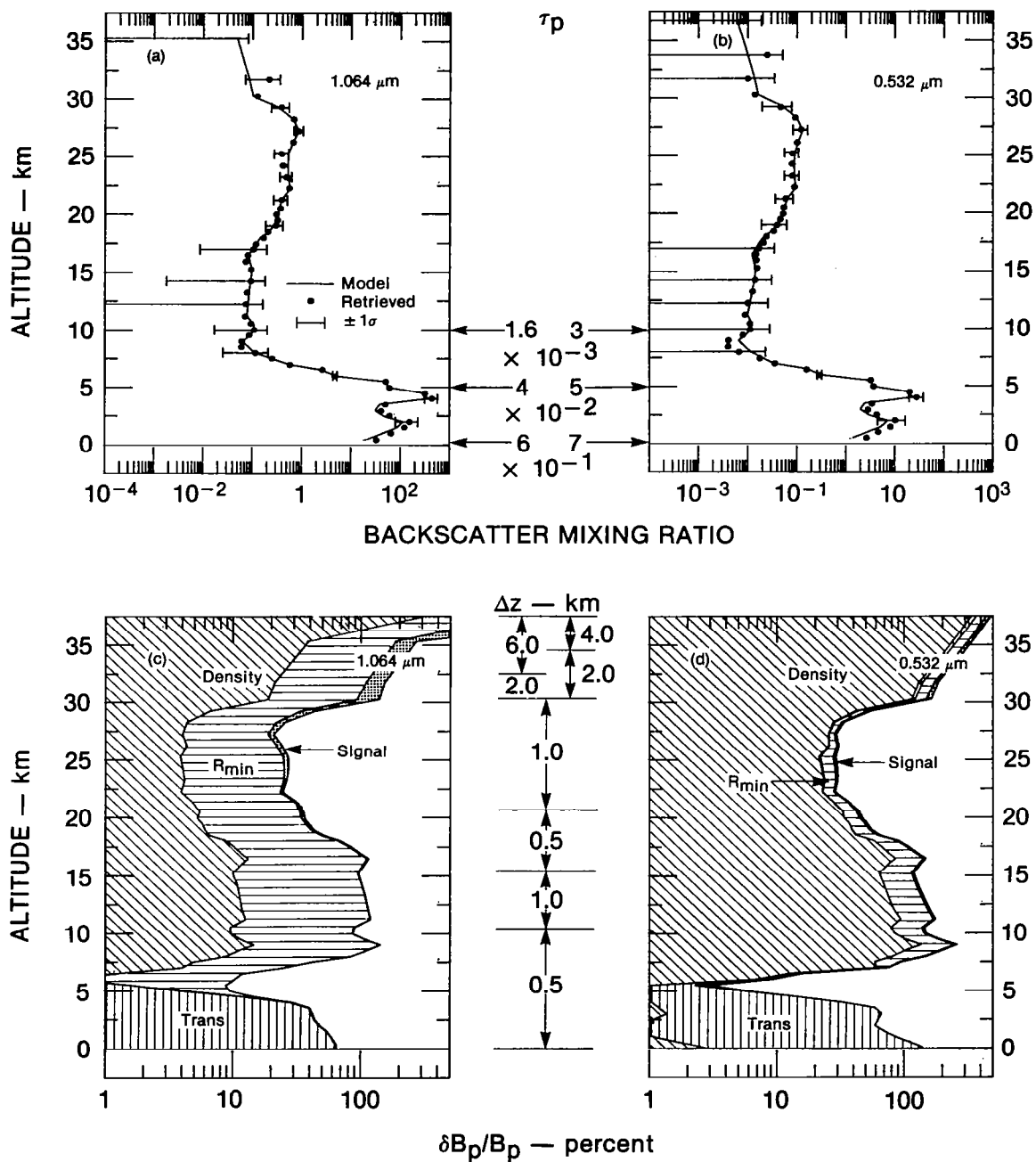


FIGURE 3 LOW-LATITUDE NIGHTTIME SIMULATION RESULTS, 1.064 AND $0.532 \mu\text{m}$, USING LIDAR DENSITY DATA ABOVE 7 km, CONVENTIONAL DENSITY BELOW

(a,b) Backscatter mixing ratio profiles; (c) Relative uncertainty in particulate backscattering broken down by source.

B. Midlatitude, Volcanic, Cloudy, Marine; Nighttime; $\Delta x \approx 200$ km

Figure 4 of this paper shows 0.355- μm results for the same scenario as Figure 7 of Part Two. These results extend only to 44 km because signal-measurement errors exceed 3 percent above that height. In this case the lidar density profile [Figure 4(c)] was again normalized to an assumed isopycnic layer at 8 km, with an offset error of +2 percent. However, in this case the offset increases with increasing height because of transmission errors that accumulate through the considerable optical thickness of the upper two cloud layers and the moderate volcanic stratospheric aerosol layer. This leads to a bias error of about 5 percent above 20 km. Because this error is larger than that expected for the conventional density profile (assumed 3 percent for this case, to simulate use of a local seasonal model density profile), a more accurate absolute lidar density profile could have been obtained by normalizing to the conventional density somewhere between 20 and 30 km (where lidar signal errors are less than 2 percent). However, we have retained the normalization at 8 km to demonstrate that this type of bias or offset error does not significantly affect temperature profile retrievals above the layers in which the transmission errors occur. [Note that the density error bars in Figure 4(c) do not include the density offset error, and thus are not expected to span the difference between the dots and the vertical line. They do describe well the rms difference between each dot and the normalization dot at 8 km, as intended.]

Figure 4(d) shows the temperature profile obtained by integrating the lidar density profile downward from 44 km, where the reference temperature was guessed with an error of +8 K. As in Figure 2(d), after integrating downward by ~ 8 km to become independent of the reference temperature guess and the larger signal-induced density errors, the temperature profile is retrieved to an accuracy of 1 to 3 K (between 32 and 15 km), in spite of the ~ 5 percent density offset error above 20 km. The reason for this was explained between Eqs. (38) and (39). Physically, the reason is that pressures derived from the lidar density

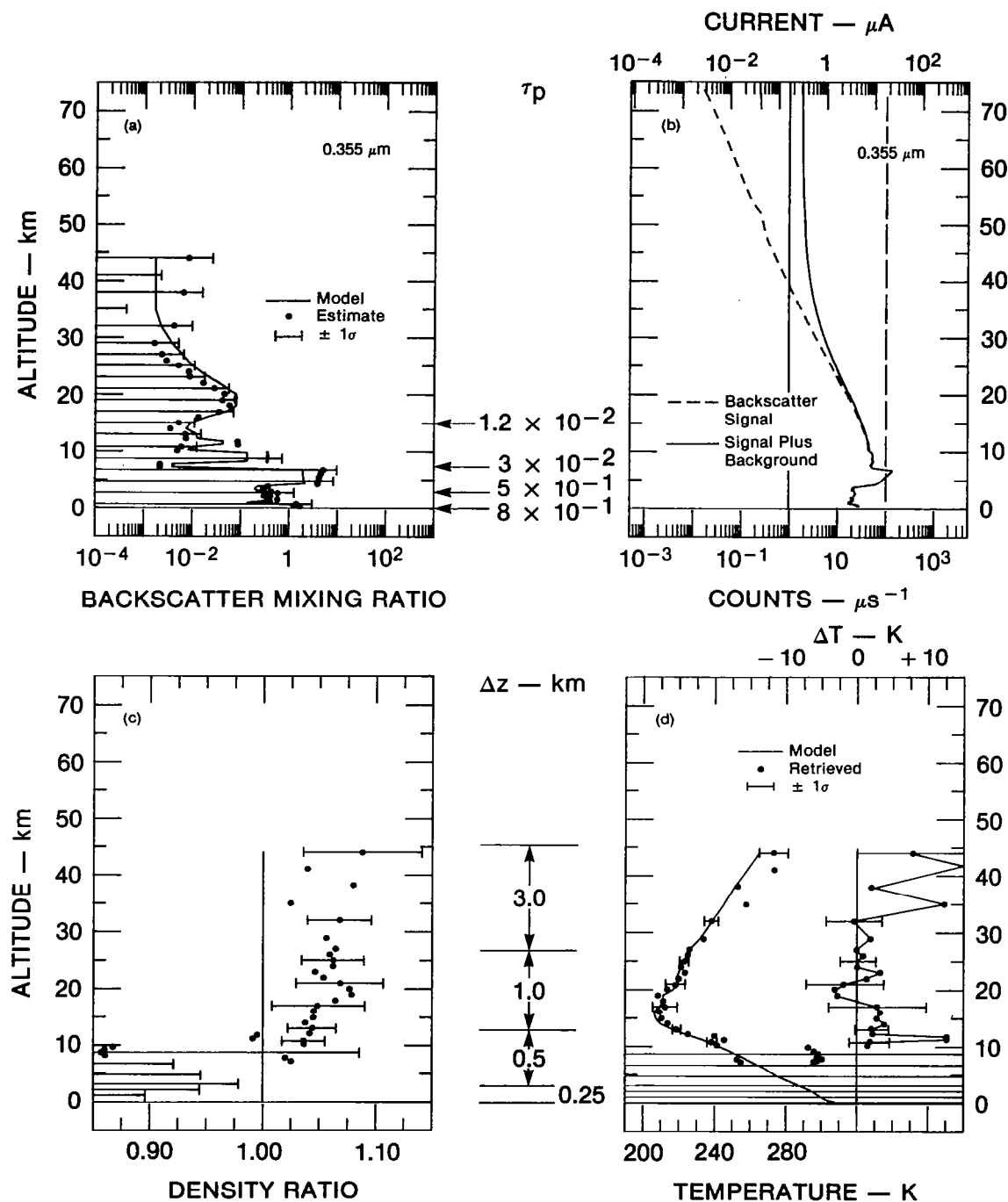


FIGURE 4 MID-LATITUDE NIGHTTIME SIMULATION RESULTS, $0.355 \mu\text{m}$

(a) Backscatter mixing ratio profile inferred from $1.064 \mu\text{m}$ profile in Figure 7(a) of Part Two; (b) Signal and background profiles; (c) Density profile inferred from (a) and (b), expressed as ratio to model; (d) Temperature profile derived from (c), compared to model.

profile are about 5 percent too large between 32 and 20 km; then, in using the gas law [Eq. (8)] to obtain temperature, these pressures are divided by a density that is also too large by about 5 percent.

Between 21 and 18 km, the moderate volcanic stratospheric aerosol introduces a local error of $\sim +3$ percent in density and -3 K in temperature. (The maximum relative temperature error, $-3/215 = -1.5\%$, is less than the maximum relative density error because of a partial compensation in pressure error caused by aerosols just above the peak.) Below the stratospheric aerosol peak, positive temperature errors occur as the transmission-induced density bias errors decrease and there is a mismatch of pressure and density errors. Below 12 km, the subvisible and visible cloud layers cause very large temperature and density errors.

For this scenario, use of the lidar density profile above 12 km produced only minor improvement in backscatter mixing ratio retrievals at 0.53 and $1.06 \mu\text{m}$ (not shown). This is a combined result of the relatively large lidar density errors and the relative insensitivity of the conventional retrievals [Figure 7 of Part Two] to density errors, because of the relatively large moderate volcanic backscatter mixing ratios. This is an example of the general rule that, when particulate layers significantly perturb the lidar density profile, high-accuracy density values are not required to obtain accurate particle retrievals. On the other hand, when backscatter mixing ratios are small (thus requiring highly accurate relative density profiles for particle retrievals) the lidar density profile has very small particle-induced errors.

C. High-Latitude, Nonvolcanic, Cloud-Free, Marine, Nighttime,
 $\Delta x \approx 2000 \text{ km}$

Figure 5 shows $0.355 \mu\text{m}$ results for the same scenario as for Figure 9 of Part Two. In this case, results extend up to 56 km, because the longer integration time (280 s) reduces signal measurement errors to

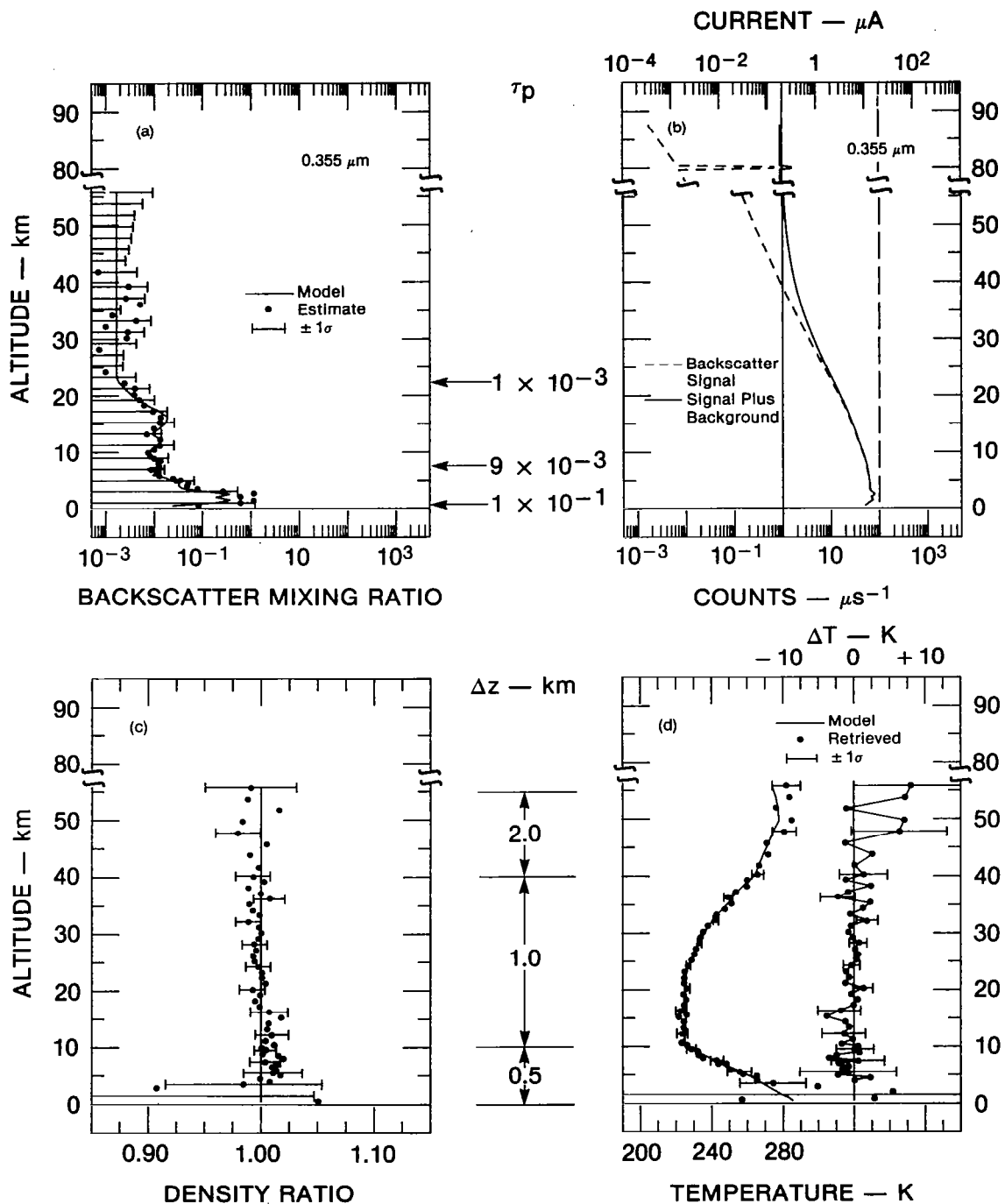


FIGURE 5 HIGH-LATITUDE NIGHTTIME SIMULATION RESULTS, $0.355 \mu\text{m}$

(a) Backscatter mixing ratio profile inferred from $1.064\text{-}\mu\text{m}$ profile in Figure 9(a) of Part Two; (b) Signal and background profiles; (c) Density profile inferred from (a) and (b), expressed as ratio to model; (d) Temperature profile derived from (c), compared to model.

about 3 percent at that level. Again, the lidar density profile was normalized at 8 km with a bias error of +2 percent; however, most of the profile has little offset because of a fortuitously large positive signal error at that height. (As shown above, results for temperature and aerosol retrievals would have been very similar without this fortuitous signal error, because of the insensitivity of these results to bias errors.) The relative density profile has rms errors of 0.5 to 2 percent between 4 and 56 km. These errors are caused primarily by signal errors, although the effect of the nonvolcanic stratospheric aerosol peak can barely be seen at 15 km.

The lidar-derived temperature profile [Figure 5(d)] was obtained by integrating down from 56 km (i.e., near the stratopause), where the reference temperature again had an error of +8 K. As before, temperature errors had decreased to ~3 K at a height (47 km) that was 9 km below the reference height. Between 4 and 45 km, rms temperature errors are 1.2 to 2.5 K, with the exception of a -3.8 K error at 15 km caused by the nonvolcanic stratospheric aerosol layer.

Figure 6 shows 1.06- and 0.53- μm aerosol retrievals using the lidar density profile above 5 km and the conventional profile below. Comparison with Figure 9 of Part Two shows considerable improvement in the ability of the 0.53- μm retrieval to replicate the vertical structure of the stratospheric aerosol. The 1.06- μm retrieval also improves significantly.

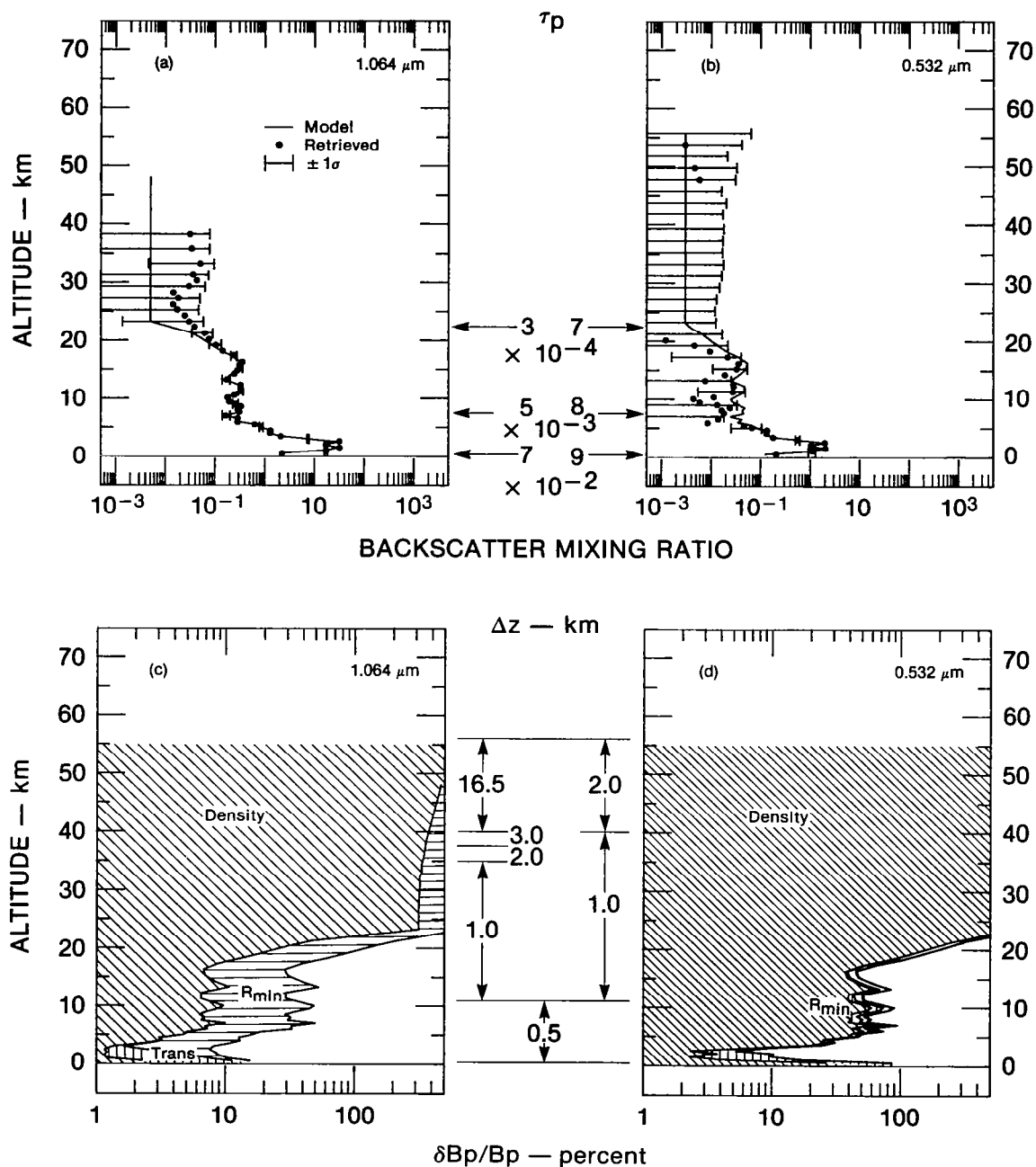


FIGURE 6 HIGH-LATITUDE NIGHTTIME SIMULATION RESULTS, 1.064 AND $0.532 \mu\text{m}$, USING LIDAR DENSITY DATA ABOVE 5 km , CONVENTIONAL DENSITY BELOW

(a,b) Backscatter mixing ratio profiles; (c,d) Relative uncertainty in particulate backscattering broken down by source.

VII SUMMARY AND CONCLUSIONS

We have described an analysis technique that combines lidar signal profiles at long and short wavelengths (in this case, 1.064 and 0.355 μm) to yield profiles of density and temperature, and aerosol and cloud backscatter, each with an associated uncertainty profile. The technique begins with conventional analysis of the long-wavelength profile, which leads to an estimate of particle backscatter at the short wavelength. This estimate is combined with the short-wavelength signal profile to yield a relative density profile and an uncertainty profile that includes effects of aerosol contamination.

This relative density profile is converted to an absolute density profile by normalization at an assumed isopycnic level¹⁰ or a level where conventional density data are available to good accuracy. The lidar-derived density profile is used to improve aerosol and cloud retrievals at 0.53 and 1.06 μm , and is also integrated vertically (from a reference height where temperature or pressure are guessed) to yield pressure and temperature profiles. The two keys to the success of this analysis procedure are:

- Returns at 0.355- μm are much more sensitive to gas backscattering than are those at 1.06 μm . (Hence, on a relative basis, 0.355 μm returns are much less sensitive to aerosol contamination, whereas 1.06 μm returns readily indicate regions where particulate contamination might be significant.)
- Aerosol retrievals and the lidar-inferred temperature profile are relatively insensitive to bias errors in the density profile, so that errors in absolute density normalization have little effect on these data products. Also, this reduces the effect of some transmission errors.

Error analysis equations were developed to quantify the above arguments and to provide error bars on all retrieved quantities. Also, to check the algebraic error expressions, the numerical simulation code was extended to inject appropriate errors into the multiwavelength retrieval

procedure. In addition to the four error sources considered for single-wavelength, conventional retrievals (i.e., errors in signal, transmission, lidar calibration, and conventional density profiles), we also included errors in absolute density normalization, in the reference temperature or pressure, and in estimating short-wavelength particle backscatter from a long-wavelength measurement.

Simulations were run for the low, middle, and high-latitude model atmospheres. In general, cirrus clouds (subvisible as well as visible) and lower tropospheric aerosols introduced larger errors in density and temperature than those in conventional data; daytime signal measurement errors were similarly large in the stratosphere and above. Hence, useful lidar density and temperature measurements were restricted to nighttime conditions in the stratosphere and (cloud-free) upper troposphere. (Signal errors also prevented useful measurements in the mesosphere if horizontal resolution was 2000 km or less.)

Simulations were run with vertical resolutions of 0.5 to 1.0 km in the upper troposphere and lower stratosphere, and 2.0 km in the upper stratosphere. Horizontal resolution of 200 km provided useful signal accuracies (0.5 to 2.0 percent) below 40 km; however, this had to be increased to 2000 km to extend useful signals to 55 km. Retrieved relative density profiles had rms errors of 0.5 to 2 percent in the upper troposphere and stratosphere. The limiting error at most heights was signal measurement error. However, nonvolcanic stratospheric aerosols introduced errors of 1 to 2 percent at the mixing ratio peak (typically ~27 km at low latitudes to ~16 km at high latitudes). For a given amount of nonvolcanic stratospheric particle backscatter, the density error tends to be larger at low latitudes, because the low-latitude peak occurs at greater heights, where the smaller absolute density yields larger relative errors. A midlatitude, moderate volcanic stratospheric aerosol model introduced relative density errors of about 3 percent at the peak (~18 km).

Use of the lidar-derived relative density profiles in place of conventional profiles significantly improved the accuracy of aerosol retrievals in the nonvolcanic stratosphere and upper troposphere--especially at $0.53\text{ }\mu\text{m}$, where conventional density errors gave poor retrievals at these heights. The impact of lidar-derived density errors on volcanic stratospheric aerosol retrievals was minimal, both because of the insensitivity of such retrievals to density errors and because of the poorer accuracy of the volcanic lidar density profile.

For cloud-free, nonvolcanic conditions, lidar-derived temperature profiles had rms errors of 1.2 to 2.5 K in a layer bounded on the bottom by strongly scattering tropospheric aerosol or cloud layers and on the top by a height ~ 8 km below the reference height where temperature or pressure was guessed. For the cloud-free model atmospheres used here, this lower bound was ~ 5 km; the upper bound was ~ 32 km for a horizontal resolution of 200 km and ~ 47 km for a horizontal resolution of 2000 km (i.e., the reference heights were at ~ 40 and ~ 55 km, respectively). The midlatitude, moderate volcanic stratospheric aerosol introduced temperature errors of ~ 3 K between 17 and 20 km. These simulations assumed an 8 K rms error in the temperature guessed at the reference height (40 to 55 km).

The major advantage of these lidar-derived temperature profiles over those obtained by passive nadir-viewing spaceborne sensors is their fine vertical resolution (~ 0.5 km in the upper troposphere and tropopause region, increasing to ~ 2 km in the upper stratosphere). This resolution would permit us to define the tropopause and temperature-wave structures to a degree of detail never before possible from space.

In general, the simulations validated the algebraic expressions used to put error bars on lidar-derived density and temperature profiles. This is important because the errors reported above apply to specific atmospheric situations and will, for example, increase considerably whenever strong particulate (cloud or aerosol) layers are encountered. In this respect the outstanding feature of the multiwavelength analysis technique is that it simultaneously retrieves density and

particle profiles, and includes particle contamination effects in the density and temperature error bars. Thus, when significant cloud or aerosol contamination occurs, the user is immediately aware of it. Overcoming these strong particle contamination effects requires more sophisticated techniques, such as the high spectral resolution method of resolving the narrow particle-backscatter line from the Doppler-broadened Rayleigh line,^{15,16} or differential-absorption measurements of a well-mixed gas, such as molecular oxygen.¹⁷

A previous contract report¹⁸ also describes the two-wavelength elastic backscatter technique for particle/gas separation as a means of measuring gas density profiles. Although that report is based on the same ideas as used here, it differs in the following ways:

- The error-propagation equation (p. 101, Ref. 18) has a fundamentally different form from our equations and does not include any calibration error terms [the δR_{\min} , δS^* , δD^* , $\delta \hat{R}$, $\delta \hat{S}$, $\delta \hat{\rho}$ of our Eqs. (7), (9), (11), (12), Part Two, and (30) and (31), Part Three]. The Ref. 18 equation evidently results from assuming a perfectly calibrated lidar, which does not need to use a "clean" or "isopycnic" atmospheric layer to relate detector output to backscatter coefficient or molecular density. Our experience with actual lidar backscatter measurements has been that some sort of atmospheric calibration is almost always required. This would be especially so for a spaceborne system, where a calibrated target would not be available to measure any system degradation that occurred in orbit. Whereas the error-propagation equation of Ref. 18 shows many of the relevant error processes, we do not feel that it is directly applicable to practical lidar measurements.
- The only signal-measurement error considered is the \sqrt{N} pulse counting error. Other possible signal-measurement errors (e.g., current saturation, nonlinearity, pulse-to-current splicing), which led to the $(\delta S/S)_{\min}$ term in this study, are neglected.
- No simulations with actual lidar data-processing algorithms and random number generators that simulate each error source are run to check the algebraic error-propagation equation.
- The derived expected molecular density error between 5 and 30 km (p. 109 of Ref. 18) varies from 4 to 14 percent, with a peak at ~18 km, provided one assumes an uncertainty in the wavelength-dependence ratio $\psi [\equiv B_p(0.355 \mu\text{m})/B_p(1.064 \mu\text{m})]$ that we consider reasonable [i.e., 50 to 100 percent--see Eq. (45) and Section III-B of Part One]. These expected errors considerably

exceed those (0.5 to 2 percent) obtained in this study for non-volcanic model atmospheres, even though this study assumed $\delta\psi = 100$ percent.

The explanation for the final discrepancy is the different aerosol models used in the two studies. Reference 18 used the LOWTRAN 3B aerosol model.¹⁹ In turn, LOWTRAN 3B uses the Elterman 1968²⁰ vertical profile of midvisible particle extinction in the upper troposphere and stratosphere. As shown by Shettle and Fenn,²¹ the Elterman 1968 extinction profile slightly exceeds the moderate volcanic extinction profiles of Shettle and Fenn. In addition, Ref. 18 assumes a backscatter phase function of 0.04 sr^{-1} for all wavelengths. As shown by Figure B-1 of Part Two, this value may be appropriate for some tropospheric aerosols, but it is a factor of two or more too large for background stratospheric aerosols. The result is that the Ref. 18 stratospheric particle backscatter values significantly exceed our moderate volcanic values, and they exceed our nonvolcanic values by factors between 6 and 9 at wavelength $0.353 \text{ }\mu\text{m}$. The model values of $B_p(\lambda)/B_g(\lambda)$ at the stratospheric peak may be summarized as:

Wavelength (μm)	High- Latitude Nonvolcanic	Low- Latitude Nonvolcanic	Mid- Latitude- Moderate Volcanic	Reference 18
0.355	0.02	0.03	0.09	0.17
0.532	0.05	0.1	0.25	0.45
0.694	0.1	0.25	0.7	0.85
1.064	0.3	1.0	2.0	2.4

The middle three columns are taken from Figures 2 through 4 of Part Two. The final column is from pp. 97 and 99 of Ref. 18, with the 0.532 and 0.694 μm wavelength values logarithmically interpolated between the 0.355 and 1.064 μm values.

This comparison raises the questions of

- (1) How well are the various models supported by measurements?
- (2) How often do "nonvolcanic" and "moderate volcanic" conditions occur?

Our models are based on dustsonde measurements of particle number, coupled with model size distribution and refractive index ranges that are also based on measurements. Our models have been validated by comparisons to ruby lidar backscatter measurements ($\lambda = 0.694 \mu\text{m}$), but when the models were developed no 1.064- or 0.353- μm backscatter measurements were available for validation. Since then, Shibata et al.²² have published nonvolcanic profiles of B_p/B_g at 1.06 μm . Although 0.353- μm measurements were not made, 0.532- μm measurements were made, and these are useful in estimating upper bounds. Ruby²³⁻²⁵ and Nd-YAG²² measurements of peak stratospheric $B_p(\lambda)/B_g(\lambda)$ may be summarized as:

Wavelength (μm)	High- Latitude Nonvolcanic	Low- Latitude Nonvolcanic	Mid- Latitude- Moderate Volcanic
0.532		0.08-0.1 ²²	
0.694	0.1 ²³	0.2 ²⁴	0.7 ^{25,26}
1.064		0.25-0.4 ²²	

These measured values agree quite well with the corresponding model values summarized above, but they are markedly less than the Ref. 18 model values.

Regarding the question of frequency of occurrence of "nonvolcanic" and "moderate volcanic" conditions, the time series of ruby lidar backscatter compiled by Russell and Hake²⁶ and Swissler et al.²⁵ are of interest. From them one can derive the following percentages of time that measured peak stratospheric backscatter mixing ratio ($\lambda = 0.69 \mu\text{m}$) occurred in various categories.

Percent of Time Measured Values Were:				
<u>Time Span</u>	<u>Less Than NV</u>	<u>NV to MV</u>	<u>MV to R18</u>	<u>Greater Than R18</u>
1964-73 ²⁶	5	70	13	13
1974-80 ²⁵	50	39	2	8
1964-80 ^{25,26}	23	57	8	11

NV = nominal midlatitude nonvolcanic model (average of high- and low-latitude).

MV = midlatitude moderate volcanic model.

R18 = Reference 18 model.

Note that measured values equaled or exceeded the Ref. 18 model value only 11 percent of the time in the 17-year period from 1964 through 1980. For this same period, measured values occurred most frequently (57 percent of the time) between our nominal nonvolcanic and moderate volcanic values. However, measured values were actually less than our nominal nonvolcanic value 23 percent of the time in 1964-80 and 50 percent of the time in 1974-80.

When one considers that the above model values are peak values, and that the peak is usually confined to a layer several km thick or less, it is evident that aerosol particle backscatter contamination in all but a few km of the upper troposphere and stratosphere, at wavelength 0.35 μm , should most of the time be several percent or less, and should very rarely attain the values of Ref. 18. In addition, the simultaneous availability of the 1.06- μm particle measurements immediately highlights the heights and times when particle contamination occurs, and it also permits an approximate correction for those effects.

REFERENCES

1. Kent, G.S.; Keenlside, W.; Sandford, M.C.W.; and Wright, R.W.H.: Laser Radar Observations of Atmospheric Tides in the 70-100 km Height Region. J. Atmos. Terr. Phys., vol. 34, 1972, pp. 373-386.
2. Kent, G.S.; and Keenlside, W.: Laser Radar Observations of Seasonal Changes in Atmospheric Density in the Mesosphere and Lower Thermosphere. J. Atmos. Sci., vol. 31, no. 5, July 1974, pp. 1409-1412.
3. Hauchecorne, A.; and Chanin, M.-L.: Density and Temperature Profiles Obtained by Lidar Between 35 and 75 km. Geophys. Res. Lett., vol. 7, no. 8, August 1980, pp. 565-568.
4. Fuller, W.H. Jr.; Swissler, T.J.; and McCormick, M.P.: Comparative Analysis of Red-Blue Lidar and Rawinsonde Data, in Atmospheric Aerosols: Their Optical Properties and Effects. NASA CP-2004, 1976, pp. TuC2-1 to 4.
5. DeLuise, J.J.; Schuster, B.G.; and Sato, R.K.: Separation of Dust and Molecular Scattering Contributions to the Lidar Observation: a Method. Appl. Opt., vol. 14, no. 8, Aug. 1975, pp. 1917-1923.
6. Russell, P.B.; Swissler, T.J.; and McCormick, M.P.: Methodology for Error Analysis and Simulation of Lidar Aerosol Measurements, Appl. Opt., Vol. 18, No. 22, Nov. 15, 1979, pp. 3783-3797.
7. Greco, R.V.: Atmospheric Lidar Multi-User Instrument System Definition Study. NASA CR-3303, 1980.
8. Frolich, C.; and Shaw, G.E.: New Determination of Rayleigh Scattering in the Terrestrial Atmosphere. Appl. Opt., vol. 19, no. 11, 1 June 1980, pp. 1773-1775.

9. Young, A.T.: Revised Depolarization Corrections for Atmospheric Extinction. Appl. Opt. vol. 19, no. 20, 15 Oct. 1980, pp. 3427-3428.
10. U.S. Standard Atmosphere Supplements, 1966. U.S. Government Printing Office, Washington, D.C. 20402.
11. Collis, R.T.H.; and Russell, P.B.: Lidar Measurement of Particles and Gases by Elastic Backscattering and Differential Absorption. Chapter 4 of Laser Monitoring of the Atmosphere, E.D. Hinkley, editor, Springer-Verlag, 1976, pp. 71-151.
12. Pinnick, R.G.; Rosen, J.M.; and Hofmann, D.J.: Stratospheric Aerosol Measurements III: Optical Model Calculations. J. Atmos. Sci., vol. 33, no. 2, Feb. 1976, pp. 304-314.
13. List, R.J.: Smithsonian Meteorological Tables. Smithsonian Institution Press, Sixth Edition, 1949, p. 295.
14. Bevington, P.R.: Data Reduction and Error Analysis for the Physical Sciences. McGraw-Hill, 1969, p. 336.
15. Fiocco, G.; Benedetti-Michelangeli, G.; Maichsberger, K.; and Madonna, E.: Measurement of Temperature and Aerosol to Molecule Ratio in the Troposphere by Optical Radar. Nature Physical Sci., vol. 229, 18 January 1971, pp. 78-79.
16. Shipley, S.T.; Joseph, J.H.; Trauger, J.T.; Guetter, P.J.; Eloranta, E.W.; Lawler, J.E.; Wiscombe, W.J.; Odell, A.P.; Roesler, F.L.; and Weinman, J.A.: The Evaluation of a Shuttle-Borne Lidar Experiment to Measure the Global Distribution of Aerosols and Their Effect on the Atmospheric Heat Budget. (Department of Meteorology, University of Wisconsin, Madison, Wisconsin 53706; NASA Grant NSG-1057.) April 1975. (NASA CR-146134, 1975.)

17. Korb, C.L.; Kalshoven, J.E.; and Weng, C.Y.: A Lidar Technique for the Measurement of Atmospheric Pressure Profiles. Trans. Amer. Geophys. Union, vol. 60, no. 18, 1 May 1979, p. 333 (abstract only).
18. Brehm, W.F.; and Buckley, J.L.: Design Study of a Laser Radar System for Spaceflight Application. Final Report, General Electric Space Division, to Air Force Geophysics Laboratory, Hanscom AFB, Massachusetts. (AFGL-TR-79-0624, 1979.)
19. Selby, J.E.A.; Shettle, E.P.; and McClatchey, R.A.: Atmospheric Transmittance from 0.25 to 28.5 μm ; Supplement LOWTRAN 3B. Air Force Geophysics Laboratory, Hanscom AFB, Massachusetts. (AFGL-TR-76-0258, 1977.)
20. Elterman, L.: UV, Visible, and IR Attenuation for Altitudes to 50 km, 1968. Air Force Geophysics Laboratory, Hanscom AFB, Massachusetts. (AFCRL-68-0153, AD 671933, 1968.)
21. Shettle, E.P.; and Fenn, R.W.: Models of the Atmospheric Aerosols and their Optical Properties. AGARD Conference Proceedings No. 183, Optical Propagation in the Atmosphere. Electromagnetic Wave Propagation Panel Symposium, Lyngby, Denmark, 27-31 October 1975, AGARD-CP-183, NTIS, AD A028-615. [Reproduced by B.M. Herman, A.J. LaRocca and R.E. Turner, Chapter 4 The Infrared Handbook, Atmospheric Scattering, W.L. Wolfe and G.J. Zissis, eds., Office of Naval Research, Department of the Navy, Government Printing Office SN008-051-00068-2.]
22. Shibata, T.; Fujiwara, M.; and Hirono, M.: Observation of Stratospheric Aerosols by Nd:YAG Lidar with a New Type of Near-Infrared-Sensitive Photomultiplier Tube. Japan J. Appl. Phys., vol. 19, no. 11, November, 1980, pp. 2205-2209.
23. Russell, P.B.; McCormick, M.P.; Swissler, T.J.; Chu, W.P.; Livingston, J.M.; Fuller, W.H.; Rosen, J.M.; Hofmann, D.J.; McMaster, L.R.; Woods, D.C.; Grams, G.W.; and Pepin, T.J.: Satellite and

Correlative Measurements of the Stratospheric Aerosol. II: Comparison of Measurements Made by SAM II; Dustsondes, and an Airborne Lidar. J. Atmos. Sci., vol. 38, no. 6, June 1981.

24. Philip, M.T.; and Kent, G.S.: Lidar Measurements of the Stratospheric Aerosol Layer over Kingston, Jamaica. Conf. Abstr. Vol., Tenth Int. Laser Radar Conf., Amer. Meteor. Soc., Boston, Massachusetts, pp. 134-135.
25. Swissler, T.J.; Hamill, P.; Osborn, M.; Russell, P.B.; and McCormick, M.P.; 1981: A Comparison of Lidar and Balloonborne Particle Counter Measurements of the Stratospheric Aerosol 1974-1980. Submitted to J. Atmos. Sci.
26. Russell, P.B.; and Hake, R.D.: The Post-Fuego Stratospheric Aerosol: Lidar Measurements, with Radiative and Thermal Implications. J. Atmos. Sci., vol. 34, no. 1, January 1977, pp. 163-177.

1. Report No. NASA CR-3473		2. Government Accession No.		3. Recipient's Catalog No.	
4. Title and Subtitle IMPROVED SIMULATION OF AEROSOL, CLOUD, AND DENSITY MEASUREMENTS BY SHUTTLE LIDAR				5. Report Date November 1981	
				6. Performing Organization Code	
7. Author(s) *Philip B. Russell, Bruce M. Morley, John M. Livingston, **Gerald W. Grams, and Edward M. Patterson				8. Performing Organization Report No. 1215	
9. Performing Organization Name and Address *SRI International **School of Geophysical Sciences 333 Ravenswood Avenue Georgia Institute of Technology Menlo Park, California 94025 Atlanta, Georgia				10. Work Unit No.	
				11. Contract or Grant No. NAS1-16052	
12. Sponsoring Agency Name and Address National Aeronautics and Space Administration Washington, D.C. 20546				13. Type of Report and Period Covered Contractor Report	
				14. Sponsoring Agency Code	
15. Supplementary Notes Langley Technical Monitor: Edward V. Browell Final Report					
16. Abstract Data retrievals are simulated for a Nd:YAG lidar suitable for early flight on the space shuttle. Maximum assumed vertical and horizontal resolutions are 0.1 and 100 km, respectively, in the boundary layer, increasing to 2 and 2000 km in the mesosphere. Aerosol and cloud retrievals are simulated using 1.06 and 0.53 μm wavelengths independently. Error sources include signal measurement, conventional density information, atmospheric transmission, and lidar calibration. By day, tenuous clouds and Saharan and boundary-layer aerosols are retrieved at both wavelengths. By night, these constituents are retrieved, plus upper tropospheric, stratospheric, and mesospheric aerosols and noctilucent clouds. Density, temperature, and improved aerosol and cloud retrievals are simulated by combining signals at 0.35, 1.06, and 0.53 μm . Particulate contamination limits the technique to the cloud-free upper troposphere and above. Error bars automatically show effects of this contamination, as well as errors in absolute density normalization, reference temperature or pressure, and the sources listed above. For nonvolcanic conditions, relative density profiles have rms errors of 0.5 to 2% in the upper troposphere and stratosphere. Temperature profiles have rms errors of 1.2 to 2.5 K and can define the tropopause to 0.5 km and higher wave structures to 1 or 2 km.					
17. Key Words (Suggested by Author(s)) Lidar, space shuttle, aerosol, cloud, density, temperature, data retrieval, simulation, error analysis, Nd:YAG, laser			18. Distribution Statement Unclassified — Unlimited Subject Category 46		
19. Security Classif. (of this report) Unclassified		20. Security Classif. (of this page) Unclassified		21. No. of Pages 167	
				22. Price A08	